Master Thesis

Tip enhanced Raman spectroscopy of carbon nanotubes

(カーボンナノチューブのチップ増強ラマン分光)

Graduate School of Science, Tohoku University
Department of Theoretical Condensed Matter Physics

Thomas Rafael Czank

September 2015

Acknowledgements

My amazing experiences in Japan would not have been possible without the MEXT research scholarship, granted to me in April of 2013 and that would not have been possible without Professor Saito invitation letter, since the first contact he tried to make me feel very comfortable using some of the Brazilian Portuguese vocabulary he had acquired. Since my arrival to Japan he allowed me to spend some of my time to study Japanese and to engage in traveling around Japan and joining cultural events. But eventually the cultural differences that confronted me since coming from Brazil also took their toll on me, however, so lucky I ever was of having the continuous support and attention from my family and friends even while being 12h behind the Japanese time zone, that means sometimes they would be at work or about to sleep, and would still struggle to message with me.

During the beginning I had great tutoring from Hesky on learning the very basics from carbon nanotubes theory and reviewing other elementary concepts from solid state physics, while teaching me all that he was always very patient, in order to get my foreigner ID in Japan, open a bank account among other things I had the untiring aid of Tatsumi, he was so kind to drive me to each of these places. To get used to the computer settings in the lab I could repetitively count on Nugraha, that always gives very direct instructions so everyone can understand how to enjoy the facilities needed for running simulations and other purposes.

Finally after one introductory semester of adaptation and preparing, I took the Master's course entrance examination, and got accepted in Tohoku University Physics Graduate School, to accomplish this I needed so much help from Wakou-san on filling in the official forms requested. She was always very kind and patient on being asked the same questions several times. During this time a brazilian undergraduate physics student came to the lab, Pedro stayed for a whole year, and it was almost as if I was back home again, but not only because of that I am also thankful to him because of the opportunity given to me, I became his tutor, and it was a very exciting and interesting experience, regarding not only teaching but also being questioned.

When completing 1 year in master's course I discovered a new friendship and deeply enriching source of culture and high level physics. Pourya from Iran, completely changed my mind views about his home country and basically lectured me on physics, programming and flirting on a daily basis.

To finish with I am completely and forever thankful to all people mentioned here and also many others, like Ciro and Gabriel, who live with me sharing an apartment and an ever stronger friendship, Marina who even in Brazil and many times busy would be available to listen to my complaints about everything, my oldest brother Ginio that always wanna play games with me, Larissa who rekindled my former excitement for living in Japan, Maisa for being the friend for a friend in need, Yuka for setting my heart on fire once more, for my brother Luizinho that came to visit me and remind me that I will always have a life and family at home and for my father who always made clear I could give up on everything and just go back home if I wanted.

The only wish I had besides finishing this thesis in a closed and complete way would be for my mother who sadly passed away in 2010 to be here so I could thank her again for everything.

Contents

1 Introduction **1**

1.1 Purpose of the study 1

1.2 Organization 2

1.3 Preface 3

2 Background **7**

2.1 Carbon Nanotubes Fundamentals 7

2.1.1 Excitons in SWNTs 12

2.1.2 Tip enhanced Raman spectroscopy (TERS) 16

2.1.3 Scattering of light by a metallic sphere 20

2.1.4 Au and Ag Dielectric Functions 21

2.1.5 Raman spectroscopy quantum phenomena 33

3 Theoretical methods **39**

3.1 Quasi-static approximation 39

3.2 Dipole radiation 47

3.2.1 Dipole radiation 48

3.3 Mie's Spherical Light Scattering Theory 52

3.3.1 Solution of the scattered wave 52

3.3.2 Solution of the internal field 59

3.3.3 Coefficients of the scattered and internal field's components . 63

3.4 Exciton Theory in carbon nanotubes 71

3.4.1 Exciton Symmetries and the Dipole selection rules for carbon nanotubes . . . 73
3.4.2 Carbon nanotubes Exciton's Wavefunctions . . . 75
3.4.3 Exciton-photon matrix element . . . 79
3.4.4 Dipole vector for Graphene and for SWNT . . . 81
3.5 Exciton photon near field matrix element . . . 85
3.6 Near field factors . . . 86
3.7 The exciton photon near-field matrix element . . . 90
3.8 Exciton-photon near field element for achiral SWNT . . . 97
3.8.1 Armchair SWNT near field exciton-photon matrix element . . . 97
3.8.2 Zigzag SWNT near field exciton-photon matrix element . . . 101

4 Results and Discussions **103**
4.1 Tip enhanced Raman intensity formulation . . . 103
4.2 Chirality dependence of $Z_k D_k$ summation . . . 107

5 Conclusion **109**

A **111**
A.1 Vector calculus in spherical coordinates . . . 111
A.1.1 Differential identities in spherical coordinates . . . 111
A.1.2 Vector Laplacian . . . 112
A.2 Differential equations for the Transverse Magnetic mode . . . 113
A.2.1 Faraday's law . . . 113
A.2.2 Ampere and Maxwell law . . . 114
A.2.3 Differential equation of E_θ in TM mode . . . 114
A.2.4 Differential equation of E_ϕ in TM mode . . . 115
A.2.5 Differential equation of B_θ in TM mode . . . 115
A.2.6 Differential equation of B_ϕ in TM mode . . . 115
A.3 The associated Legendre polynomials . . . 115

A.4 The spherical Bessel and the spherical Hankel functions 117

B **119**

B.1 Exciton near field matrix element calculation program 119

Chapter 1

Introduction

1.1 Purpose of the study

The main objective of this study is to predict tip enhanced Raman spectra by calculating each factor that contributes to the increment in the scattered light intensity, those are: the generation of a near field around the tip apex, which was approximated as a sphere, to find out the behavior of the scattered radiation by this sphere, the Helmholtz Vector equation with Mie's scattering solution was sought [1]. Inside the aforementioned equation as the tip is made of metal its dielectric function had to be considered as dependent on the wavelength λ.

Apart from the previous electromagnetic part, the physical properties of the sample, in the current study, single wall carbon nanotubes (SWNT), had to be considered, the effects of the radiation in the sample, among which is the generation of the excitons that change completely the Raman intensity usual formulation, in order to understand the generation of excitons and how the radiation influences the carriers states inside SWNTs, an optical perturbed Hamiltonian had to be solved, and after that how would the dipole vector be changed by the near field factor from the optical perturbation in the Hamiltonian.

Regarding the exciton, in order to consider the change in its transitions with the

dipole vector, its wave-function amplitude was needed and to obtain it the Bethe-Salpeter equation was solved, from quantum electrodynamics this equation considers all of the possible interactions that might occur between the electron and the hole.

Even tough the solution for Helmholtz Vector equation and the Mie's scattering were done analytically, physical properties from SWNT, the radiation interaction with the sample, namely the dipole vector, the near field factor influence, Bethe-Salpeter equation and others were done numerically, and the Fortran codes are included in the appendices with some explanation on their use, or their original thesis will be cited.

Not only predicting the new Raman intensity but also investigating the relationship between the theory and the experimental data, the tip apex spherical approximation radius, the dielectric function from its material, the distance to the sample, SWNT chirality dependence, and others that have not been so well discussed like the Exciton transition dependence [2], those are the purpose of this thesis.

1.2 Organization

This study is going to be expanded following in the next chapter, (i) the very well based concepts of SWNTs physical properties, (ii) the excitons generated inside them, (iii) a more detailed description of usual and tip equipped Raman experimental arrangements and results, (iv) about the spherical dispersion of the incident electromagnetic radiation, (v) the dielectric function behavior from the metals used in some tip equipped Raman experiments and finally a (vi) Raman intensity brief introduction.

In chapter 3, a quasi-static approximation is explained as a preview of the near field behavior present near the tip, followed by a thorough and realistic analytical solution of the Helmholtz equation, in which every coefficient from the far field and near field factors are obtained. Also in this chapter the exciton wave functions are discussed, and the excitons types are discussed and classified. Also contains the step by step discussion and formulation of the exciton-near field interaction near field

element, the near field and far field factors are clearly separated and compared, then the near field dipole vector is calculated and formulated for armchair SWNT and for zig-zag, unfortunately there is no general chirality formulation yet.

Chapter 4 shows some predictions for armchair chiralities of the near field enhanced Raman intensities, the chirality dependence is shown and an enhancement coefficient is studied compared the usual and near field Raman spectras.

And finally the conclusion on chapter 5, that summarizes the developments and the weak and incomplete points yet to be elaborated.

1.3 Preface

Raman spectroscopy is the material analysis technique in which radiation is shone over a desired sample. This material has some modes of vibration of specific frequencies, namely, energies, if the incident light has a close frequency to the aforementioned ones, there is a resonance effect and the intensity of the scattered radiation peaks. Using this effects it is possible to use it as an imaging technique.

Recently nanosciences have kept decreasing the dimensions of the developed devices, as a result, in order to be able to perform a physical property analysis it is necessary to use smaller wavelength than these devices dimensions, but there is a limit, the diffraction limit, [3] the spatial resolution Δx can not be smaller than $\lambda/2$. Given this limit, in order to improve the resolution of Raman imagining, non decreasing wavelength of the incident radiation techniques were the solution developed by some experimental groups, [3], [4], as a way to increase the intensity of the scattered radiation. Resulting from these techniques, the enhanced Raman intensity increases the spatial accuracy of the image, from μm to nm. This has been done by using a new experimental arrangement [4] instead of the usual micro Raman measurement, a metallic tip is set close to the sample, when the tip is illuminated by the incident radiation it gets polarized, and near the tip apex there is a huge charge accumu-

lation. As there are other material analysis equipment that makes use of tips, like STM (scanning tunneling microscopy) or AFM (atomic force microscopy), it is actually possible to do a simultaneous analysis by Raman tip enhanced imaging combined with tip equipped arrangements.

The enhancement effect is due to the near field generated in between the tip and the sample. Not only the resolution in Raman imaging was greatly increased, but also new peaks appeared in the tip enhanced Raman spectra, as seen in [4]. This is extremely intriguing because these are related to SWNT (single walled nanotubes) vibrational modes that were unknown. Identifying and explaining them is a a whole new deal.

Although this phenomenon has been measured, observed and used experimentally, it has not been explained in detail theoretically. Since the Raman intensity depends on the interactions between the analysed sample carriers, the electrons, with the incident radiation, photons, and the quanta of mechanical vibrations in the sample lattice, phonons, the usual explanation for the enhancement could be to calculate a modified electron-photon and electron-phonon interactions matrix elements. But this is not the case. In SWNTs this happens at room temperature due to the one dimensional character of the SWNT, when an electron is excited from the valence band to the conduction band leaving a positive charged hole in the valence band, they are still bounded together by a Coulomb even at room temperature. This pseudoparticle, the exciton, interacts with the incident radiation near field components which adds its contribution for the Raman Spectra as it will be seen in this thesis later.

What is the near field component of the incident radiation mentioned before? It is the localized component, that is a non propagative radiation in a very small region, $kr << 1$, k is the wave vector while r is the distance from the radiation source. The near field is dominant because it has an amplitude decay dependence of $1/r^3$ whereas the far field has one of $1/r$.

The so called near field component from the electromagnetic radiation is the con-

tribution that arises from the region about the irradiating source, its amplitudes diminishes with increasing distance, r, with a $\frac{1}{r^3}$ dependence. This has a special property, since the amplitude will disappear very quickly away from the neighborhood of the radiation source, this energy will be localized on the same aforementioned region. As for the far field component, in which the amplitude decreases with $\frac{1}{r}$, therefore having negligible contribution close to the radiation source, opposing to the near field component, the far field one swipes energy away from the radiation source the localized near field is of a far greater important role than the far field because its amplitude is larger. The tip-enhanced Raman spectroscopy (TERS) makes use of the near field generated by a metallic tip such as Ag or Au, as a spectroscopy imaging technique for single wall carbon nanotubes (SWNT) [5]. So now what remains to be explained is the SWNT, which is as if a graphene slice, rectangular, would be rolled up as a cylinder and had its two extremities glued together. However, differently from the graphene, that does not have a variety of types, graphene slices are all identical unless discussing about their dimensions and edges. That is not so for the carbon nanotube, depending on how the graphene slice is rolled up and glued, the properties of this cylinder are completely unique.

The enhancement seen in the Raman spectra [5, 6] has been explained as a result from the near field component of the radiation around the metallic tip and sample by Hartschuh *et al.* This was verified by varying the tip apex and sample distance in the 5 to 10nm range [5]. The scattered radiation near field component dominates, even compared to the incident radiation amplitude, this was done by use of the finite difference time domain method (FDTD) [7] which even tough is not the focus of this thesis, is based on mesh to mesh interactions with the consideration of discrete time, this is to obtain the the charge accumulation on the tip apex generated field oscillations in time.

Although it is accepted that the near field component of the radiation gives the major contribution to the Raman spectra enhancement, this enhancement phenomenol-

ogy and calculation has not been thoroughly discussed. From this point of view an explanation and quantitative prediction for the Raman spectra and the near field exciton interaction in SWNT is of great importance and usefulness as a mean to aid experimentalists in pursuit of better resolution of nanodevices, that could use this work as a prediction to find out the best wavelengths, materials, tip shapes [8, 7], and other parameters in their tip enhancement spectroscopy.

Chapter 2

Background

2.1 Carbon Nanotubes Fundamentals

The single wall carbon nanotube (SWNT) is a one dimensional material, that is, its structure has only one degree of freedom, the usual description of it is made by imagining a single atom graphene slice and rolling it up as a cylinder by gluing its ends together. In regard of the carbon atom orbiting electrons it has a $2s$ valence electron and two other $2p$ ones, this is the configuration of the graphene sheet, that has 3 sp^2 hybridization orbitals, therefore the bonds between the carbon atoms in graphene are all covalent with their 3 nearest neighbors forming a hexagonal grid [9, 10].

Ahead is figure 2-1, where $\boldsymbol{C}_h = n\boldsymbol{a}_1 + m\boldsymbol{a}_2 = (n, m)$, this is the chiral vector, it points in the direction of the SWNT chirality (n, m), it is defined by the unitary cell vectors from graphene $\boldsymbol{a}_1 = \left(\frac{\sqrt{3}}{2}, \frac{1}{2}\right)a$ and $\boldsymbol{a}_2 = \left(\frac{\sqrt{3}}{2}, -\frac{1}{2}\right)a$, the crystalline structure constant is $a = 0.246$ [9].

Taking the example of the figure ahead which has a $\boldsymbol{C}_h = (4, 2)$ other important properties are directly obtainable from the two integers (n, m) such as; the carbon nanotube diameter, $d_{\mathrm{t}} = a\sqrt{n^2 + nm + m^2}/\pi$ and the chiral angle, $\tan\theta =$

Fig. 2-1: fig:/fig:SWNT-Ch.eps

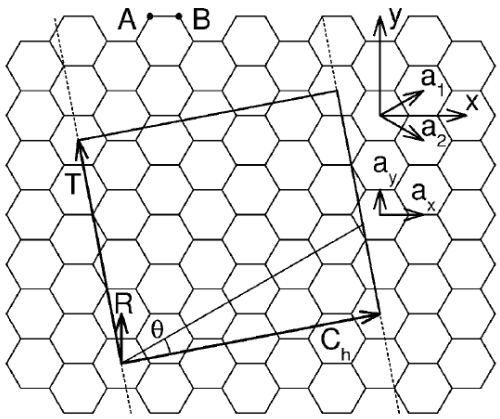

Figure 2-1: **Chiral index C_h and the unrolled unit cell of $(4, 2)$ carbon nanotube [11].** The x and y axes are defined in armchair and zigzag direction. The $\boldsymbol{a}_1$ and $\boldsymbol{a}_2$ are unit lattice vectors from the graphene lattice. The rectangle defined by $\boldsymbol{C}_h$ and $\boldsymbol{T}$ is the unrolled unit cell of the carbon nanotube.

$\sqrt{3}m/(2n+m)$ [9].

It is possible to classify SWNTs depending on their chiralities since their physical properties also depend on it. For the $n = m$ that define a chiral angle of $\theta = \pi/6$ SWNTs, armchair nanotubes because of their same shaped edges. In the case of $n \neq 0$ and $m = 0$ defining a chiral angle of $\theta = 0$ the nanotube edges are in zigzag.

These two types of SWNTs are achiral ones, since they cannot be completely defined by translating and repeating the unitary cell in the chiral angle direction.

However, there is a chiral nanotube, that has a chiral angle in between the armchair and zigzag ones, $0 < \theta < \pi/6$, the translational vector for this type is $\boldsymbol{T} = t_1\boldsymbol{a}_1 + t_2\boldsymbol{a}_2 = (t_1, t_2)$ where $t_1 = \frac{2m+n}{d_R}$ and $t_2 = -\frac{2m+n}{d_R}$. d_R is obtained by $d_R = \gcd(2n + m, 2m + n)$ where gcd is a function that has the greatest common divisor as its image set. Considering the armchair nanotube (n, n) as an example the $d_R = (3n, 3n) = 3n$, therefore the translational vector is $\boldsymbol{T} = (1, -1)$.

From the unitary cell other properties are now obtainable, they are: the number of graphene grids and the number of carbon atoms. Respectively N is calculated by the area of the carbon nanotube unitary cell $|\boldsymbol{C}_h \times \boldsymbol{T}|$ divided by the area of the graphene grid , $|\boldsymbol{a}_1 \times \boldsymbol{a}_2| = \sqrt{3}a/2$, finally $N = 2(n^2 + nm + m^2)/d_R$. As for the

number of carbon atoms, it is important to state that the two carbon atom types in the graphene grid are different, and this difference arises from the orbitals bonding as a result, the number of carbon atoms is $2N$, so for the $(4, 2)$ SWNT with $d_R = 2$ and $N = 28$ there are 56 carbon atoms in this chiral SWNT unitary cell.

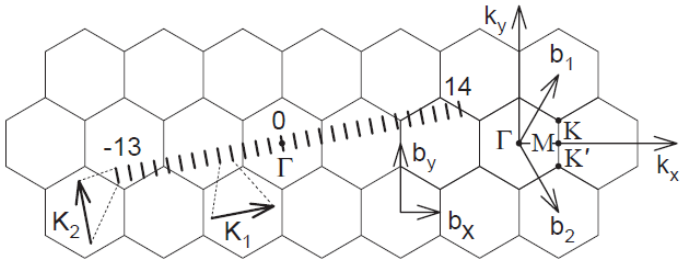

Figure 2-2: **Reciprocal lattice of graphene for a chiral nanotube (4,2) with its cutting lines [11].** $\boldsymbol{b}_1$ and $\boldsymbol{b}_2$ are the reciprocal unitary vectors from the graphene lattice. The high symmetry points, Γ, M, K and K', are defined as the center, the middle and the corners of the first Brillouin zone of the graphene lattice, respectively. As for $\boldsymbol{K}_1$ and $\boldsymbol{K}_2$, the reciprocal lattice unitary vectors for the carbon nanotube in circumferential and tube axis directions correspondingly. The cutting line index μ ranges from -13 to 14 passing through Γ point at $\mu = 0$. The number of cutting lines is the number of graphene lattices in a carbon nanotube unit cell.

Regarding the electronic properties of carbon nanotubes, they can be obtained in the reciprocal space, which can be constructed from the graphene's one, as shown in Fig. 2-2. The reciprocal lattice unitary vectors from graphene $\boldsymbol{b}_1$ and $\boldsymbol{b}_2$ come from the restriction, $\boldsymbol{a}_i \cdot \boldsymbol{b}_j = 2\pi\delta_{ij}$ then

$$\boldsymbol{b}_1 = \left(\frac{2\pi}{\sqrt{3}}, 2\pi\right)\frac{1}{a} \quad \boldsymbol{b}_2 = \left(\frac{2\pi}{\sqrt{3}}, -2\pi\right)\frac{1}{a} \tag{2.1}$$

Which will be used to obtain the carbon nanotube reciprocal lattice vectors, $\boldsymbol{K}_1$ and $\boldsymbol{K}_2$ from a restriction similar to the previous one, $\boldsymbol{C}_h \cdot \boldsymbol{K}_1 = \boldsymbol{T} \cdot \boldsymbol{K}_2 = 2\pi$ and $\boldsymbol{C_h} \cdot \boldsymbol{K}_2 = \boldsymbol{T} \cdot \boldsymbol{K}_1 = 0$. $\boldsymbol{K}_1$ will be in the $\boldsymbol{C}_h$ direction while $\boldsymbol{K}_2$ will be in the $\boldsymbol{T}$ direction , with lengths $|\boldsymbol{K}_1| = 2/d_t$ and $|\boldsymbol{K}_2| = 2\pi/T$ the circumferential and tube axis directions.

Fig. 2-2: fig:/fig:SWNT-reciprocal.eps

As the number of unit cells is very big and the whole graphene grid is a repetition of the unit cell, the use of the periodic boundary conditions is in order, with the same amount of discrete wave vectors as the number of unit cells, N, they are defined in the circumferential direction in a symmetric interval as $1 - \frac{N}{2} < \mu < \frac{N}{2}$ as $\mu \boldsymbol{K}_1$, cutting lines, as shown in Fig. 2-2 . However, in the tube axis they are continuous and range from $-\pi/T$ to π/T in the first Brillouin zone.

A very fundamental property from SWNT comes from the calculation of the energy dispersion relation of the electrons, a consequence of the aforementioned periodic boundary conditions is the zone-folding method which is justified again by the repetition of the unit cell encountered all across graphene and SWNT grids.

$$\boldsymbol{k} = \mu \boldsymbol{K}_1 + k \frac{\boldsymbol{K}_2}{|\boldsymbol{K}_2|} \quad \text{with} \quad \mu = 1 - N/2, ..., N/2 \quad \text{and} - \frac{\pi}{T} \leq \frac{\pi}{T}. \tag{2.2}$$

The energy dispersion of graphene is obtained by applying the zone-folding scheme [10], from which the SWNT one is obtained, by the use of periodic boundary conditions the wave vector associated to $\mathbf{C}_h$, becomes quantized, the cutting lines go on following the chiral direction, $\boldsymbol{K}_1$ in the reciprocal space [12] and so do the electronic energy dispersion following along the cutting line μ of carbon nanotube is [9]

$$E_\mu(k) = E_{g2D}\left(\mu \boldsymbol{K}_1 + k \frac{\boldsymbol{K}_2}{|\boldsymbol{K}_1|}\right), \quad \left(\mu = 0, ..., N - 1 \text{and} - \frac{\pi}{T} < k < \frac{\pi}{T}\right), \tag{2.3}$$

E_{g2D} is the electronic energy dispersion of graphene keeping in mind that the $+$ is for the π bond and the $-$ is for the π^* anti-bonding, [10]

$$E_{g2D} = \frac{\epsilon_{2p} \pm tw(\mathbf{k})}{1 \pm sw(\mathbf{k})} \tag{2.4}$$

which was obtained by use of the simple tight binding method (STB), an approximation in which only the nearest carbon atoms interactions are considered. t is the nearest neighbour transfer integral, $\langle \phi_{\mathrm{A}} | H | \phi_{\mathrm{B}} \rangle$, where the indexes A and B denote

the different orbital bonding carbon atoms. s is the overlap integral of both atoms, $\langle \phi_{\mathrm{A}} \,|\, \phi_{\mathrm{B}} \rangle$. And finally,

$$w(\mathbf{k}) = \sqrt{|f(\mathbf{k})|^2} = \sqrt{1 + 4\cos\frac{\sqrt{3}k_x a}{2}\cos\frac{k_y a}{2} + 4\cos^2\frac{k_y a}{2}} \tag{2.5}$$

Now going back to the (4,2) SWNT energy dispersion relation from Eq. 2.3 after zone-folding, and checking Fig. 2-3 [11] it is possible to visualize the dimension difference from the graphene and the SWNT density of states (DOS).

The discrete cutting lines μ index are also shown with the high-symmetry points, from this figure it is also possible to obtain a very important conclusion. At the K point the valence and conduction bands clearly touch, that is a degeneracy where there is no energy gap. A SWNT with such a chirality that contains K passing cutting lines is a metallic SWNT, while the opposing case is semiconducting, because it will have a band gap between the π and π^* bands.

Not only being semiconducting they can still be divided into two cases, S1 and S2, are defined as $\mathrm{mod}(2n+m, 3) = 1$ and $\mathrm{mod}(2n+m, 3) = 2$, and the previously explained metallic case has $\mathrm{mod}(2n+m, 3) = 0$ [10]. As for the (4,2) example SWNT shown in Fig. 2-3 is a S1.

Another very relevant feature, especially if Raman spectroscopy is taken into account, is the DOS peaks, van Hove singularities (vHS) [10]. This is the same case that was used to explain the metallic SWNT, when the π and π^* bands touch in a high symmetry point [13].

When the incident light energy is equal to the gap between the conduction and valence bands at the vHS there can be a transition of an electron, in the case of a light polarization in the same direction as the tube axis, the transition will be vertical with the same cutting line index μ from the valence to the conduction band. This transition is labelled $\mathrm{E}_{\mu\mu}$, while in the case of a light polarization perpendicular to the tube axis the transition electron will end up in a different μ index cutting line.

Fig. 2-3: fig:/fig:SWNT-dispersion.eps

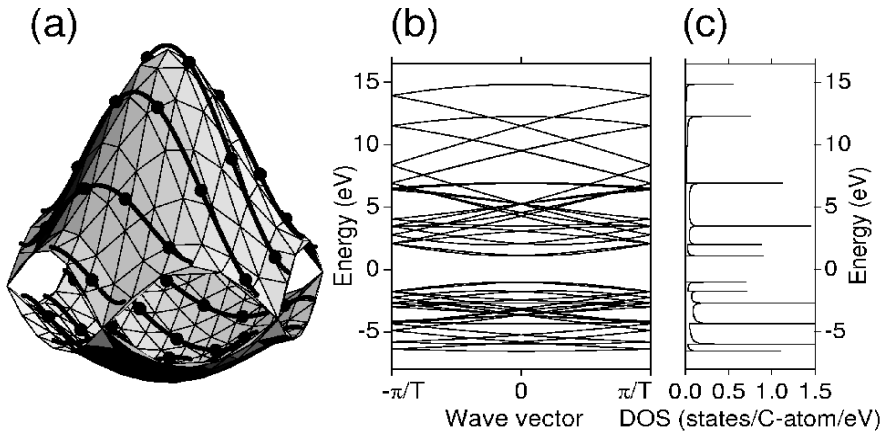

Figure 2-3: **The electronic energy dispersion and DOS of (4,2) carbon nanotube from zone-folding scheme [11].** (a) Valence band (π) and conduction band (π^* band) of graphene's Brillouin zone. The thick cutting lines of (4,2) carbon nanotube after zone-folding, and the solid dots as the end of the cutting lines. (b) The electronic energy dispersion of (4,2) carbon nanotube after zone-folding. (c) The electronic density of state (DOS) per energy per carbon atom of (4,2) carbon nanotube. The peaks from DOS are the van Hove Singularities (vHS).

The following figure 2-4 shows vertical transitions closest to the K point E_{11}, and higher energy vertical transitions in visible region are called E_{22} and E_{33}. The plot of these vertical transition energies by the SWNT is a Kataura plot [2]. This is a prelude of the discussion following the electron transitions, the origin of excitons in SWNT.

2.1.1 Excitons in SWNTs

When the electron makes a transition from the valence band into the conduction band it leaves the absence of a negative charge, being replaced my a positive charged hole, however this hole and the excited electron are closely bound by Coulombiam interaction, and together they are a pseudo-particle called exciton, it is a pseudo particle since its lifetime is of the order of nanoseconds [15].

Fig. 2-4: fig:/fig:exciton-Eii-Jiang.eps

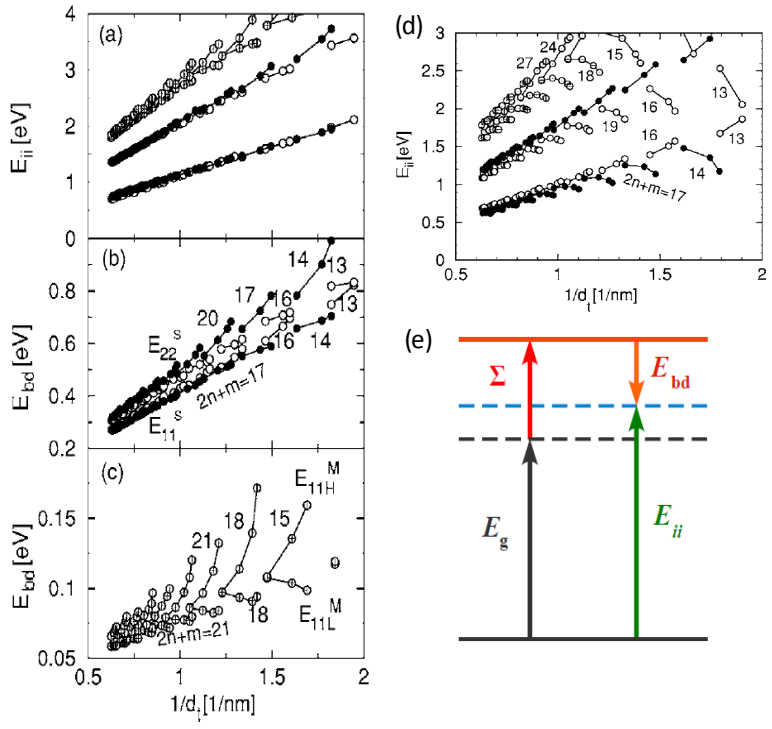

Figure 2-4: **Transition energy E_{ii} and binding energy E_{bd} Kataura plot.** For figures (a), (b) and (c) the simple tight binding (STB) method was used, open, filled and crossed circles are for S1, S2 and metallic SWNTs (a) Exciton transition energy E_{ii} as a function of the inverse of diameter d_t. [2]. (b) Binding energy E_{bd} by the inverse of diameter d_t. [2]. (c) Binding energy E_{bd} of metallic SWNTs as a function of inverse of diameter d_t [2]. (d) Exciton transition energy E_{ii} from the extended tight binding (ETB) method by the inverse of diameter d_t. [2]. (e) Exciton theory correction of the transition energy E_{ii} . The energy gap E_g of single-particle model is added to a positive self energy Σ, and from that the binding energy E_{bd} is subtracted [14].

To generate an exciton no more than 1 eV is needed [10, 2], as it is a two-body system, the wave-vectors on each cutting line is not well defined. The study of the exciton has been done as a solution sought to the ratio inconsistency that exists between the E_{22}/E_{11} of semiconducting SWNTs and predicted by STB method, also it doesn't match the experimental data since the transition energy has a weak dependence on the chiral angle from STB [16]. Which is incoherent with the experimental data from

the Kataura plot showing a range from the $(2n + m)$ family in [17]. The exciton transition energy E_{ii} depends on the electron-electron and electron hole interactions which makes the self-energy, Σ, and the binding energy, E_{bd}, bigger than zero, as can be seen in Fig. 2-4(e) [14]. Nevertheless, J. Jiang et al. have investigated a exciton transition energy E_{ii} from STB method with a weak spread on chirality, $\mathbf{C}_{ch}$, in Fig. 2-4(a) [2]. This was untangled by the extended tight binding method (ETB) where the π and σ orbitals are combined, and as a result the bond length and tube structure are taken into account with greater accuracy [10]. By ETB the transition energy E_{ii} relation to the chiral angle is properly explained in Fig. 2-4(d) [2] which matches the data from [17]. Further on, the binding energy E_{bd} with its dependence to the SWNTs diameter and chirality for semiconducting and metallic SWNTs are in Fig. 2-4(c) and Fig. 2-4(d).

This photo-luminescence (PL) experiment with two photons was key to confirming the excitonic effect in the optical transitions in the SWNTs, from J. Maultzsch et al. [18]. Firstly the one photon PL in the one particle picture, where the electron is excited to make an E_{22} transition to the conduction band, after the relaxation from this electron it makes another transition, this time E_{11} emission to the valence band, which can be seen in Fig. 2-5(a). As for the exciton picture, the photon energy is transferred to the $1u$ exciton to do a E_{22} transition. Following this excitation the same exciton then relaxes to the $1u$ state by a E_{11} photon emission which happens due to the collapse of the exciton, that is the recombination of the electron and hole. Nevertheless, the PL two photons experiment in Fig. 2-5(b) there is an usually optically inactive $2g$ exciton(dark), in one photon PL. When excited, this $2g$ exciton then relaxes to a $1u$ exciton with energy from the E_{11} transition, making a final one photon emission by collapsing into the electron hole recombination. The energy difference between $2g$ and $1u$ excitonic states is due to the intensity of the Coulombiam interaction, that it didn't occur as a consequence of the excitonic effects would equalize

Fig. 2-5: fig:/fig:exciton-2photon.eps

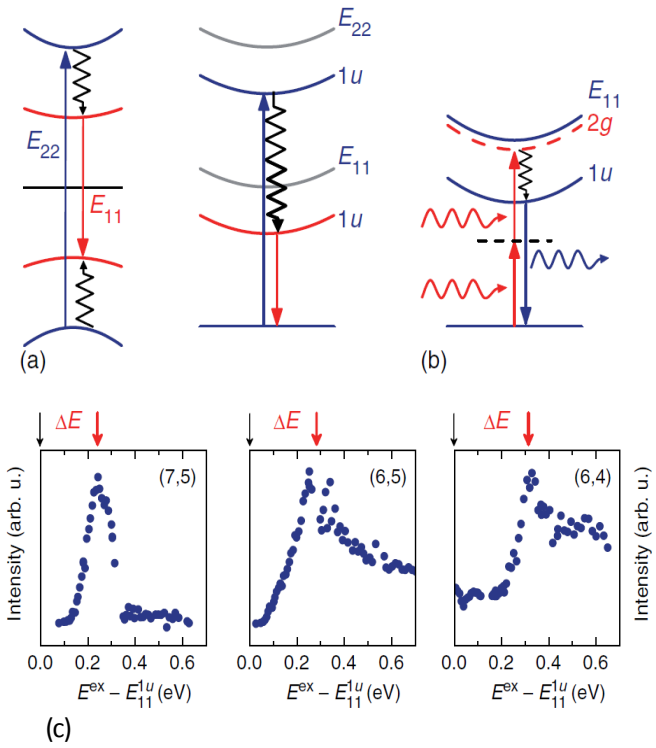

Figure 2-5: **Photo-luminescence (PL) experiment in SWNTs with two photons, from [18]** (a)In the left picture there is one photon PL process in the one particle picture while in the right one there is one photon PL process as well but in the exciton picture where the $1u$ exciton is optically allowed. (b) Two photon PL experiment where $2g$ exciton becomes optically allowed, in opposition to the one-photon PL experiment where it is not optically active. (c) Luminescence as a function of two photon excitation energy for (7,5), (6,5) and (6,4) SWNTs. The black arrows indicate the one photon emission energy from the $1u$ exciton E_{11}^{1u} whereas the red arrows point to the two photon absorption maximum where E_{11}^{1g} is written.

the one and two photons allowed states energies [18]. Yet by plotting the emission intensity as a function of $\mathrm{E^{ex}} - \mathrm{E_{11}^{1u}}$ where $\mathrm{E^{ex}}$ is an excitation energy in Fig. 2-5(c), the intensity peak of each chirality has been observed in range 240 - 325 meV, this is the two photons allowed $\mathrm{E_{11}^{2g}}$ state. As for the exciton binding energy $\mathrm{E}_{bd} = \mathrm{E_{11}^{2g}} - \mathrm{E_{11}^{1u}}$ from this maximum point, matching the first principle calculation [18].

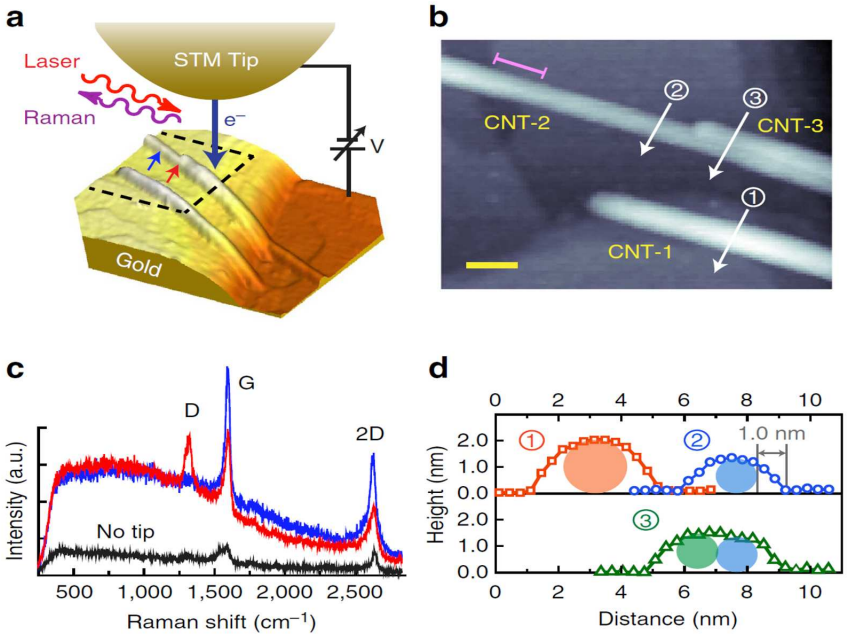

Figure 2-6: **The schematic experimental setting up of a STM TERS experiment** (a) Model of the Scanning Tunnelling Microscopy tip close to the sample over a golden bulk, displaying the influx of electrons direction and the incident radiation and Raman scattering, over the carbon nanotubes CNTs bundle [4]. (b) STM image of the bundled 3 CNTs . (c) The Raman spectra comparison with and without tip, with the modes of vibration labels over the 3 peaks (d) Dimensions of the CNTs predictions based on the STM TERS imaging

2.1.2 Tip enhanced Raman spectroscopy (TERS)

As aforementioned the TERS experiment can be made in experimental arrangements that already contain a tip, like scanning tunnelling microscopy (STM) on Fig.2-6 which is the case in [4], atomic force microscopy (AFM) and others.

In Fig. 2-6 case the topographic imagining was done while taking the Raman spectra, the result is enlightening, since it even uncovers phonon vibrational modes peaks that were not measurable with the lower scattered light intensity from before. An usual configuration between most of the TERS experiments is a sharp metallic conic shaped tip put at a small distance above the sample. Yet there are two categories: based on the transparency property of the sample [19] as : (i) on-axis illumination

Fig. 2-6: fig:/TERS-stmsetup.eps

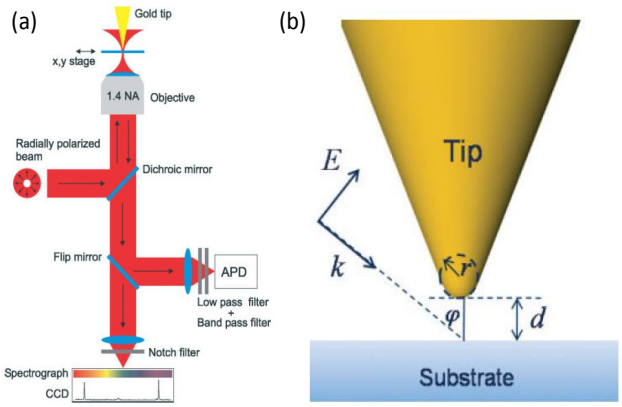

Figure 2-7: **The schematic experimental setting up of a TERS experiment** (a) On-axis illumination of the metallic tip using radially polarized laser beam through the transparent sample. This near field experiment can't be made on a non-transparent sample [20]. (b) Side illumination of the metallic tip using the linearly polarized laser light. This configuration can be utilized with the sample on the non-transparent substrate [7].

shown in Fig. 2-7(a) and (ii) side illumination shown in 2-7(b). In the latter case the TERS experiment is on the on-side illumination scheme utilized by L. G. Cançado et al. [20].

The setup above in Fig. 2-7(a) has a gold tip in which the tip apex is approached as a sphere of about 20 nm diameter produced by electrochemical etching on the x,y plane. The separation distance between the tip apex and the sample is controlled by a quartz tuning fork attached to the it.Radially polarized laser beam or a linearly polarized beam is focused on the sample using a high numerical aperture objective (1.4NA), and the gold tip is aligned with the beam's focus. The optical signal follows to be collected by the same objective and detected either using a single photon counting avalanche photo-diode (APD), or by the combination of a spectrograph and a cooled charge-coupled device (CCD) [20]. In both cases, the tip enhanced Raman image is captured at the same time as the topographic image by raster scanning the sample [20]. The use of a linearly polarized laser with wavelength 632.8 nm and

Fig. 2-7: fig:/TERS-setup.eps
Fig. 2-8: fig:/TERS-result-Cancado.eps

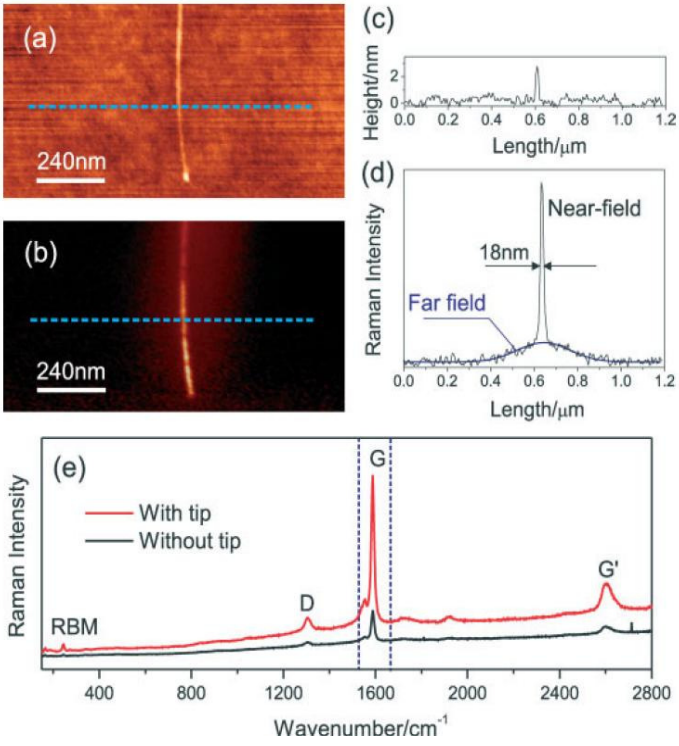

Figure 2-8: **Experimental results from TERS in on-axis illumination scheme [20]** (a) Topographic image of the carbon nanotube bundle on a glass bulk. (b) TERS imaging of carbon nanotube bundle on glass. (c) High profile of the carbon nanotube bundle taken along the dashed blue line of the topographic image. (d) Raman intensity of the carbon nanotube bundle along the dashed blue line of the TERS image. (e) The Raman intensities as a function of Raman shift measured with and without the gold tip are distinguished by the red and black spectra, respectively. The integration region of the G band Raman intensities is indicated by the vertical dashed lines.

fixing the gold tip about 2 nm above a carbon nanotube bundle on a glass bulk, as shown in Fig 2-8(a). The carbon nanotube bundle taken along the dashed blue line in the topographic image is shown in Fig 2-8(c). From the topographic image, the diameter of the carbon nanotube bundle was estimated as 2.5 nm. The Raman intensity measured along the dashed blue line of the TERS image in Fig 2-8(d). From the Raman intensity, the spatial resolution of the near field is obtained as 18 nm, and the resolution of the far field fitted with Gaussian function is about 290 nm. The resolution of the TERS image is close to the diameter of the tip. All this considered,

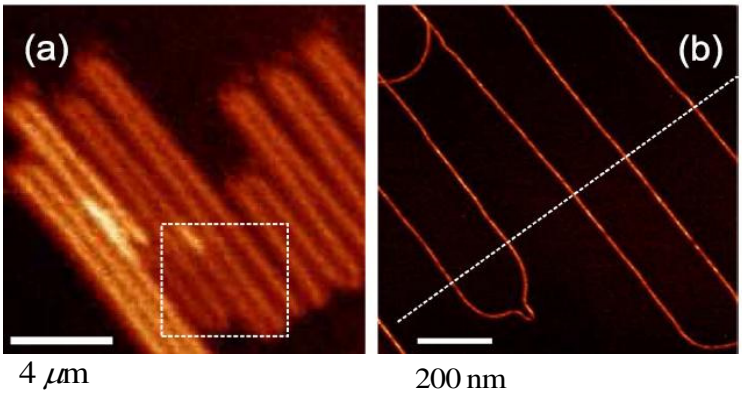

Figure 2-9: **Conventional and tip-enhanced Raman images of a self-organized semiconducting carbon nanotube serpentine done by L. G. Cançado et al. [21]** (a) Raman image around the G band intensity. (b) Tip enhanced Raman image around G band intensity by raster scanning the gold tip at distance 2 nm above the carbon nanotube within the square area enclosed by dashed square in the non-enhanced Raman image. (c) Raman intensity taken along the dashed line in the tip enhanced Raman image.

the measured Raman intensities as a function of Raman shift equipped with a tip by the red spectrum and without tip indicated by the black spectrum are shown in Fig 2-8(e). The near field enhancement of the Raman intensity can be seen from this figure. From the energy of RBM mode $\underline{\omega_{\mathrm{RBM}} = 245\ \mathrm{cm}^{-1}}$, the chirality of the SWNT was identified to be (10,3) semiconducting SWNT, whose E_{22} transition resonances with the energy of laser light.

The TERS experiment have been done for a self-organized semiconducting carbon nanotube serpentine by L. G. Cancado et al. [21]. Conventional and tip enhanced Raman images acquired from the G band intensity are in Fig. 2-9(a) and Fig. 2-9(b). The tip-enhanced Raman image has much higher resolution than the usual Raman image, which has a low resolution. The spatial resolution of the TERS image is of 25 nm as shown in Fig. 2-9(c).

Fig. 2-9: fig:/TERS-result-Cancado2.eps

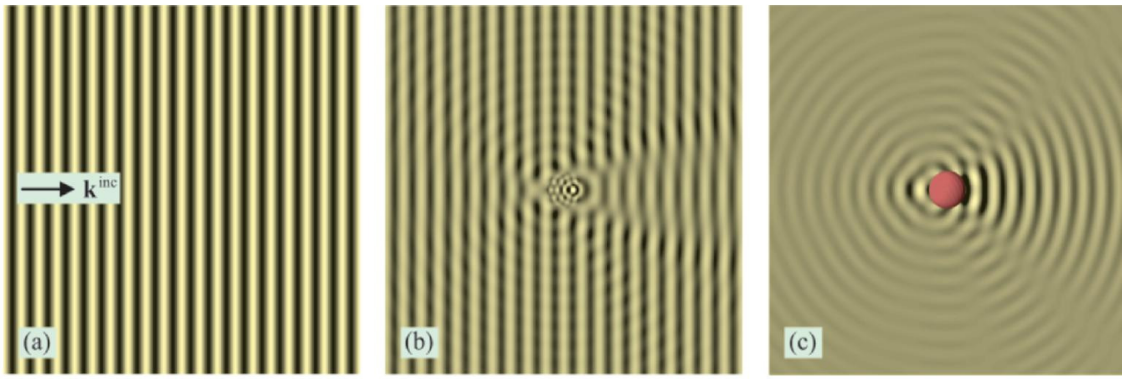

Figure 2-10: **The illustration of the scattering of light by a spherical particle [22]** (a) Real part of the incident electric field traveling from the left side to the right side in non absorbing dielectric medium. (b) Real part of total electric field which is the summation of the incident electric field and the scattered electric field radiated from the spherical particle with real refractive index n=2.8 at the center of the figure. (c) Real part of the scattered electric field by the spherical particle at the center of the figure.
Caution : The color scale of each figure is different.

2.1.3 Scattering of light by a metallic sphere

Since the metallic tips used in TERS experiments was approximated as spheres, in order to understand the radiation behavior around the region between the tip and sample, the radiation scattering by a sphere has to be considered.

The scattering produced by a sphere is similar to the so called elastic scattering, also known as Rayleigh scattering, but this one was done in detail by Mie, and is called Mie's scattering.

This results arise from the solution of Maxwell's equations in spherical coordinates, which give origin to the Helmholtz vector equations, for the electric and magnetic components [1].

Linearly polarized plane wave will be considered as the incident light, and by the separation of variables method, the solutions of the Helmholtz vector equations will be sought for any kind of dielectric material with the spherical shape. The concept

Fig. 2-10: fig:/Mie.eps

of the scattering of light by a dielectric spherical particle is illustrated in Fig. 2-10. The amplitude of the real part of the incident light travelling in the non absorbing dielectric medium is illustrated in Fig 2-10(a). When the finite volume of the spherical particle is at the center of Fig 2-10(a), it will be excited by the plane wave to radiate the scattered wave propagating out from the particle. The amplitude of the total electric field in the scattering process is shown in Fig 2-10(b). It can be seen that the total electric field near the particle is a spherical wave due to the superposition of the incident light and the spherically scattered wave. In Fig 2-10(c), the spherically scattered electric field is shown without the incident electric field.

2.1.4 Au and Ag Dielectric Functions

Besides the behavior of the radiation surrounding the tip apex spherical approximation and the sample, the way the field interacts with each kind of metal in the metallic tip from TERS experiments is also essential to get the full picture of the tip enhancement Raman phenomena, therefore, the study of the dielectric function is now introduced, so that the dissipation and penetration of the radiation inside the metal of tip might be fully understood.

An initial model to investigate how the free carriers inside metals behave when excited by an external electromagnetic field was developed by Drude. His model regards the electrons inside a solid metal as a free gas around their positively charged cores. They collide with each other constantly while moving around during their excitation caused by the electromagnetic field.

Considering the visible wavelength region used in the previously mentioned TERS experiments equipped with gold or silver tips this model is valid, yet that is not so when higher energies are used since, the electrons wandering around will actually make a transition from their valence band to a conduction band. For those higher energies a more elaborate model is required, the so called Lorentz model for interband transitions. With those two models, it is possible to get a reliable description, that

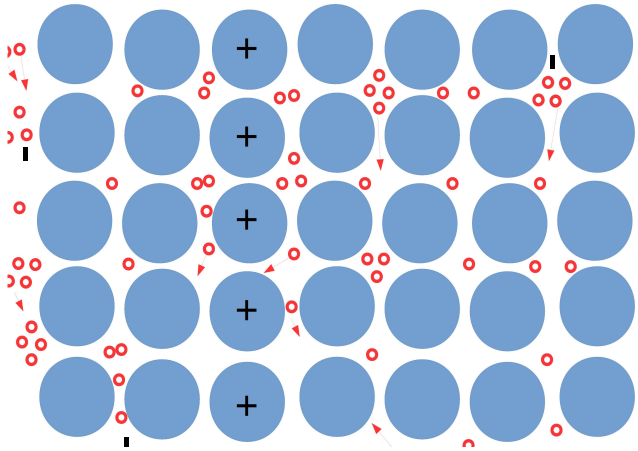

Figure 2-11: The positive cores, blue, surrounded by the colliding moving electrons in red

is supported by experimental observation.

Drude's model

This model assumes that the free electron gas has a finite value for the average relaxation time, τ, after colliding with each other.

It can be written as

$$\frac{\mathrm{d}\boldsymbol{p}(t)}{\mathrm{d}t} + \frac{\boldsymbol{p}(t)}{\tau} = \boldsymbol{f}(t), \tag{2.6}$$

where $\boldsymbol{p}(t)$ is the average momentum and $\boldsymbol{f}(t)$ is the driving force which can be either static or time dependent. Usually the average relaxation time, τ, of the electrons can be estimated from the DC resistivity, ρ_0, with $\tau = \frac{m}{ne^2\rho_0}$, where m is electron mass, n is conduction electron density and e is electron charge [23]. Considering the driving force $\boldsymbol{f}$ in Eq. (2.6) as the static electric field. At a temperature of, T = 373 K, the approximated relaxation time τ of Ag and Au are $\tau_{Ag} = 2.8 \times 10^{-14}$s and $\tau_{Au} = 2.1 \times 10^{-14}$s, respectively [23]. After that, the dielectric constant ε from Drude's model under a time dependent incident radiation, $\boldsymbol{E}_0 e^{-i\omega t}$, on the surface

Fig. 2-11: fig:/drudesmodel2.eps

of metal will be sought. The electric field inside the metal $\boldsymbol{E}$ oscillates in resonance with the external light, that is, $\boldsymbol{E}(t) = \boldsymbol{E}e^{-i\omega t}$. The driving force $\boldsymbol{f}(t)$ acting upon the electron become $\boldsymbol{f}(t) = -e\boldsymbol{E}e^{-i\omega t}$. Then, Eq. (2.6) becomes

$$m\frac{\mathrm{d}^2\boldsymbol{r}(t)}{\mathrm{d}t^2} + \frac{m}{\tau}\frac{\mathrm{d}\boldsymbol{r}}{\mathrm{d}t} = -e\boldsymbol{E}_0 e^{-i\omega t}, \tag{2.7}$$

where $\boldsymbol{r}(t)$ is the average electronic displacement. Eq. (2.7) can be solved by assuming that the average electronic displacement has the same time-harmonic response as the driving force, that is, $\boldsymbol{r}(t) = \boldsymbol{r}_0 e^{-i\omega t}$. By substituting this assumed time harmonic average displacement into Eq. (2.7), the amplitude $\boldsymbol{r}_0$ can be found. The displacement of the electron relative to the positive background, the positively charged core, gives rise to the electronic polarization $\boldsymbol{P}(t)$ defined as a number of electric dipole moments $\boldsymbol{\mu}$ per unit volume, $\boldsymbol{P}(t) = n\boldsymbol{\mu}(t) = -ne\boldsymbol{r}_0 e^{-i\omega t}$, where n is electronic density. Then, the electronic polarization is written in terms of the electric field inside the metal $\boldsymbol{E}_0$

$$\boldsymbol{P} = -\frac{(ne^2/m)\boldsymbol{E}_0}{\omega^2 + i\omega/\tau}. \tag{2.8}$$

Polarization of the positive background $\boldsymbol{P}_b$, which is non-resonant, since the positively charged core is too heavy to be moved by the external radiation source, may be included in the constitutive relation $\boldsymbol{D} = \varepsilon_0\varepsilon\boldsymbol{E} = \varepsilon_0\boldsymbol{E} + \boldsymbol{P} + \boldsymbol{P}_b$, where $\boldsymbol{E}$ is the local electric field inside the metal. Then, the electronic polarization $\boldsymbol{P}$ is written in terms of the local electric field $\boldsymbol{E}$ as $\boldsymbol{P} = \varepsilon_0(\varepsilon - \varepsilon_+)\boldsymbol{E}$, where ε_+ is defined as the dielectric constant of the positive background. The dielectric constant ε is

$$\varepsilon = \varepsilon_+ - \frac{\omega_p^2}{\omega^2 + i\omega\Gamma}, \tag{2.9}$$

The real part and the imaginary part of ε_i as a function of frequency is described as follows

$$\varepsilon_1 = \varepsilon_+ - \frac{\omega_p^2}{\omega^2 + \Gamma^2} \quad , \quad \varepsilon_2 = \frac{\omega_p^2\Gamma}{\omega(\omega^2 + \Gamma^2)}, \tag{2.10}$$

where $\omega_p = \sqrt{\frac{ne^2}{\varepsilon_0 m}}$ is the plasma frequency, the frequency with which each of the electrons when displaced from an equilibrium position about the positively charged core are restored to that position, and $\Gamma = 1/\tau$ is called the damping constant representing the scattering rate of the free electrons. The plasma frequencies and the damping constants of Ag and Au are shown in table 2.1. It can be seen that the plasma frequencies of gold and silver are very close to each other because number of conduction electrons per unit volume of gold and silver are nearly the same about $5.86 \times 10^{28}\,\mathrm{m}^{-3}$ and $5.90 \times 10^{28}\,\mathrm{m}^{-3}$, respectively [23]. The plasma frequencies ω_p of these two metals are in ultraviolet region. The damping constants of both two metals is small compared to the plasma frequency. From table 2.1, ε_1 and ε_2 of Ag

Table 2.1: The approximated relaxation time calculated from the DC resistivity at T = 373 K [23], the plasma frequencies and damping constants of Ag and Au

metal	$\tau(s)$	$\omega_p(eV)$	$\Gamma(eV)$
Ag	2.8×10^{-14}	8.99	0.148
Au	2.1×10^{-14}	9.02	0.197

and Au based on the Drude model calculated by Eq. (2.10) are shown in Fig 2-12. Here we plot the dielectric constants as a function of wavelength which is useful in spectroscopy. The range of the wavelength covers the visible region and ranges to the lower energies in the near infrared region as well as going to higher energies close to the ultraviolet region.

The real component, ε_1, from Ag and Au is negative, which is means it would decrease the phase of the transmitted radiation that went inside the metal, in visible and infrared regions and decreases as increasing the wavelength, since the energy is less than that of the plasma frequency ω_p. If the energy becomes larger than that of the plasma frequency ω_p as given in table 2.1, the ε_1 becomes positive, increasing the phase in this case since it causes dispersion, and if it is zero when the energy of laser light is the same as the plasma frequency. If the energy of laser light is

Fig. 2-12: fig:/eps1Drude.eps

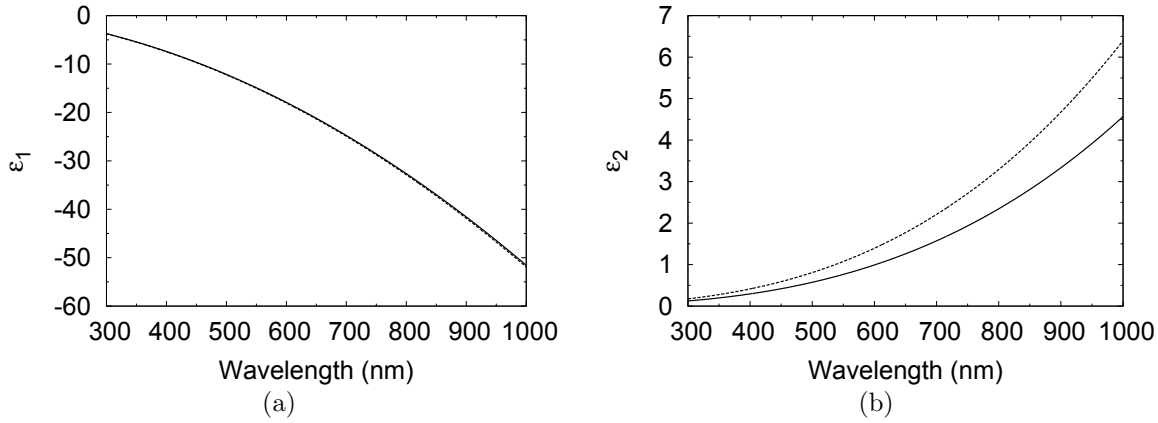

Figure 2-12: **Dielectric constant of Ag and Au from Drude, solid and dashed lines, respectively [24] :** (a) Real component from the dielectric constant of Ag and Au based on the parameters from table 2.1 (b) Imaginary component from the dielectric constant of Ag and Au based on the parameters from table 2.1.

large compared to the plasma frequency ω_p, ε_1 becomes ε_+ which corresponds to the dielectric constant of the positive background. It should be noted that the ε_1 of Ag is nearly the same as Au in infrared region including higher energy regions, and it is also the case for low energy region of the wavelength in μm scale. ε_2 opposing ε_1 is always be positive in the whole spectrum as there is no the negative term in its expression.However, ε_2, vanishes for energies greater than the plasma frequency ω_p. The absolute value of ε_2 is small compared to the absolute value of ε_1 as it is verifiable if ε_2 is approximated by $\varepsilon_2 \approx (\frac{\omega_p^2}{\omega^2})(\frac{\Gamma}{\omega})$ when the damping constant is neglected. Regarding the visible region, in which the energy is smaller than the plasma frequency, the approximated ε_2 becomes very small in spite of the amplitude of ε_1 which can also be approached as $\varepsilon_1 \approx (\frac{\omega_p^2}{\omega^2}) - 1$ by neglecting the damping constant. These behaviors of the dielectric constants play a relevant role in the resonance of surface plasmons in metals. When the energy of the incident light is increased and the electrons are strongly excited, a quantum effect contributes to the dielectric constant by the transition of the free electrons from the valence band to the conduction band,

so called the interband transition. This phenomena can be understood by the Lorentz model described in next the section.

Interband transition and the Lorentz model

Electrons in noble metals can make an interband transition from the filled valence band, d-band, to the empty conduction band, s-band, if the excitation energy of the laser light matches with the energy gap. Therefore, the contribution from an interband transition to the dielectric constant depends on the band structure of each metal. The transition edges of Ag calculated from the relativistic augmented plane wave method are at 3.98 eV , 311.6 nm, and 3.45 eV, 359.4 nm, [25]. Meaning that the interband transition does not contribute to the dielectric constant of Ag in the visible and lower energy regions. Nevertheless, the absorption edges of Au are at a wavelength of 470 nm and 330 nm [26]. As a result, the effect of the interband transition can not be neglected in visible region for Au.

This model considers that the electron is connected with the positive nucleus by the spring with the force constant $k = m_e\omega_0^2$ forming the dipole oscillator or the Lorentz oscillator. The dipole oscillates at natural frequency ω_0, if no external force or damping is present, or it can be damped since the electron has a finite life-time through the collisions. When the laser light of frequency ω shines over the atom, the electron is displaced from its equilibrium position by the driving force $-eE(t)$ while the nucleus is considered as fixed relatively to the electron, since its huge mass is many times bigger than that of the electron. After being displaced from the equilibrium position, the electron is then influenced by the restoring force, according to Hook's law $-m_e\Gamma\frac{\mathrm{d}x}{\mathrm{d}t}$, and a damping force $-m_e\omega_0^2 x$, starting to vibrate at the same frequency as the external light wave. The Lorentz model is shown in Fig. 2-13. The equation

Fig. 2-13: fig:/Lorentz-model2.eps

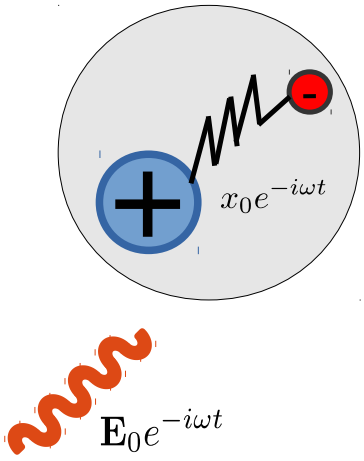

Figure 2-13: The geometry of the Lorentz model. The electron is connected to the nucleus by the spring forming the Lorentz oscillator. The oscillator starts vibration when there is the time-harmonic driving force due to the electric field $E_0 e^{-i\omega t}$ applied to the atom.

of motion for the electronic displacement x

$$m_e \frac{\mathrm{d}^2 x}{\mathrm{d}t^2} + m_e \Gamma \frac{\mathrm{d}x}{\mathrm{d}t} + m_e \omega_0^2 x = -eE(t), \tag{2.11}$$

where m_e is mass of the electron, Γ is the damping constant, e is the electronic charge and $E(t)$ is the time-harmonic electric field. Assuming the time-harmonic dependence of the electric field as $e^{-i\omega t}$ implying in an electric field such as $E(t) = E_0 e^{-i\omega t}$. Considering also that the electron oscillates at the same frequency as the external light wave, that is, $x(t) = x_0 e^{-i\omega t}$. The amplitude x_0 is obtainable by substituting $x(t)$ and $E(t)$ into the Eq. (2.11).

$$x(t) = \frac{-e/m_e}{\omega_0^2 - \omega^2 - i\Gamma\omega} E(t). \tag{2.12}$$

Besides, there is an induced electric dipole moment $\mu(t) = -ex(t)$, due to the elec-

tronic displacement $x(t)$ written in Eq. (2.12). From that, the electronic resonant polarization P is obtained as the product of the electronic density, n, and the electric dipole moment $\mu(t)$, $P = n\mu(t)$. From the relation, $\mathbf{D} = \varepsilon_0\varepsilon\mathbf{E} = \varepsilon_0\varepsilon_+\mathbf{E} + \mathbf{P}_{\text{resonant}}$, where the dielectric constant of the positive background is introduced ε_+, the complex dielectric constant ε is expressed as follows:

$$\varepsilon = \varepsilon_+ + \frac{\omega_p^2}{\omega_0^2 - \omega^2 - i\Gamma\omega}, \tag{2.13}$$

where ω_p is the plasma frequency defined as previously, $\omega_p = \sqrt{\frac{ne^2}{\varepsilon_0 m}}$. The real and imaginary parts of ε, ε_1 and ε_2,

$$\varepsilon_1 = \varepsilon_+ + \frac{\omega_p^2(\omega_0^2 - \omega^2)}{(\omega_0^2 - \omega^2)^2 + (\Gamma\omega)^2} \quad , \quad \varepsilon_2 = \frac{\omega_p^2\Gamma\omega}{(\omega_0^2 - \omega^2)^2 + (\Gamma\omega)^2}. \tag{2.14}$$

The dielectric constant ε at low frequency, or, the static dielectric constant, denoted as ε_s is obtained by taking the angular frequency ω as zero, and so $\varepsilon_s = \varepsilon_+ + \omega_p^2/\omega_0^2$. At high frequency, the dielectric constant becomes its non-resonant background version entirely, ε_+. Furthermore, it is convenient to express the dielectric constant in terms of the wavelength, for spectroscopic purpose, the main focus of this thesis. The $\varepsilon_1(\lambda)$ and $\varepsilon_2(\lambda)$ defined by recalling the relation $\omega = 2\pi c/\lambda$. Introducing two new parameters, the wavelength of the plasma frequency, $\omega_p = 2\pi c/\lambda_p$, and the damping constant in the same dimension as the wavelength, also called the damping length, $\omega_\Gamma = 2\pi c/\lambda_\Gamma$. Then, ε_1 and ε_2 as a function of wavelength are

$$\varepsilon_1(\lambda) = \varepsilon_+ + \frac{(1/\lambda_p^2)(1/\lambda_0^2 - 1/\lambda^2)}{(1/\lambda_0^2 - 1/\lambda^2)^2 + (1/\lambda_\Gamma^2)(1/\lambda^2)} \tag{2.15}$$

$$\varepsilon_2(\lambda) = \frac{(1/\lambda_p^2)(1/\lambda_\Gamma)(1/\lambda)}{(1/\lambda_0^2 - 1/\lambda^2)^2 + (1/\lambda_\Gamma^2)(1/\lambda^2)}. \tag{2.16}$$

Fig. 2-14 shows ε_1 and ε_2 from the Lorentz model as a function of wavelength by assuming parameters such as, $\lambda_0 = 700$ nm, $\lambda_p = 137.9$ nm and $\lambda_\Gamma = 11.4$ μm.

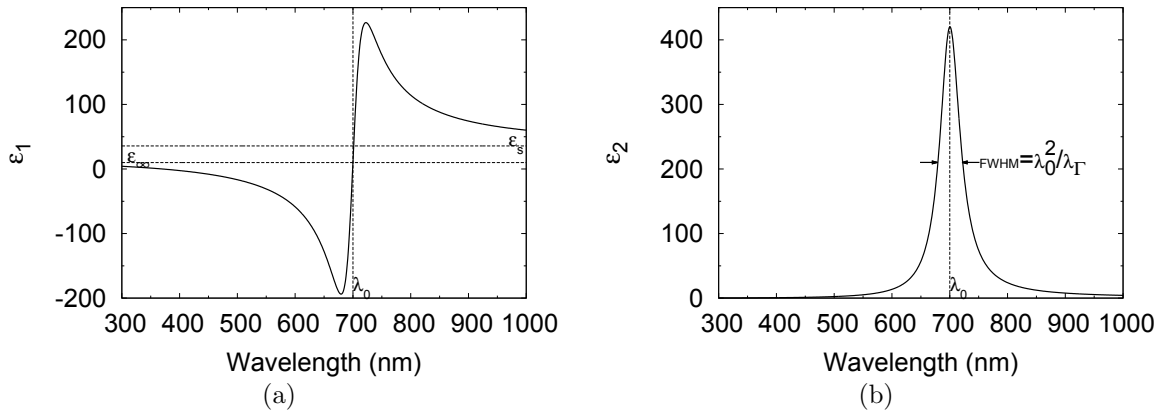

Figure 2-14: **Dielectric constant from Lorentz model [24]** (a) Real part of the dielectric constant, ε_1, as a function of the wavelength (b) Imaginary part of the dielectric constant, ε_2, as a function of the wavelength

The imaginary part, ε_2, gets to its maximum at $\lambda = \lambda_0$, and then sharply decrease to zero with any change taking the wavelength away from λ_0. The full width at half maximum, FWHM, of the broadening can be determined by considering the wavelength near λ_0, so that it can be approximated as $\lambda \approx \lambda_0$ and $1/\lambda_0^2 - 1/\lambda^2 \approx 2(\triangle\lambda)/\lambda_0^3$ where $\triangle\lambda = \lambda - \lambda_0$. The FWHM is $\lambda_0^2/\lambda_\Gamma$ as indicated in Fig. 2-14(b). The ε_1 at long wavelength is ε_s. It increases inversely with the wavelength toward λ_0 and finally get at its maximum at the wavelength, $\lambda = \lambda_0 + \frac{\lambda_0^2}{2\lambda_\Gamma}$, and then decreases suddenly when passing through λ_0, until approaching the negative minimum point at the wavelength of $\lambda = \lambda_0 - \frac{\lambda_0^2}{2\lambda_\Gamma}$. By lowering the wavelength more than the minimum point, ε_1 starts to increase again and reaches ε_+ at a very short wavelength.

Experimental dielectric constant for bulk metals

The bulk dielectric constants from Ag and Au in the energy range from 0.5 to 6.5 eV, at room temperature were measured by P.B. Johnson and R. W. Christy in 1972

Fig. 2-14: fig:/eps1Lorentz.eps
Fig. 2-15: fig:/expeps1.eps

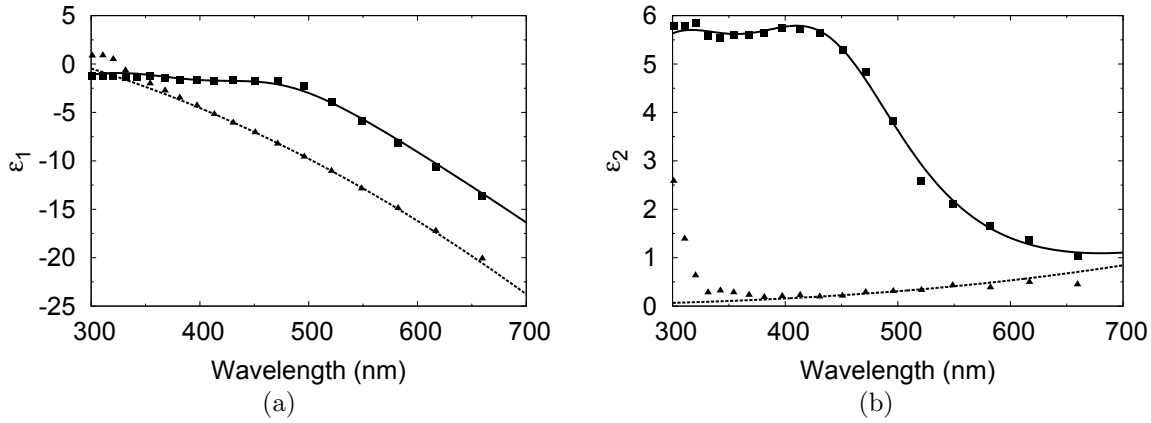

Figure 2-15: **Experimental dielectric constant** (a) The experimental ε_1 from Au and Ag are displayed by the solid rectangle and triangle while the fitting function for ε_1 from Au and Ag are plotted as the solid and dashed lines. (b) The experimental ε_2 from Au and Ag with the The fitting function of ε_2 [27, 28, 26].

[27]. These bulk dielectric constants are widely used. The experiment employed by Johnson and Christy was based on measuring the reflectance R and the transmittance T of a metallic thin film. The R is measured from the reflection at normal incidence. At the same time, T is measured from the transmission to the normal at an angle of 60°. These two quantities are converted into the complex refractive index n of the metal, by comparison with the theoretical expression describing R and T. Theoretically, the reflectance and transmittance are dependent of n, the refractive index of the surrounding dielectric media, the angle of incidence and the metallic thin film thickness [29]. Unfortunately, there are no analytical solution for the conversion from R and T to n. n solutions are therefore obtained numerically by a graphical method. After obtaining the complex refractive indexes, the complex dielectric constants ε are obtained by recalling the relation $n = \sqrt{\varepsilon}$ from the electromagnetic theory. The experimental ε_1 and ε_2 of Ag and Au are shown in Fig. 2-15 as a function of the wavelength in the range from 350 to 700 nm together with their fitting functions. The Au dielectric constant one has been given by P. G. Etchegoin et al [26], and is

as follows

$$\varepsilon_{\mathrm{Au}} = \varepsilon_{+} - \frac{1}{\lambda_p^2(1/\lambda^2 + i/\gamma_p\lambda)} + \sum_{i=1,2} \frac{A_i}{\lambda_i}\left[\frac{e^{i\phi_i}}{1/\lambda_i - 1/\lambda - i/\gamma_i} + \frac{e^{-i\phi_i}}{1/\lambda_i + 1/\lambda + i/\gamma_i}\right], \tag{2.17}$$

where $\varepsilon_{+} = 1.54$, $\lambda_p = 143$ nm, $\gamma_p = 14500$ nm, $A_1 = 1.27$, $\phi_1 = -\pi/4$ radian, $\lambda_1 = 470$ nm, $\gamma_1 = 1900$ nm, $A_2 = 1.1$, $\phi_2 = -\pi/4$ radian, $\lambda_2 = 325$ nm, and $\gamma_2 = 1060$ nm. The fitting function of Au takes two contributions into account: (i) the Drude's model, and (ii) the interband transition, Lorentz model. Yet the fitting function of Ag given by S. Foteinopoulou et al. [28] has only Drude's model component because there is no interband transition for Ag excited by the incident light in the visible region. Drude fitting function of the dielectric constant of Ag as a function of frequency is expressed as follows

$$\varepsilon(\omega) = \varepsilon_{+} - \frac{\omega_p^2}{\omega(\omega + i\Gamma_D)}, \tag{2.18}$$

where $\varepsilon_{+} = 4.785$, $\omega_p = 14.385 \times 10^{15}$ rad/s, and $\Gamma_D = 7.95 \times 10^{13}$ rad/s.

The different behavior of the dielectric constants of Ag and Au can be obviously seen by considering the ε_2 of these two materials shown in Fig. 2-15(b). ε_2 of the Ag behaves as the free electrons described by the Drude model near infrared region and in the whole visible region because it decreases as lowering wavelength, corresponding to the ε_2 in Drude model. However, The ε_2 of the Ag increases at the wavelength around 368 nm due to the interband transition effect at $\lambda \approx 359$ nm as already mentioned in the section of Lorentz model. As for the Au, ε_2 , it increases with a decreasing wavelength in the visible region due to the effect of the interband transition at $\lambda \approx 470$ nm. The bulk dielectric constants of Ag are valid thin films of thickness, $d \geq 30.4$ nm, the critical thickness. In the case of Au its critical thickness is 25 nm which is smaller than the Ag one. When the thickness is smaller than this critical

point, the dielectric constant has a thickness dependence [27].

2.1.5 Raman spectroscopy quantum phenomena

Raman spectroscopy was briefly described before, but only taking into account the classical point of view in which an incident radiation over a material sample causes an inelastic electronic excitation due to the light interaction with the lattice, namely, interference between the incident light and the mechanical modes of vibration from the material lattice. Nevertheless, this is a very simple and incomplete classical explanation and will not be developed further, since the focus of this study is to understand how does the near field causes an enhancement on the Raman intensity in TERS experiments, and the classical view cannot explain the effect sought [10].

Fermi's Golden Rule

When light interacts with a material sample, the basic start from every Raman related arrangement, the free carriers there contained are going to feel a perturbation and the quantum picture that describes this considers an original and unperturbed Hamiltonian with a new perturbation one [13].

$$H = \frac{1}{m}(-i\hbar\nabla - e\mathbf{A}(t))^2 + V(\mathbf{r}) \tag{2.19}$$

Where m is the free charge carrier mass, $\hbar$ is Planck's constant. $\mathbf{A}$ is the vector potential from which the electric, $\mathbf{E}$, and magnetic, $\mathbf{B}$, components can be extracted, and finally V which is the potential, the gap influence on the carriers and other environmental factors.

Here the quadratic terms in $\mathbf{A}(t)$ will be neglected and by the Coulomb gauge $\nabla \cdot \mathbf{A}(t) = 0$, the perturbation Hamiltonian H_{opt} acting on the electron and causing

its scattering from an occupied band to an occupied band is given by

$$H_{\text{opt}} = \frac{ie\hbar}{m}\mathbf{A}(t)\cdot\nabla \tag{2.20}$$

The above equation is a time dependent perturbing Hamiltonian to an usually conservative system, the solutions for the free charge carriers wavefunctions will be sought.

$$\psi(\mathbf{r},t) = \sum_n a_n(t)u_n(\mathbf{r})e^{-i\frac{E_n t}{\hbar}} \tag{2.21}$$

With the above definition inside Eq.2.19 it is possible to obtain a recursive relation for the wavefunction coefficients.

$$\dot{a}_m(t) = \frac{1}{i\hbar}\sum_n a_n(t)e^{i\omega_{mn}t}\langle m|H(t)|n\rangle, \text{ where} \qquad \langle m|H(t)|n\rangle = \int u_m^*(\mathbf{r})H(t)u_n(\mathbf{r})dr \tag{2.22}$$

In the coefficients $\omega_{mn} = \frac{E_m - E_n}{\hbar}$, is the proportional to states energy difference frequency, also called as Bohr frequency.

As an example only the first order correction for a sinusoidal time dependent perturbation will be considered, $H(t) = H(0)e^{\pm i\omega t}$, by integrating Eq. 2.22, the probability of transition between, m and n states.

$$|a_m^{(1)}(t)|^2 = \frac{|\langle n|H|m\rangle|^2}{\hbar^2}\frac{4\sin^2[(\omega_{mn}\pm\omega)t/2]}{(\omega_{mn}\pm\omega)^2}, \qquad (m\neq n) \tag{2.23}$$

This will give the north of the Raman phenomena as well, since the incident radiation will excite the valence electrons, and these might interact with one or more phonons, by dislocating the crystalline lattice locally, and finally when going back to their fundamental state they will emit light of different wavelength with respect to the incident one.

Fig. 2-16: fig:/fermisgoldenrule.eps

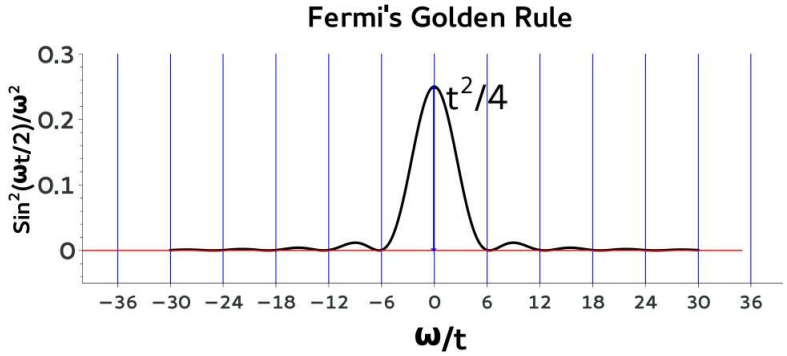

Figure 2-16: Transition probability normalized by the frequency, in function of the frequency

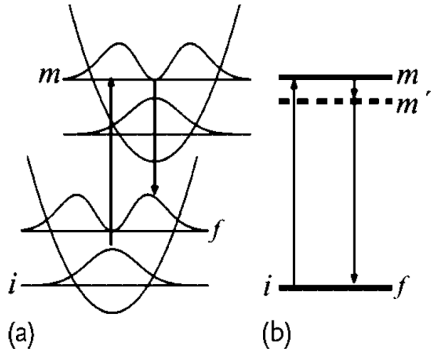

Figure 2-17: (a)Molecular Raman process with the electronic and vibrational levels, it is worth calling attention for the displacement between the two parabolas, this is due to the fact that they correspond to different atomic positions. (b) The excitation and emission process for the Raman changed electron [10]

The Raman intensity

Arises from the excitation of the electrons by the incident photons, which in a molecule change the atomic initial position [10], due to that an overlap between two different vibrational states such as n_q and $n_q + 1$ is possible, as in Fig. 2-17 (a). After the excitation an electron gets a different state, different wavefunction, therefore inducing a new position for the atom, destabilizing it, this causes an atomic vibration.

A general second order Raman event can be described in the following example

Fig. 2-17: fig:/raman2ndorder.eps

As for the case of larger crystalline structures, with several atoms, atomic positions may not be changed by electronic excitations, while second order perturbations will only account for elastic scattering of the photons, as a result the study of third order perturbation is required to get real description of the phenomena. In this case the photo excited electron is going to disturb the atom by generating a new phonon by electron-phonon interaction, and then return to its initial state.

When an electron is excited from an initial state with energy E_i by incident photons to a higher energy state E_m, where $_m$ denotes a real state, when the incident energy excites the electron over the energy gap between the valence and conduction bands, resonance, it gets into a real state, however, it can transfer an amount of energy that does not correspond to a discrete real state, in that case the electron will get into a virtual state, a linear combination of real states. This same electron will interact with a phonon, of energy E_q before returning to the initial state.

All this considered, the Raman intensity considering first order process as a function of the phonon energy, $E_q = \hbar\omega_q$ and of the incident energy, since laser radiation is usually employed, E_{laser}, is given by [10].

$$I(\omega_q, E_{\text{laser}}) = \sum_f \left| \sum_{m,m'} \frac{M_{\text{op}}(\mathbf{k}-\mathbf{q}, im') M^{\text{ep}}(\mathbf{q}, m'm) M_{\text{op}}(\mathbf{k}, im)}{(E_{\text{laser}} - \Delta E_{mi})(E_{\text{laser}} - \hbar\omega_q - \Delta E_{m'i})} \right|^2 \tag{2.24}$$

Where $\mathbf{k}$ is the photon wave vector and $\mathbf{q}$ is the phonon one, i is the initial state, m and $m^{'}$ are two excitation virtual states, f is for the final state. $\Delta E_{m^{(\prime)}i} \equiv (E_{m^{(\prime)}} - E_i) - i\gamma_r$ in which γ_r is the broadening factor for a possible resonant effect, finally M_{op} denotes the electron photon interaction matrix element, while M^{ep} the electron phonon matrix element. In this thesis case the intensity will have M_{op} replaced by $M_{\text{ex-op}}$ which is the exciton optical interaction matrix element and will be explained in detail in the following sections.

Chapter 3

Theoretical methods

Now the focus is turn individually into each component of the tip enhancement Raman effect, starting with the electromagnetic effect, which will be explained in detail, followed by the dipole vector transition in optically excited carbon nanotube, an exciton thorough explanation and to finish with, a new near field dipole vector transition and the basis of a exciton-photon matrix element, the cornerstone to an enhanced Raman intensity.

3.1 Quasi-static approximation

This approximation is based on the concept that to get an initial image of the radiation behavior, it is possible to neglect the time dependency of the incident electromagnetic field, therefore it is as if a picture of the arrangement was taken. When this approximation is applied to the metallic sphere approximation from the nano sphere employed in the TERS experiment, which is much smaller than the wavelength of the incident light used in that experiment its electric field component is constant over the volume of the metallic sphere. Then, the electric field is considered as static, not time dependent, opposing the reality in which it temporally oscillates with $e^{-i\omega t}$ [30]. The scattered electric field $\boldsymbol{E}^{\mathrm{s}}$ outside the metallic sphere and the internal, transferred,

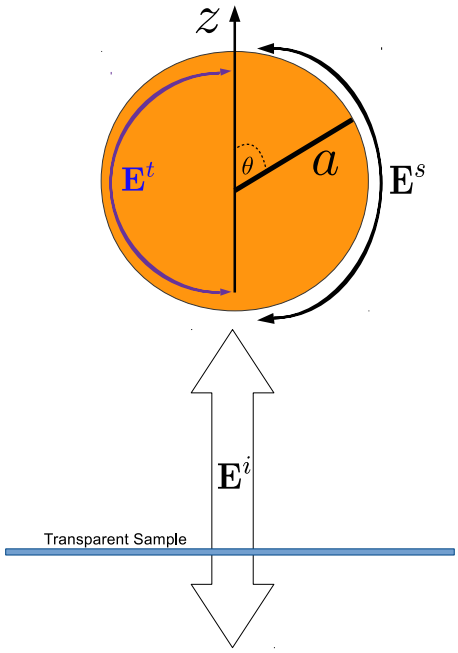

Figure 3-1: **Geometry of the quasi-static approximation.** The incident electric field $\boldsymbol{E}^{\mathrm{i}}$ indicated by the transparent big arrow is constant over the volume of the metallic sphere with radius a. The arrow indicates that $\boldsymbol{E}^{\mathrm{i}}$ is oscillating with time harmonic $e^{-i\omega t}$. The internal electric field $\boldsymbol{E}^{\mathrm{t}}$ is represented by the purple arrow, and the scattered electric field $\boldsymbol{E}^{\mathrm{s}}$ is indicated by the black arrow. The total electric field outside the metallic sphere is the sum of $\boldsymbol{E}^{\mathrm{i}}$ and $\boldsymbol{E}^{\mathrm{s}}$ while the total electric field inside the metallic sphere is $\boldsymbol{E}^{\mathrm{t}}$.

electric field inside the metallic sphere $\boldsymbol{E}^{\mathrm{t}}$ are obtained analysing a scalar potential, φ, using the relation $\boldsymbol{E} = -\nabla\varphi$. This scalar potential inside and outside the metallic sphere is obtained from Laplace's equation, $\nabla^2\varphi = 0$, which, in spherical coordinates,

$$\frac{1}{r^2}\frac{\partial}{\partial r}\left(r^2\frac{\partial\varphi}{\partial r}\right) + \frac{1}{r^2\sin\theta}\frac{\partial}{\partial\theta}\left(\sin\theta\frac{\partial\varphi}{\partial\theta}\right) + \frac{1}{r^2\sin^2\theta}\frac{\partial^2\varphi}{\partial\phi^2} = 0. \tag{3.1}$$

Now, in order to get the full characterization of those three electric field components the separation of variables method is applied to solve Eq. (3.1) by writing the scalar potential as 3 independent functions, each one dependent of a single variable,

Fig. 3-1: fig:/fig:quasi-static-geo3.eps

$\varphi = R(r)P(\theta)Q(\phi)$. Then after Eq. (3.1) has each of its component divided by φ. Based on the simplest case, the ϕ dependent component equation, it is possible to consider it as minus an integer squared, m^2 and from this basic definition, used merely by convenience, the others components will be found.

$$\frac{1}{r^2}\left[2r\frac{\partial R(r)}{\partial r} + r^2\frac{\partial^2 R(r)}{\partial r^2}\right]\frac{1}{R(r)} + \frac{1}{r^2\sin\theta}\left[\cos\theta\frac{\partial P(\theta)}{\partial\theta} + \sin\theta\frac{\partial^2 P(\theta)}{\partial\theta^2}\right]\frac{1}{P(\theta)} + \frac{1}{r^2\sin^2\theta}\frac{\partial^2 Q(\phi)}{\partial\phi^2}\frac{1}{Q(\phi)} = 0 \tag{3.2}$$

From there the isolation of the ϕ component is sought by

$$r^2\sin^2\left\{\frac{1}{r^2}\left[2r\frac{\partial R(r)}{\partial r} + r^2\frac{\partial^2 R(r)}{\partial r^2}\right]\frac{1}{R(r)} + \frac{1}{r^2\sin\theta}\left[\cos\theta\frac{\partial P(\theta)}{\partial\theta} + \sin\theta\frac{\partial^2 P(\theta)}{\partial\theta^2}\right]\frac{1}{P(\theta)}\right\} = -\frac{\partial^2 Q(\phi)}{\partial\phi^2}\frac{1}{Q(\phi)} \tag{3.3}$$

$$\frac{\partial^2 Q(\phi)}{\partial\phi^2} - m^2 Q(\phi) = 0 \tag{3.4}$$

By use of the constant definition it is possible to separate the two remaining components, the same technique is going to be employed, but the θ component is to be isolated and every term is multiplied by r^2.

$$\left[2r\frac{\partial R(r)}{\partial r} + r^2\frac{\partial^2 R(r)}{\partial r^2}\right]\frac{1}{R(r)} = -\frac{1}{\sin\theta}\left[\cos\theta\frac{\partial P(\theta)}{\partial\theta} + \sin\theta\frac{\partial^2 P(\theta)}{\partial\theta^2}\right]\frac{1}{P(\theta)} + \frac{m^2}{\sin^2\theta} \tag{3.5}$$

Finally these two terms may be written as two distinct equations equal to a same integer constant squared l^2, while the ϕ component equation is written for the sake

of completion.

$$\frac{\partial^2 Q(\phi)}{\partial \phi^2} - m^2 Q(\phi) = 0, \tag{3.6}$$

$$2r\frac{\partial R(r)}{\partial r} + r^2\frac{\partial^2 R(r)}{\partial r^2} - l^2 R(r) = 0, \tag{3.7}$$

$$\frac{1}{\sin\theta}\left[\cos\theta\frac{\partial P(\theta)}{\partial \theta} + \sin\theta\frac{\partial^2 P(\theta)}{\partial \theta^2}\right] + \left(l^2 - \frac{m^2}{\sin^2\theta}\right)P(\theta) = 0 \tag{3.8}$$

From these set it is possible to identify 3 corresponding general differential equations that have polynomials combinations as their solution,

For the r component equation, Eq. 3.7, is of the same shape as an Euler equation [31], which has the following solution.

$$R(r) = Ar^n + \frac{B}{r^{n+1}}, \text{ where }, \quad l^2 = -n(n+1) \tag{3.9}$$

Where A and B are coefficients to be defined by applying the boundary conditions later.

As for the case of the θ component equation, Eq.3.8, which is of the same shape as Legendre differential equation [31], that has solution to be.

$$P(\theta) = P_n(x), \text{ where } x = \cos\theta, \quad P_n(x) = \frac{1}{2^n n!}\frac{d^n}{dx^n}(x^2-1)^n \tag{3.10}$$

Finally for the last component remaining, ϕ, Eq. 3.4, which is the simplest polynomial, since this differential equation is of the harmonic shape the solution is

$$Q(\phi) = Ce^{im\phi}, \text{ where } C \text{ is a coefficient to be defined by boundary conditions} \tag{3.11}$$

All this considered, the general solution from Laplace φ is

$$\varphi(r,\theta,\phi) = \sum_{l=0}^{\infty}\sum_{m=0}^{l}\left(a_{lm}r^{l} + \frac{b_{lm}}{r^{l+1}}\right)P_l^m(\cos\theta)e^{im\phi}, \tag{3.12}$$

where $P_l^m(\cos\theta)$ are the associated Legendre polynomials.

The internal potential φ^{t} must be finite at the origin, thus $b_{lm} = 0$ for the potential inside the metallic sphere. In the region outside the metallic sphere, the scattered potential φ^{s} should be zero as it gets to infinity, thus a_{lm} must be zero for the potential outside the metallic sphere. The incident electric field $\boldsymbol{E}^{\mathrm{i}}$ is assumed to be polarized along the z direction, that is, $\boldsymbol{E}^{\mathrm{i}} = E_0\hat{e}_z$, then the potential of the incident electric field is written as $\varphi^{\mathrm{i}} = -E_0 z = -E_0 r P_1(\cos\theta)$. The total potential outside the metallic sphere is the sum between the potentials of the incident light and the scattered field $\varphi^{\mathrm{out}} = \varphi^{\mathrm{i}} + \varphi^{\mathrm{s}}$, and the total potential inside the metallic sphere is the internal potential $\varphi^{\mathrm{in}} = \varphi^{\mathrm{t}}$.

The geometry of the quasi-static approximation is shown in Fig. 3-1. The coefficients a_{lm} of the internal field and b_{lm} of the scattered field are then obtained using the continuity of the tangential component of the electric field and the continuity of the radial component of the electric displacement at the surface of the metallic ball $(r = a)$:

$$\frac{\partial\varphi^{\mathrm{out}}}{\partial\theta}\Big|_{r=a} = \frac{\partial\varphi^{\mathrm{in}}}{\partial\theta}\Big|_{r=a}, \tag{3.13}$$

$$\varepsilon_e\frac{\partial\varphi^{\mathrm{out}}}{\partial r}\Big|_{r=a} = \varepsilon\frac{\varphi^{\mathrm{in}}}{\partial r}\Big|_{r=a}, \tag{3.14}$$

where a is the radius of the metallic sphere, ε_e is the dielectric constant of the environment and ε is the dielectric constant of the metallic spherical approximation to the tip, which depends on the frequency or wavelength of the incident light. The relation between the Legendre polynomial and the associated Legendre ones, $\frac{\mathrm{d}P_n(\cos\theta)}{\mathrm{d}\theta} = -P_l^1(\cos\theta)$ is required for Eq. (3.13). It can be seen that $m = 0$ for the

scattered and internal fields because the incident light is polarized along the z direction, and if the incident light is polarized along the x one, $m = 1$. Then Eq.(3.13) becomes

$$E_0 a P_1^1(\cos\theta) - \sum_{l=1}^{\infty} \frac{b_{l0}}{a^{l+1}} P_l^1(\cos\theta) = -\sum_{l=1}^{\infty} a_{l0} a^l P_l^1(\cos\theta). \tag{3.15}$$

From the orthogonality conditions of the associated Legendre polynomials, the first linear equation of the coefficients is

$$a^l a_{l0} - \frac{1}{a^{l+1}} b_{l0} = -a E_0 \delta_{l1}. \tag{3.16}$$

The second linear equation is obtained from Eq. (3.14) again by the orthogonality of Legendre polynomials,

$$\varepsilon l a^{l-1} a_{l0} + \varepsilon_e \frac{l+1}{a^{l+2}} b_{l0} = -\varepsilon_e E_0 \delta_{l1}. \tag{3.17}$$

After solving Eq. (3.16) and Eq. (3.17), the coefficients a_{l0} and b_{l0} are

$$a_{10} = -\Big(\frac{3\varepsilon_e}{\varepsilon + 2\varepsilon_e}\Big) E_0 \qquad , \qquad b_{10} = \Big(\frac{\varepsilon - \varepsilon_e}{\varepsilon + 2\varepsilon_e}\Big) a^3 E_0, \tag{3.18}$$

$a_{l0} = 0$ and $b_{l0} = 0$ if $l \neq 1$. Therefore, the electric field has only the dipole term which is resonant when $\varepsilon = -2\varepsilon_e$. This resonance condition can be satisfied for the Ag sphere in vacuum, using radiation with wavelength of about 350 nm where the real part from the dielectric function is -2.0 and its imaginary part relatively small as shown in Fig. 2-15. The scattered electric field $\boldsymbol{E}^{\mathrm{s}}$ and the internal one $\boldsymbol{E}^{\mathrm{t}}$ which arose from the gradient of the scattered potential φ^{s} and the internal potential φ^{t}, are then the same as in [30]

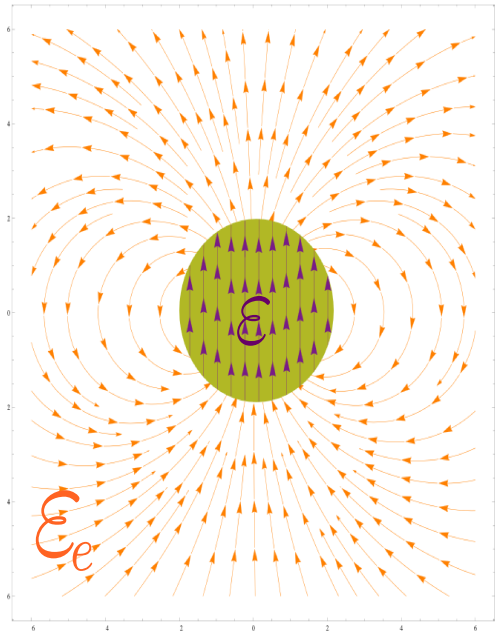

Figure 3-2: **The electric field from the quasi-static approximation.** Outer lines in orange, under the environment dielectric function ε_e and the violet inner lines in the metallic spherical approximation to the tip apex

$$\boldsymbol{E}^{\mathrm{s}} = E_0\Big(\frac{\varepsilon-\varepsilon_e}{\varepsilon+2\varepsilon_e}\Big)\Big(\frac{a}{r}\Big)^3(2\cos\theta\hat{e}_r+\sin\theta\hat{e}_\theta), \tag{3.19}$$

$$\boldsymbol{E}^{\mathrm{t}} = 3E_0\Big(\frac{\varepsilon_e}{\varepsilon+2\varepsilon_e}\Big)\hat{e}_z. \tag{3.20}$$

From this solution of Laplace's equation it is possible to get the electric field outside and inside the spherical approximation of the tip apex depicted in Fig3-2.

For a perfect conductor, the amplitude of the imaginary part of ε is much larger than that of the ε_e, as a result the internal field $\boldsymbol{E}^{\mathrm{t}}$ becomes close to zero . Moreover, the scattered electric field $\boldsymbol{E}^{\mathrm{s}}$ expressed in Eq. (3.19) resembles the incident electric field due to the static dipole moment $p=\varepsilon_e\alpha E_0$ where α is the polarizability, written as $\alpha=4\pi a^3\Big(\frac{\varepsilon-\varepsilon_e}{\varepsilon+2\varepsilon_e}\Big)$, placed at the center of the sphere. The electric field due to the oscillating electric dipole moment will be given in the next section. The main interest

Fig. 3-2: fig:/fig:goldensphere3.eps

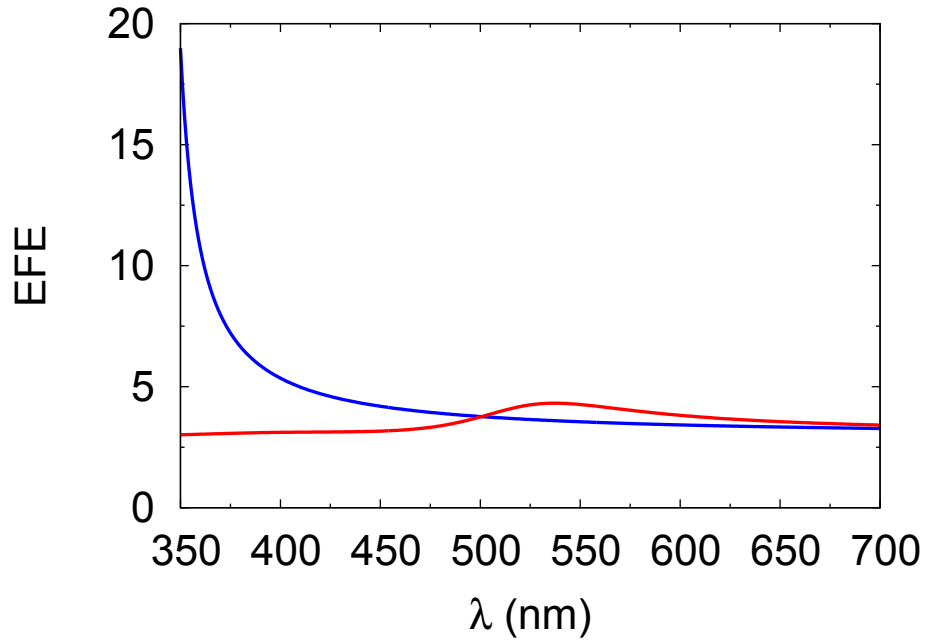

Figure 3-3: **The electric field enhancement EFE of Ag and Au spheres from the quasi-static approximation.** The blue line is the EFE of the small Ag sphere and the red line is the same for a the small Au sphere. The dielectric constants of Ag and Au are obtained from fitting functions [28, 26].

is in the electric field enhancement EFE which is defined as the ratio between the maximum of the total electric field outside the metallic sphere and the amplitude of the incident electric field. The maximum of the total electric field $\boldsymbol{E}^{\text{out}}$ always occurs at the surface of the metallic sphere and on the polarization axis. The scattered electric field at the maximum point is then $E^{\text{s}}_{\text{max}} = 2E_0\left(\frac{\varepsilon-\varepsilon_e}{\varepsilon+2\varepsilon_e}\right)$, and the maximum of the total electric field becomes $E^{\text{out}}_{\text{max}} = E^{\text{s}}_{\text{max}} + E_0 = \left(\frac{3\varepsilon}{\varepsilon+2\varepsilon_e}\right)E_0$. Therefore, the electric field enhancement can be written explicitly as :

$$EFE = 3\left|\frac{\varepsilon}{\varepsilon+2\varepsilon_e}\right|. \tag{3.21}$$

The electric field enhancement EFE depends only on the wavelength of the incident light and the dielectric constant of the environment. It does not depend on

Fig. 3-3: fig:/fig:staticEFE.eps

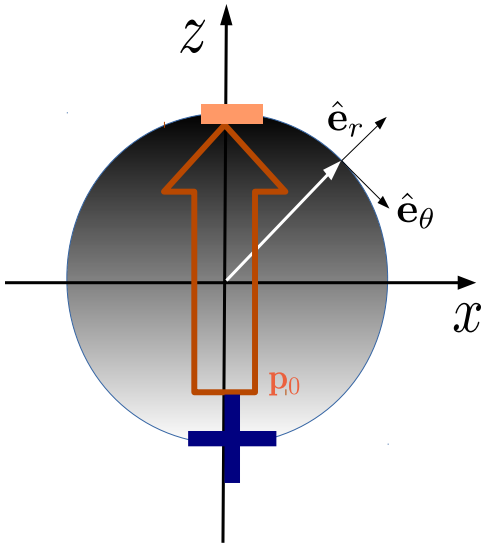

Figure 3-4: The electric dipole moment $\mathbf{p}_0$ polarized along z-axis, $\mathbf{p} = \mathbf{p}_0 e^{-i\omega t}$, where $\hat{e}_z$ is the unit vector in the direction of z. $\hat{e}_r$ and $\hat{e}_\theta$ are unit vectors in the spherical coordinate in the direction of r and θ, respectively. As for the gradient from the gradient between the positive and negative poles, is to represent the charge density distribution, that also oscillates in time

the radius of the metallic sphere, which is not true for large metallic spheres where the transmitted field wavelength suffers a retardation and dispersion effect due to the size of the sphere, [32]. The retardation effect is included in Mie's theory which is fully described later in section 3.3.

Here, the electric field enhancement EFE as a function of wavelength of the small Ag and Au spheres in vacuum is shown in Fig. 3-3. The dielectric constant of Ag and Au are taken from the fitted functions as shown in Fig. 2-15 [28, 26]. High EFE has been found for the small Ag sphere in the region of blue light. The EFE of the small Au sphere in this region is low compared to the Ag. At wavelength 350 nm corresponding to the dielectric constants $\varepsilon_{Ag} = -2.36 + 0.11i$ and $\varepsilon_{Au} = -1.08 + 5.63i$ [28, 26] , the EFE of the small Ag and Au spheres are 19.0 and 3.0, respectively. The high electric field enhancement of the small Ag sphere at the wavelength 350 nm is a result of the dipole resonance.

Fig. 3-4: fig:/fig:dipole2.eps

3.2 Dipole radiation

After the quasi static approximation solution, the dipole vector is further developed, as a pivotal concept to grasp the near field generation phenomena along the tip spherical approximation of the metallic tip apex.

3.2.1 Dipole radiation

Most materials are susceptible to polarization by an electric field. This effect is dependent of the number of electric dipole moments $\boldsymbol{p}$ per unit volume. If the electric field is oscillating with time harmonically, $e^{-i\omega t}$ where ω is angular frequency, the dipoles will oscillate in time at the same frequency as the electric field resulting in the radiation. The electric field of the oscillating dipole $\boldsymbol{p} = \boldsymbol{p}_0 e^{-i\omega t}$ at the distance $\boldsymbol{r}$ from the dipole in the vacuum.

$$\Box\phi = -\frac{\rho(\mathbf{r},t)}{\varepsilon_0} \tag{3.22}$$

$$\Box\mathbf{A} = -\mathbf{J}(\mathbf{r},t)\mu_0 \tag{3.23}$$

$$\text{where Green's function is } g(\mathbf{r},\omega) = \frac{1}{2\pi}\int_{-\infty}^{\infty} g(\mathbf{r},t)e^{i\omega t}dt \tag{3.24}$$

In the above set, $\Box = \nabla^2 - \frac{1}{c^2}\frac{\partial^2}{\partial t^2}$, the so called D'Alambertian, $\mathbf{A}$ is the vector potential, ϕ is the scalar potential, $\rho(\mathbf{r},t)$ is the charge density and finally $\mathbf{J}(\mathbf{r},t)$ is the current density. One of the main difficulties of solving this set of equations is that each component is actually a vector, therefore the need to compute vector operations, to obtain each component.

The dipole vector is obtained solving the wave equations in 3.24 regarding the vector and scalar potentials [33], the solution is laborious and elongated, it may be included in the appendix

$$\boldsymbol{E}(\boldsymbol{r}) = \frac{ck\omega\mu_0}{4\pi}\frac{e^{ikr}}{r}\hat{\boldsymbol{e}}_r \times (\boldsymbol{p}_0 \times \hat{\boldsymbol{e}}_r) + \frac{1}{4\pi\varepsilon_0}\Big(\frac{1}{r^3} - \frac{ik}{r^2}\Big)e^{ikr}[3(\hat{\boldsymbol{e}}_r \cdot \boldsymbol{p}_0)\hat{\boldsymbol{e}}_r - \boldsymbol{p}_0], \quad (3.25)$$

where c is the velocity of light in vacuum, k is wave number of light in vacuum, μ_0 is the permeability of vacuum, ε_0 is the permittivity of vacuum [34]. Here, the dipole is oriented along z-axis, that is, $\boldsymbol{p}_0 = p_0\hat{\boldsymbol{e}}_z$, as shown in Figure (3-4) where the azimuthal symmetry is assumed. Unit vectors $\hat{\boldsymbol{e}}_r$ and $\hat{\boldsymbol{e}}_\theta$ in the spherical coordinates written in terms of $\hat{\boldsymbol{e}}_z$ and $\hat{\boldsymbol{e}}_x$ in parallel and perpendicular directions to the dipole. As $\hat{\boldsymbol{e}}_r = \sin\theta\hat{e}_x + \cos\theta\hat{\boldsymbol{e}}_z$, $\hat{\boldsymbol{e}}_\theta = \cos\theta\hat{\boldsymbol{e}}_x - \sin\theta\hat{\boldsymbol{e}}_z$. Then, the vector product of the first term of Eq. (3.26) becomes $\hat{\boldsymbol{e}}_r \times (\boldsymbol{p}_0 \times \hat{\boldsymbol{e}}_r) = -p_0\sin\theta\hat{\boldsymbol{e}}_\theta$, and the dot product of the second term of Eq. (3.26) becomes $3(\hat{\boldsymbol{e}}_r \cdot \boldsymbol{p}_0)\hat{\boldsymbol{e}}_r - \boldsymbol{p}_0 = 2p_0\cos\theta\hat{\boldsymbol{e}}_r + p_0\sin\theta\hat{\boldsymbol{e}}_\theta$. The electric field is then written in the spherical coordinates

$$\begin{aligned}\boldsymbol{E}(\boldsymbol{r}) &= \frac{1}{2\pi\varepsilon_0}\Big(\frac{1}{r^3} - \frac{ik}{r^2}\Big)(p_0e^{ikr})\cos\theta\hat{\boldsymbol{e}}_r + \\ &\quad \frac{1}{4\pi\varepsilon_0}\Big(\frac{1}{r^3} - \frac{ik}{r^2} - \frac{k^2}{r}\Big)(p_0e^{ikr})\sin\theta\hat{\boldsymbol{e}}_\theta \\ &= E_r\hat{\boldsymbol{e}}_r + E_\theta\hat{\boldsymbol{e}}_\theta \end{aligned} \quad (3.26)$$

p_0e^{ikr} is known as the retarded dipole, and it may be simply written as $[p] = p_0e^{ikr}$. Here, the retarded dipole means that it starts to radiate the electromagnetic wave at time $t - r/c$ where r is the distance between the observer and the radiating dipole. In the near field region ($kr << 1$) (or in the very close region to the electric dipole), the dominant term is proportional to $1/r^3$. The electric field in the near field region $\boldsymbol{E}^{\mathrm{nf}}$ is

$$\boldsymbol{E}^{\mathrm{nf}} = \frac{1}{4\pi\varepsilon_0}\Big(\frac{p_0}{r^3}\Big)(2\cos\theta\hat{\boldsymbol{e}}_r + \sin\theta\hat{\boldsymbol{e}}_\theta). \quad (3.27)$$

Therefore, the scattered electric field $\mathbf{E}^s$ obtained from the quasi-static approximation in Eq. (3.19) is recovered if the electric dipole moment in the vacuum is equal to

Fig. 3-5: fig:/fig:Edipole.eps

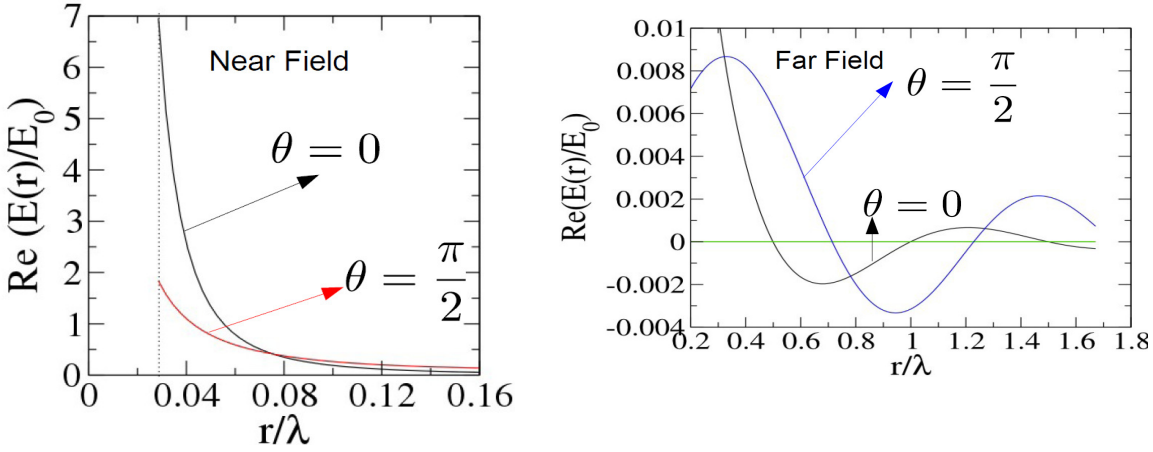

Figure 3-5: **Re$(E(r))/E_0$ as a function of radial distance r:** The dipole electric field $E(r)$ is generated by the electric dipole moment $p_0 = 4\pi\varepsilon_0\left(\frac{\varepsilon-\varepsilon_0}{\varepsilon+2\varepsilon_0}\right)a^3E_0$ where ε and a are the dielectric constant and radius of the metallic sphere. a is 10 nm. The wavelength of the incident light is 350 nm, and the corresponding bulk dielectric constant of the Ag is $\varepsilon_{\text{Ag}} = -2.36 + 0.11i$ [28]. (a) Re$(E(r))/E_0$ as a function of r when $\theta = 0$, the red curve and $\theta = \pi/2$ represented by the blue curve in the near field region $r \ll 0.16\lambda$. The dashed black line denote $r = 10$ nm corresponding to the radius of the Ag sphere. (b) Re$(E(r))/E_0$ as a function of r when $\theta = 0$ represented by the red curve and $\theta = \pi/2$ represented by the blue curve in the far field region $r \gg 0.16\lambda$.

$p_0 = 4\pi\varepsilon_0\left(\frac{\varepsilon-\varepsilon_0}{\varepsilon+2\varepsilon_0}\right)a^3E_0$.

In Fig. 3-5, Re$(E(r))/E_0$ was plotted as a function of r for $\theta = 0$ and $\theta = \pi/2$, where $E(r)$ is the dipole electric field as expressed in Eq. (3.26). The electric dipole moment $p_0 = 4\pi\varepsilon_0\left(\frac{\varepsilon-\varepsilon_0}{\varepsilon+2\varepsilon_0}\right)a^3E_0$ is in the small Ag sphere with radius a and the dielectric constant ε_{Ag}. The radius a is defined as 10 nm. The wavelength of the incident light is 350 nm, and the dielectric constant of Ag at this wavelength is approximated to be $\varepsilon_{\text{Ag}} = -2.36 + 0.11i$ [28] which corresponds to the bulk dielectric

constant of Ag. The near field region was divided by the radial distance where $kr \ll 1$ or $r \ll 0.16\lambda$ is satisfied and the far field region where $kr \gg 1$ or $r \gg 0.16\lambda$ is satisfied. Firstly, in both two regions, there is only the radial part of the electric field $E_r(r)$ along the line $\theta = 0$ which is parallel to the polarization axis, and there is only the polar part of the electric field $E_\theta(r)$ along the line $\theta = \pi/2$ which is perpendicular to the polarization axis, as seen in Eq. (3.26) and Fig. 3-4. In the near field region, shown in Fig. 3-5, the electric field strongly decays by increasing r due to a $1/r^3$ dependence. The maximum of the dipole electric field is about twice that of the incident electric field which occurs at the surface of the Ag sphere with $\theta = 0$. As for the far field region, also in Fig. 3-5, the amplitude of the dipole electric field is very small compared to the amplitude of the incident electric field. The dominant term of the dipole electric field in this region is proportional to $1/r$ which only appears in the polar part of the dipole electric field, E_θ. E_r of the dipole electric field is very small compared to E_θ in the far field region. Therefore, the dipole electric field in the far field region is an outgoing wave which travels out from the source carrying energy with only a polar component.

3.3 Mie's Spherical Light Scattering Theory

A metal is an absorbing material since its dielectric constant has an imaginary part. When under an external light , such as laser, incident on a metallic sphere, then the electric current flows resulting in the absorption of the electromagnetic field. The electromagnetic field inside the metallic sphere is called the internal field. Furthermore, the oscillation of charges and current in the metallic sphere radiates a secondary electromagnetic field, the scattered wave outward. The space may be divided into two regions: (i) outside the metallic sphere and (ii) inside the metallic sphere. It is assumed that the metallic sphere is within a non-absorbing dielectric with dielectric constant ε where the incident light and the scattered wave are traveling. Firstly, the

solutions of the scattered wave traveling outward from the metallic sphere will be sought and after that, the solutions of the internal fields can be solved by a similar fashion. To conclude with, the coefficients of the scattered wave and the internal field are calculated using the boundary conditions.

Hereafter, the time-harmonic dependence of the electric and magnetic fields is assumed to be $e^{-i\omega t}$ where ω is the angular frequency of the incident light.

3.3.1 Solution of the scattered wave

Maxwell's equations for the electromagnetic wave traveling in the non-absorbing dielectric

$$\nabla \cdot \boldsymbol{E} = 0, \tag{3.28}$$

$$\nabla \cdot \boldsymbol{B} = 0, \tag{3.29}$$

$$\nabla \times \boldsymbol{E} = i\omega \boldsymbol{B}, \tag{3.30}$$

$$\nabla \times \boldsymbol{B} = -i\varepsilon \frac{k_0}{c} \boldsymbol{E}, \tag{3.31}$$

where $\boldsymbol{E}$ is the electric field, $\boldsymbol{B}$ is the magnetic field, k_0 is the vacuum wavenumber and c is velocity of light in vacuum. The wave equations of $\boldsymbol{E}$ and $\boldsymbol{B}$ are obtained by taking the rotation, $\nabla\times$, from Eq. (3.30) and Eq. (3.31). By the vector identity, $\nabla \times \nabla \times \boldsymbol{E} = \nabla(\nabla \cdot \boldsymbol{E}) - \nabla^2 \boldsymbol{E}$ and Gauss's laws, the wave equations are

$$(\nabla^2 + k^2)\boldsymbol{E} = 0 \quad , \quad (\nabla^2 + k^2)\boldsymbol{B} = 0 \tag{3.32}$$

where $k = \sqrt{\varepsilon} k_0$ is the wavenumber of the incident light and the scattered wave in the dielectric medium. Eq. (3.32) are known as the vector Helmholtz equations. Each component (r, θ, ϕ) of the vector Laplacian's $\nabla^2 \boldsymbol{E}$ in spherical coordinates are given in Appendix (A.1.2). Only the radial components of the electric (magnetic) field $E_r(B_r)$ are separable from the other components. Therefore, $E_r(B_r)$ can be solved directly

from the vector Helmholtz equations. In order to solve for the other components of the electric (E_θ, E_ϕ) and those of the magnetic fields (B_θ, B_ϕ), the general solutions of the electromagnetic field are split into two modes, (i) the transverse magnetic mode or TM mode and the (ii) transverse electric mode or TE mode. As indicated by their names, TM mode has no radial component of the magnetic field or $B_r = 0$, yet $E_r \neq 0$, and TE mode has no radial component of the electric field or $E_r = 0$, yet $B_r \neq 0$. TM mode corresponds to the electric vibration where as the TE mode is related to the magnetic vibration in the metallic sphere. Importantly, the general solution of the electromagnetic wave is the sum of TM and TE modes.

TM mode of the scattered fields

Remembering that in this mode $B_r = 0$, initially E_r will be sought in the TM mode. The differential equation of E_r in spherical coordinates is given by

$$\frac{1}{r^2}\frac{\partial}{\partial r}\left(r^2\frac{\partial E_r}{\partial r}\right) + \frac{1}{r^2\sin\theta}\frac{\partial}{\partial\theta}\left(\sin\theta\frac{\partial E_r}{\partial\theta}\right) + \frac{1}{r^2\sin^2\theta}\frac{\partial^2 E_r}{\partial\phi^2} + k^2 E_r = 0. \tag{3.33}$$

The separation of variables technique that was employed to solve Laplace's equation in section 3.1, is employed one more time to solve Eq. (3.33), yet there is a difference, since in this case k^2E_r is a term that makes this partial differential equation inhomogeneous , by writing E_r as $E_r = \frac{R(r)}{r}P(\theta)Q(\phi)$ and using this definition into Eq. (3.33), the three ordinarily differential equations of each function, $R(r), P(\theta)$ and $Q(\phi)$ are

$$\frac{\partial^2}{\partial r^2}(rR(r)) + \left[k^2 - \frac{l(l+1)}{r^2}\right](rR(r)) = 0, \tag{3.34}$$

$$\frac{1}{\sin\theta}\frac{\partial}{\partial\theta}\left(\sin\theta\frac{\partial P(\theta)}{\partial\theta}\right) + \left[l(l+1) - \frac{m^2}{\sin^2\theta}\right]P(\theta) = 0, \tag{3.35}$$

$$\frac{\partial^2 Q(\phi)}{\partial\phi^2} + m^2 Q(\phi) = 0. \tag{3.36}$$

It is valid to point out that differently than Laplace's equation separation of variables, in the E_r case the inhomogeneous term may be carried along a single component, r in this case. The solution of the azimuthal part $Q(\phi)$ could be either $\sin(m\phi)$ or $\cos(m\phi)$, where m are integers. Then we may write $Q(\phi)$ as a linear combination of these two solutions

$$Q(\phi) = A\cos(m\phi) + B\sin(m\phi) \qquad m = 0, \pm1, \pm2, \pm3, \ldots . \tag{3.37}$$

The solutions of Eq. (3.35) for a given m are the associated Lengendre polynomials, $P_l^m(\cos\theta)$, where $l = 0, 1, 2, 3, \ldots$. Legendre's polynomials properties are discussed in the Appendix (A.3). For the radial part, the Eq. (3.34) which is the spherical Bessel function are used. As for Eq. (3.34) the spherical Hankel functions of the first kind, $h_l^{(1)}$

$$R(r) = h_l^{(1)}(kr), \tag{3.38}$$

which behaves asymptotically from the outgoing wave, $h_l^{(1)}$ can be approximated as $h_l^{(1)}(kr) \approx (-1)^{l+1}\frac{e^{ikr}}{kr}$.

As for the complete solution for E_r, it can be expressed as a linear combination of all l and m. Here it is possible to see the scattering coefficient a_{lm}, that is part of the main difference between the near field and far field interactions with excitons

$$E_r(r, \theta, \phi) = \sum_{l,m} a_{lm} \frac{h_l^{(1)}(kr)}{r} P_l^m(\cos\theta) Q_m(\phi). \tag{3.39}$$

The remaining components of the electric and magnetic fields in TM mode are extracted by going back to Maxwell's equations while focusing on each direction components in the LHS and the RHS of Eq. (3.30) and Eq. (3.31) so that a six equations system arises. The differential equation of each remaining component then, is written in terms of the already obtained E_r by a normal elimination method found

in the Appendix ($A.2$). These differential equations for E_θ, E_ϕ, B_θ and B_ϕ are

$$\frac{\partial^2}{\partial r^2}(rE_\theta) + k^2(rE_\theta) = \frac{\partial^2 E_r}{\partial r \partial \theta}, \tag{3.40}$$

$$\frac{\partial^2}{\partial r^2}(rE_\phi) + k^2(rE_\phi) = \frac{1}{\sin\theta}\frac{\partial^2 E_r}{\partial r \partial \phi}, \tag{3.41}$$

$$\frac{\partial^2}{\partial r^2}(rB_\theta) + k^2(rB_\theta) = -\frac{i\varepsilon k_0}{c}\frac{1}{\sin\theta}\frac{\partial E_r}{\partial \phi}, \tag{3.42}$$

$$\frac{\partial^2}{\partial r^2}(rB_\phi) + k^2(rB_\phi) = \frac{i\varepsilon k_0}{c}\frac{\partial E_r}{\partial \theta}. \tag{3.43}$$

The Eqs. (3.40)-(3.43) have the same form as LHS but different from RHS. Next, the solution of E_θ for each l and m will be shown as an example since for the other components the same process was conducted.

The solution of E_θ in TM mode is obtained by substituting the E_r for each l and m from Eq. (3.33) into Eq. (3.40),

$$\frac{\partial^2}{\partial r^2}(rE_\theta) + k^2(rE_\theta) = a_{lm}\frac{\partial}{\partial r}\left[\frac{h_l^{(1)}(kr)}{r}\right]\frac{\partial P_l^m(\cos\theta)}{\partial \theta}Q_m(\phi). \tag{3.44}$$

Eq. (3.44) shows that E_θ has its angular part corresponding to $\frac{\mathrm{d}P_l^m(\cos\theta)}{\mathrm{d}\theta}Q_m(\phi)$, and the radial part in terms of $h_l^{(1)}(kr)$. This means that the same polynomials used previously apply, with different coefficients nonetheless. Thus it can be assumed that $E_\theta = \frac{1}{r}\frac{\partial}{\partial r}[rK_l(r)]\frac{\mathrm{d}P_l^m(\cos\theta)}{\mathrm{d}\theta}Q_m(\phi)$ where $K_l(r)$ is a radial function to be determined. By substituting this assumed solution of E_θ into Eq. (3.44) and employing the linearly independent property of $P_l^m(\cos\theta)$, the differential equation of $K_l(r)$ should be

$$\frac{\partial^2}{\partial r^2}[rK_l(r)] + rK_l(r) = a_{lm}\frac{h_l^{(1)}(kr)}{r} \tag{3.45}$$

Since $h_l^{(1)}(kr)$ is in Eq. (3.34), the $\frac{h_l^{(1)}(kr)}{r}$ satisfies

$$\frac{h_l^{(1)}(kr)}{r} = \frac{1}{l(l+1)}\frac{\partial^2}{\partial r^2}[rh_l^{(1)}(kr)] + \frac{k^2}{l(l+1)}rh_l^{(1)}(kr) \tag{3.46}$$

By substituting Eq. (3.46) into Eq. (3.45) and comparing the equation's both sides, the solution of $K_l(r)$ may be

$$rK_l(r) = \frac{a_{lm}}{l(l+1)} rh_l^{(1)}(kr) \tag{3.47}$$

The solution of E_θ is written as a linear combination of all l and m :

$$E_\theta = \sum_{l,m} \frac{a_{lm}}{l(l+1)} \frac{1}{r} \frac{\mathrm{d}}{\mathrm{d}r} \Big[rh_l^{(1)}(kr) \Big] \frac{\mathrm{d}P_l^m(\cos\theta)}{\mathrm{d}\theta} Q_m(\phi) \ , \ (l = 0, 1, 2, ..., |m| \leq l). \tag{3.48}$$

For simplification a new radial function, namely, $\zeta_l(kr)$ is defined as $\zeta_l(kr) = krh_l^{(1)}(kr)$, and $\zeta_l^{'}(kr)$ is its own derivative. Finally, the solution of E_θ becomes

$$E_\theta = \sum_{l,m} \frac{a_{lm}}{l(l+1)} \frac{\zeta_l^{'}(kr)}{r} \frac{\mathrm{d}P_l^m(\cos\theta)}{\mathrm{d}\theta} Q_m(\phi). \tag{3.49}$$

The solutions of E_ϕ , B_θ and B_ϕ in TM mode are obtained in the same fashion as in E_θ, solving Eq. (3.41), Eq. (3.42) and Eq. (3.43). These solutions are

$$E_\phi = \sum_{l,m} \frac{a_{lm}}{l(l+1)} \frac{\zeta_l^{'}(kr)}{r} \frac{P_l^m(\cos\theta)}{\sin\theta} \frac{\mathrm{d}Q_m(\phi)}{\mathrm{d}\phi}, \tag{3.50}$$

$$B_\theta = -\frac{ik^2}{\omega} \sum_{l,m} \frac{a_{lm}}{l(l+1)} h_l^{(1)}(kr) \frac{P_l^m(\cos\theta)}{\sin\theta} \frac{\mathrm{d}Q_m(\phi)}{\mathrm{d}\phi}, \tag{3.51}$$

$$B_\phi = \frac{ik^2}{\omega} \sum_{l,m} \frac{a_{lm}}{l(l+1)} h_l^{(1)}(kr) \frac{\mathrm{d}P_l^m(\cos\theta)}{\mathrm{d}\theta} Q_m(\phi). \tag{3.52}$$

TE mode of the scattered field's components

The electric and magnetic field in TE mode in the region outside the metallic sphere are obtained in the similar way as TM mode by starting from the derivation of the radial part of the magnetic field B_r, since in this mode $E_r = 0$. The remaining components of the magnetic field, B_θ and B_ϕ, and the electric field are obtained by solving the differential equations which are written in terms of the B_r previously

obtained. The differential equation of B_r comes from the vector Helmholtz equation, in Eq. (3.32), thus it is of the same form as the E_r in Eq. (3.33). B_r must also behave as an outgoing wave asymptotically as demanded by the boundary conditions for the radiation wave. Therefore, the solution of B_r has the same angular and radial components as E_r, yet the amplitude differs. Here, B_r's amplitude in TE mode for each l as b_{lm}. Then, B_r is expressed as

$$B_r(r,\theta,\phi) = \sum_{l,m} b_{lm} \frac{h_l^{(1)}(kr)}{r} P_l^m(\cos\theta) Q_m(\phi). \tag{3.53}$$

Next, the differential equations of B_θ, B_ϕ, E_θ and E_ϕ written in term of B_r are sought by the simple elimination method of a six equations system from Eq. (3.30) and Eq. (3.31) using the linearly independence property of the unit vectors in spherical coordinates. The differential equation of B_θ in TE mode has exactly the same form as that of E_θ in the TM mode, and the differential equation of B_ϕ in TE mode is the same as E_ϕ again in the TM mode. Therefore, the solutions from B_θ and B_ϕ in TE mode are of the same shape as in Eq. (3.49) and Eq. (3.52), but with the amplitude b_{lm}

$$B_\theta = \sum_{l,m} \frac{b_{lm}}{l(l+1)} \frac{\zeta_l'(kr)}{r} \frac{\mathrm{d}P_l^m(\cos\theta)}{\mathrm{d}\theta} Q_m(\phi), \tag{3.54}$$

$$B_\phi = \sum_{l,m} \frac{b_{lm}}{l(l+1)} \frac{\zeta_l'(kr)}{r} \frac{P_l^m(\cos\theta)}{\sin\theta} \frac{\mathrm{d}Q_m(\phi)}{\mathrm{d}\phi}. \tag{3.55}$$

Nevertheless, the RHS of the differential equations from E_θ and E_ϕ in TE mode are different in comparison with those of B_θ and B_ϕ in TM mode. To obtain these two solutions in TE mode, which are the same as those of E_θ in TM mode, their solution is shown as an example, the process is: (1) substituting the solution of B_r in Eq. (3.53), to the differential equations, for the components E_θ and E_ϕ, (2) writing E_θ and E_ϕ as separable equations with the same angular part but different radial part as the RHS of the differential equations, (3) recalling the linearly independence of $P_l^m(\cos\theta)$ and

the spherical Bessel equation and finally (4) comparing two sides of the equations to determine the radial part. By following these steps, the solutions of E_θ and E_ϕ in TE mode mode is

$$E_\theta = i\omega \sum_{l,m} \frac{b_{lm}}{l(l+1)} h_l^{(1)}(kr) \frac{P_l^m(\cos\theta)}{\sin\theta} \frac{\mathrm{d}Q_m(\phi)}{\mathrm{d}\phi}, \tag{3.56}$$

$$E_\phi = -i\omega \sum_{l,m} \frac{b_{lm}}{l(l+1)} h_l^{(1)}(kr) \frac{\mathrm{d}P_l^m(\cos\theta)}{\mathrm{d}\theta} Q_m(\phi). \tag{3.57}$$

All this considered, the general solutions of the electric and magnetic field which are the sum of TM and TE modes in the region outside the metallic sphere were obtained. Yet the coefficients $a_l m$ and $b_l m$ which are defined as the coefficients of TM and TE modes have not been discovered yet. The boundary conditions at the surface of the metallic sphere must be used to find them. Therefore, the electromagnetic field inside the metallic sphere called the internal field at the surface is needed to satisfy the previously state boundary conditions. The solution of the internal field is explained in the next section.

3.3.2 Solution of the internal field

The first three equations from Maxwell's set inside the metallic sphere are the same as Eqs. (3.28)-(3.30). Yet the Ampere and Maxwell's law must include the current density $\boldsymbol{J}$ flowing inside the metallic sphere. Thus, the fourth equation from Maxwell's set must be rewritten to

$$\nabla \times \boldsymbol{B} = \mu_0 \boldsymbol{J} - i\varepsilon \frac{k_0}{c} \boldsymbol{E}, \tag{3.58}$$

where μ_0 is the permeability of free space, ε is the dielectric constant, k_0 is wavenumber in free space and c is the speed of light in free space. The metallic sphere is assumed to be an Ohmic material, in which, $\boldsymbol{J} = \sigma \boldsymbol{E}$ where σ is the conductivity. Therefore, the two terms from the RHS of Eq. (3.58) can be grouped. Then, Eq. (3.58)

becomes

$$\nabla \times \boldsymbol{B} = -\frac{ik_0}{c}\left(\varepsilon + \frac{i\sigma}{\varepsilon_0 \omega}\right)\boldsymbol{E}. \tag{3.59}$$

The term $\varepsilon + \frac{i\sigma}{\varepsilon_0\omega}$ will be replaced by the dielectric constant $\tilde{\varepsilon}$ [24], to put Eq. (3.59) in the same form as Eq. (3.31). This approach is commonly found in solid state physics and is known as optical conductivity. The metallic sphere becomes dispersive due to the complex dielectric component ε_2 in $\tilde{\varepsilon}$. Finally, Ampere's and Maxwell's laws of the internal field are now

$$\nabla \times \boldsymbol{B} = -\frac{ik_0}{c}\tilde{\varepsilon}\boldsymbol{E}. \tag{3.60}$$

From Eq. (3.28)-Eq. (3.30) and Eq. (3.60), the vector Helmholtz equations of the electric and magnetic fields can be obtained, and the complex wavenumber $\tilde{k}$ is defined as $\tilde{k} = k_0\sqrt{\varepsilon}$ [24], then

$$(\nabla^2 + \tilde{k}^2)\boldsymbol{E} = 0 \quad , \quad (\nabla^2 + \tilde{k}^2)\boldsymbol{B} = 0. \tag{3.61}$$

As expected the vector equations for the internal field are of the same form as the scattered wave. The difference between Eq. (3.32) and Eq. (3.61) is only the wavenumber. The solution of the internal field is divided into TM mode in which $E_r \neq 0$ but $B_r = 0$, and TE mode in which $B_r \neq 0$ but $E_r = 0$, as it was done for the scattered wave. The general solution of the internal field is the sum of these two modes.

TM mode of the internal field's components

In TM mode ($E_r \neq 0, B_r = 0$), firstly the solution of the radial part of the electric field E_r is sought, as for the remaining components of the electric field and other the ones from the magnetic field which can be derived from E_r. The differential equation of the internal E_r is of the same form as Eq. (3.33) except for the wavenumber which becomes complex for the internal field. Using the separation of variables method one more time will imply in a function that has an angular part as a product of the associated Legendre polynomial $P_l^m(\cos\theta)$ and $Q_m(\phi)$, expressed in Eq. (3.37). The

solution of the radial function $R(r)$ is obtained from the spherical Bessel function

$$\frac{\mathrm{d}^2}{\mathrm{d}r^2}(rR(r)) + [\tilde{k}^2 - \frac{l(l+1)}{r^2}](rR(r)) = 0. \tag{3.62}$$

The internal field's boundary condition is that it must be finite at the center of the metallic sphere which is defined as the origin of the system. Thus, only the spherical Bessel function $j_l(\tilde{k}r)$ satisfies it, this is due to the approximation from $j_l(\tilde{k}r)$ since $j_l(\tilde{k}r) \approx \frac{(\tilde{k}r)^l}{1\cdot3\cdot5\cdots(2l+1)}$ which is finite at the origin. Therefore, the solution of E_r of the internal field in TM mode and its coefficient d_{lm} are defined

$$E_r(r,\theta,\phi) = \sum_{l,m} d_{lm}\frac{j_l(\tilde{k}r)}{r}P_l^m(\cos\theta)Q_m(\phi). \tag{3.63}$$

It can be seen that the differences between E_r of the scattered wave in Eq. (3.39) and E_r of the internal one in Eq. (3.63) are between their coefficients. Therefore, the remaining components of the electric field, E_θ and E_ϕ, and the magnetic field, B_θ and B_ϕ, of the internal field are obtained by replacing the complex coefficient a_{lm} of the scattered wave by d_{lm}, and the spherical Hankel function $h_l^{(1)}(kr)$ of the scattered wave by the spherical Bessel function $j_l(\tilde{k}r)$, as the differential equations of the remaining components of the internal field are the same as those of the scattered wave. A new radial function, $\psi_l(\tilde{k}r) = krj_l(\tilde{k}r)$ is defined to simplify the cumbersome accumulation of different functions, and $\psi_l'(\tilde{k}r)$ is its own derivative. Therefore, these

remaining solutions of the internal electric and magnetic field are

$$E_\theta = \sum_{l,m} \frac{d_{lm}}{l(l+1)} \frac{\psi_l{}'(\tilde{k}r)}{r} \frac{\partial P_l^m(\cos\theta)}{\partial\theta} Q_m(\phi), \tag{3.64}$$

$$E_\phi = \sum_{l,m} \frac{d_{lm}}{l(l+1)} \frac{\psi_l{}'(\tilde{k}r)}{r} \frac{P_l^m(\cos\theta)}{\sin\theta} \frac{\partial Q_m(\phi)}{\partial\phi}, \tag{3.65}$$

$$B_\theta = -\frac{i\tilde{k}^2}{\omega} \sum_{l,m} \frac{d_{lm}}{l(l+1)} j_l(\tilde{k}r) \frac{P_l^m(\cos\theta)}{\sin\theta} \frac{\partial Q_m(\phi)}{\partial\phi}, \tag{3.66}$$

$$B_\phi = \frac{i\tilde{k}^2}{\omega} \sum_{l,m} \frac{d_{lm}}{l(l+1)} j_l^(\tilde{k}r) \frac{\partial P_l^m(\cos\theta)}{\partial\theta} Q_m(\phi). \tag{3.67}$$

In order to obtain the coefficients discussed before this equation set will be further studied when handling all of the components from both inside and outside fields to obtain the coefficients values.

TE mode of the internal field's components

In TE mode ($B_r \neq 0, E_r = 0$), firstly the solution of the radial part of the internal magnetic field B_r is investigated and then, from this solution, the remaining components of the internal magnetic field and also the electric field are developed. The differential equation of the internal B_r is in the same form as that of the internal E_r in TM mode. Therefore, the solution of the internal B_r has the same radial and angular forms as the internal E_r but with different coefficients. And the corresponding coefficient of the internal field in TE mode is c_{lm}. Thus, the solution of internal B_r is

$$B_r(r,\theta,\phi) = \sum_{l,m} c_{lm} \frac{j_l(\tilde{k}r)}{r} P_l^m(\cos\theta) Q_m(\phi). \tag{3.68}$$

The remaining components of the internal magnetic field and the internal electric field in TE mode are obtained by replacing the coefficient b_{lm}, $h_l^{(1)}(kr)$, $\zeta_l(kr)$ and

$\zeta_l^{'}(kr)$ of the scattered wave in TE mode by c_{lm}, $j_l(\tilde{k}r)$, $\psi_l(\tilde{k}r)$ and $\psi_l^{'}(\tilde{k}r)$. Then,

$$B_\theta = \sum_{l,m} \frac{c_{lm}}{l(l+1)} \frac{\psi_l^{'}(\tilde{k}r)}{r} \frac{\partial P_l^m(\cos\theta)}{\partial\theta} Q_m(\phi), \tag{3.69}$$

$$B_\phi = \sum_{l,m} \frac{c_{lm}}{l(l+1)} \frac{\psi_l^{'}(\tilde{k}r)}{r} \frac{P_l^m(\cos\theta)}{\sin\theta} \frac{\partial Q_m(\phi)}{\partial\phi}, \tag{3.70}$$

$$E_\theta = i\omega \sum_{l,m} \frac{c_{lm}}{l(l+1)} j_l(\tilde{k}r) \frac{P_l^m(\cos\theta)}{\sin\theta} \frac{\partial Q_m(\phi)}{\partial\phi}, \tag{3.71}$$

$$E_\phi = -i\omega \sum_{l,m} \frac{c_{lm}}{l(l+1)} j_l(\tilde{k}r) \frac{\partial P_l^m(\cos\theta)}{\partial\theta} Q_m(\phi). \tag{3.72}$$

Following up, all defined coefficients will be calculated using the boundary conditions of the electromagnetic field at the surface of the metallic sphere.

3.3.3 Coefficients of the scattered and internal field's components

In this section, the coefficients of the scattered wave and the internal field are finally extracted from the boundary conditions for the electric and magnetic field's components at the surface of the metallic sphere.

Expansion by plane wave incident light

In spectroscopy measurement, laser light is often utilized as an excitation source. The incident light will be considered to be a laser source, propagating as a plane wave. The direction of propagation is z, and the incident electric field is polarized in the x direction. Thus, the electric and magnetic fields propagating in the non-absorbing dielectric, ε

$$\boldsymbol{E}^{\mathrm{i}} = E_0 \hat{\boldsymbol{e}}_x e^{ikz} \quad , \quad \boldsymbol{B}^{\mathrm{i}} = \frac{k}{\omega} E_0 \hat{\boldsymbol{e}}_y e^{ikz}, \tag{3.73}$$

where k is the wavenumber of the incident light in the dielectric environment, ω is the angular frequency of the incident light, and E_0 is the amplitude of the incident

electric field which is related to the intensity of the incident light I as $E_0 = \sqrt{\frac{I}{\varepsilon_0 c}}$, where ε_0 is the permittivity of the free space and c is the velocity of light in free space. $\boldsymbol{E}^{\mathrm{i}}$ and $\boldsymbol{B}^{\mathrm{i}}$ can be expanded in term of spherical waves. The concept of TM mode and TE mode is also applied to the incident light as it is applied to the scattered wave in the region outside of the metallic sphere. As a result, once E_r^{i} has been expanded, the remaining components of the electric and magnetic fields are obtained simply by comparing the E_r^{i} with E_r^{s} for the scattered wave in both TM and TE modes.

By considering the E_r^{i} expansion. E_r^{i} can be considered for TM mode in the spherical coordinates

$$E_r^{\mathrm{i}} = E_0 \sin\theta \cos\phi e^{ikr\cos\theta} = -\frac{E_0}{ikr}\cos\phi \frac{\partial}{\partial\theta}\Big(e^{ikr\cos\theta}\Big). \tag{3.74}$$

The azimuthal component has only one term correspondent to $m = 1$, the cosine function, since $Q_1(\phi) = \cos\phi + \sin\phi$, but the sine will be disconsidered. The exponential term can be expanded in term of the spherical Bessel function $j_l(kr)$ and the Legendre polynomial $P_l(\cos\theta)$ as

$$e^{ikr\cos\theta} = \sum_l (2l+1) i^l j_l(kr) P_l(\cos\theta). \tag{3.75}$$

By substituting Eq. (3.75) into Eq. (3.74) provided with the relation between Legendre polynomials the associated Legendre polynomials, $(-1)^m \frac{\mathrm{d}^m P_l}{\mathrm{d}\theta^m} = P_l^m(\cos\theta)$, expanding E_r^{i}

$$E_r^{\mathrm{i}} = E_0 \sum_l (2l+1) i^{l-1} \frac{j_l(kr)}{kr} P_l^m(\cos\theta)\cos\phi. \tag{3.76}$$

Comparing Eq. (3.76) with Eq. (3.39), the remaining components of the electric and magnetic fields in TM mode can be calculated from those of the scattered wave in TM mode, if the coefficients a_{lm} are replaced by $E_0(2l+1)i^{l-1}$ for the initial wave, the same with the spherical Hankel function of the first kind $h_l^{(1)}(kr)/r$ by the spherical

Bessel function $j_l(kr)/kr$, and also $Q_m(\phi)$ by $\cos\phi$. Implying

$$E_\theta^{\mathrm{i}} = E_0 \sum_l \frac{(2l+1)i^{l-1}}{l(l+1)} \frac{\psi_l'(kr)}{kr} \frac{\mathrm{d}P_l^1(\cos\theta)}{\mathrm{d}\theta} \cos\phi, \tag{3.77}$$

$$E_\phi^{\mathrm{i}} = -E_0 \sum_l \frac{(2l+1)i^{l-1}}{l(l+1)} \frac{\psi_l'(kr)}{kr} \frac{P_l^1(\cos\theta)}{\sin\theta} \sin\phi, \tag{3.78}$$

$$B_\theta^{\mathrm{i}} = E_0 \frac{k}{\omega} \sum_l \frac{(2l+1)i^{l}}{l(l+1)} j_l(kr) \frac{P_l^1(\cos\theta)}{\sin\theta} \sin\phi, \tag{3.79}$$

$$B_\phi^{\mathrm{i}} = E_0 \frac{k}{\omega} \sum_l \frac{(2l+1)i^{l}}{l(l+1)} j_l(kr) \frac{\mathrm{d}P_l^1(\cos\theta)}{\mathrm{d}\theta} \cos\phi. \tag{3.80}$$

where a is the radius of the metallic sphere.

Next, the expansion of the incident light in TE mode ($B_r^{\mathrm{i}} \neq 0, E_r^{\mathrm{i}} = 0$).$B_r^{\mathrm{i}}$ in spherical coordinates from Eq. (3.73) is

$$B_r^{\mathrm{i}} = E_0 \frac{k}{\omega} \sin\theta \sin\phi e^{ikr\cos\theta} = E_0 \frac{k}{\omega} \Big(-\frac{1}{ikr} \Big) \sin\phi \frac{\partial}{\partial\theta} \Big(e^{ikr\cos\theta} \Big). \tag{3.81}$$

By substituting Eq. (3.75) into Eq. (3.81) and recalling the identity $\frac{\mathrm{d}P_l}{\mathrm{d}\theta} = -P_l^1(\cos\theta)$, B_r^{i} expansion

$$B_r^{\mathrm{i}} = E_0 \frac{k}{\omega} \sum_l (2l+1) i^{l-1} \frac{j_l(kr)}{kr} P_l^m(\cos\theta) \sin\phi.. \tag{3.82}$$

It can be seen that the azimuthal dependence is a sine function in this case, perpendicular, if $m = 1$, $Q_1(\phi) = \sin\phi + \cos\phi$, where in this case cosine will be disconsidered. Therefore the phase difference between the azimuthal component of the incident electric and magnetic fields is $\pi/2$. Comparing Eq. (3.82) with Eq. (3.53), the remaining components of the magnetic and electric fields in TE mode are acquired from those of the scattered wave in TE mode, replacing the complex coefficients b_{lm} by $E_0 \frac{k}{\omega}(2l+1)i^{l-1}$, as well as the radial function $h_l^{(1)}(kr)/r$ by the spherical Bessel function $j_l(kr)/kr$, and finally $Q_m(\phi)$ by $\sin\phi$. From this, the expanded remaining

components of the incident magnetic and electric fields are

$$B_\theta^{\mathrm{i}} = E_0 \frac{k}{\omega} \sum_l \frac{(2l+1)i^{l-1}}{l(l+1)} \frac{\psi_l'(kr)}{kr} \frac{\mathrm{d}P_l^1(\cos\theta)}{\mathrm{d}\theta} \sin\phi, \tag{3.83}$$

$$B_\phi^{\mathrm{i}} = E_0 \frac{k}{\omega} \sum_l \frac{(2l+1)i^{l-1}}{l(l+1)} \frac{\psi_l'(kr)}{kr} \frac{P_l^1(\cos\theta)}{\sin\theta} \cos\phi, \tag{3.84}$$

$$E_\theta^{\mathrm{i}} = E_0 \sum_l \frac{(2l+1)i^{l}}{l(l+1)} j_l(kr) \frac{P_l^1(\cos\theta)}{\sin\theta} \cos\phi, \tag{3.85}$$

$$E_\phi^{\mathrm{i}} = -E_0 \sum_l \frac{(2l+1)i^{l}}{l(l+1)} j_l(kr) \frac{\mathrm{d}P_l^1(\cos\theta)}{\mathrm{d}\theta} \sin\theta. \tag{3.86}$$

Coefficients from the scattered and internal field's components

The continuities of the tangential components of the electric and magnetic fields at the surface of the metallic sphere are applied to obtain the coefficients of the scattered wave and the internal field. The electromagnetic field outside the metallic sphere is the sum of the incident light and the scattered wave. The general solution of the electromagnetic field is the summation of TM mode and TE mode, then these two mode are needed to be differentiated. The TM mode and TE mode are denoted by the left superscript "tm" and "te", respectively. Thus, the boundary conditions of the tangential component of the electric and magnetic field at the surface of the metallic sphere are

$$({}^{\mathrm{tm}}E_\theta^{\mathrm{i}} + {}^{\mathrm{te}}E_\theta^{\mathrm{i}})_{(r=a)} + ({}^{\mathrm{tm}}E_\theta^{\mathrm{s}} + {}^{\mathrm{te}}E_\theta^{\mathrm{s}})_{(r=a)} = ({}^{\mathrm{tm}}E_\theta^{\mathrm{t}} + {}^{\mathrm{te}}E_\theta^{\mathrm{t}})_{(r=a)} \tag{3.87}$$

$$({}^{\mathrm{tm}}E_\phi^{\mathrm{i}} + {}^{\mathrm{te}}E_\phi^{\mathrm{i}})_{(r=a)} + ({}^{\mathrm{tm}}E_\phi^{\mathrm{s}} + {}^{\mathrm{te}}E_\phi^{\mathrm{s}})_{(r=a)} = ({}^{\mathrm{tm}}E_\phi^{\mathrm{t}} + {}^{\mathrm{te}}E_\phi^{\mathrm{t}})_{(r=a)} \tag{3.88}$$

$$({}^{\mathrm{tm}}B_\theta^{\mathrm{i}} + {}^{\mathrm{te}}B_\theta^{\mathrm{i}})_{(r=a)} + ({}^{\mathrm{tm}}B_\theta^{\mathrm{s}} + {}^{\mathrm{te}}B_\theta^{\mathrm{s}})_{(r=a)} = ({}^{\mathrm{tm}}B_\theta^{\mathrm{t}} + {}^{\mathrm{te}}B_\theta^{\mathrm{t}})_{(r=a)} \tag{3.89}$$

$$({}^{\mathrm{tm}}B_\phi^{\mathrm{i}} + {}^{\mathrm{te}}B_\phi^{\mathrm{i}})_{(r=a)} + ({}^{\mathrm{tm}}B_\phi^{\mathrm{s}} + {}^{\mathrm{te}}B_\phi^{\mathrm{s}})_{(r=a)} = ({}^{\mathrm{tm}}B_\phi^{\mathrm{t}} + {}^{\mathrm{te}}B_\phi^{\mathrm{t}})_{(r=a)} \tag{3.90}$$

The first step is finding the coupled equations of these coefficients from Eq. (3.87) to Eq. (3.90). Two coupled equations are acquired from a pair of boundary conditions for E_θ and E_ϕ, and the other two coupled equations are obtained from another pair

of boundary conditions for B_θ and B_ϕ. Then, four coupled equations to be solved for the coefficients of the scattered wave and the internal field in both TM and TE modes are sought. E_θ^{i} in TM mode and TE mode are written in Eqs. (3.77) and (3.85). The E_θ^{s} in TM mode and TE modes are written in Eqs. (3.49) and (3.56), respectively, and E_θ^{t} in TM mode and TE mode are shown in Eqs. (3.64) and (3.71), respectively. All of these equations are substituted into Eq. (3.91), and then the terms with the same angular dependence are grouped so that the integral identities of the associated Legendre polynomial in Appendix Eqs. $(A.27) - (A.28)$ can be later applied. After substituting and grouping as mentioned,

$$\begin{aligned} 0 &= \sum_{l=1}^{\infty}\Big[E_0\frac{(2l+1)i^{l-1}}{l(l+1)}\frac{\psi_l^{'}(x)}{x}+\frac{a_{lm}}{l(l+1)}\frac{\zeta_l^{'}(x)}{a}-\frac{d_{lm}}{l(l+1)}\frac{\psi_l^{'}(mx)}{a}\Big]\frac{\mathrm{d}P_l^m(\cos\theta)}{\mathrm{d}\theta}+ \\ &\quad \sum_{l=1}^{\infty}\Big[E_0\frac{(2l+1)i^{l}}{l(l+1)}j_l(x)+\frac{i\omega b_{lm}}{l(l+1)}h_l^{(1)}(x)-\frac{i\omega c_{lm}}{l(l+1)}j_l(mx)\Big]\frac{P_l^m(\cos\theta)}{\sin\theta}. \quad (3.91) \end{aligned}$$

For the boundary condition of E_ϕ, the expansion of E_ϕ^{i} into TM mode and TE mode are written in Eq. (3.78) and Eq. (3.85). The solutions of E_ϕ^{s} in TM mode and TE mode in Eq. (3.50) and Eq. (3.57). As for E_ϕ^{t} in TM mode and TE mode, in Eq. (3.65) and Eq. (3.72). Are substituted into Eq. (3.88). Then, by grouping the terms with the same angular dependence, Eq. (3.88) becomes

$$\begin{aligned} 0 &= \sum_{l=1}^{\infty}\Big[E_0\frac{(2l+1)i^{l-1}}{l(l+1)}\frac{\psi_l^{'}(x)}{x}+\frac{a_{lm}}{l(l+1)}\frac{\zeta_l^{'}(x)}{a}-\frac{d_{lm}}{l(l+1)}\frac{\psi_l^{'}(mx)}{a}\Big]\frac{P_l^m(\cos\theta)}{\sin\theta}+ \\ &\quad \sum_{l=1}^{\infty}\Big[E_0\frac{(2l+1)i^{l}}{l(l+1)}j_l(x)+\frac{i\omega b_{lm}}{l(l+1)}h_l^{(1)}(x)-\frac{i\omega c_{lm}}{l(l+1)}j_l(mx)\Big]\frac{\mathrm{d}P_l^m(\cos\theta)}{\mathrm{d}\theta}. \quad (3.92) \end{aligned}$$

There are two angular functions, $\frac{P_l^m(\cos\theta)}{\sin\theta}$ and $\frac{\mathrm{d}P_l^m(\cos\theta)}{\mathrm{d}\theta}$, in both Eq. (3.91) and Eq. (3.92). Furthermore, the l-dependence coefficient in $\frac{P_l^m(\cos\theta)}{\sin\theta}$ in Eq. (3.92) is the same as that one of $\frac{\mathrm{d}P_l^m(\cos\theta)}{\mathrm{d}\theta}$ in Eq. (3.91). This satisfies the integral identities $(A.27)$ and $(A.28)$ of the associated Legendre polynomials, so that derivation of two coupled equations of the coefficients of the scattered wave and the internal field

is possible. From the integral identities of the associated Legendre polynomial in Eqs. (3.91) and (3.92), the two linear coupled equations of the coefficients

$$\zeta_l^{'}(x)a_{lm} - \psi_l^{'}(mx)d_{lm} = -E_0 a(2l+1)i^{l-1}\frac{\psi_l^{'}(x)}{x}, \tag{3.93}$$

$$h_l^{(1)}(x)b_{lm} - j_l(mx)c_{l1} = -E_0\frac{(2l+1)i^{l-1}}{\omega}j_l(x). \tag{3.94}$$

Similarly, from Eqs. (3.89) and (3.90), and the integral identities of the associated Legendre polynomial ($A.27$) and ($A.28$), the other two coupled equations of the coefficients of the scattered wave and the internal one are

$$h_l^{(1)}a_{lm} - m^2 j_l(mx)d_{lm} = -E_0\frac{(2l+1)i^{(l-1)}}{k}j_l(x), \tag{3.95}$$

$$\zeta_l^{'}(x)b_{lm} - \psi_l^{'}(mx)c_{lm} = -E_0\frac{(2l+1)i^{(l-1)}}{\omega}\psi_l^{'}(x). \tag{3.96}$$

Then, the coefficients of the scattered wave and the internal field in TM mode are a_{lm} and d_{lm}, from the linear equations (3.93) and (3.96). Eqs. (3.94) and (3.96) are solved for the coefficients of the scattered wave and the internal field in TE mode, b_{lm} and c_{lm}.

$$a_{lm} = -E_0\frac{(2l+1)i^{l-1}}{k}\left[\frac{m\psi_l(mx)\psi_l^{'}(x) - \psi_l^{'}(mx)\psi_l(x)}{m\psi_l(mx)\zeta_l^{'}(x) - \psi_l^{'}(mx)\zeta_l(x)}\right], \tag{3.97}$$

$$d_{lm} = E_0\frac{(2l+1)i^{l-1}}{\tilde{k}}\left[\frac{m\psi_l(x)\zeta_l^{'}(x) - m\psi_l^{'}(x)\zeta_l(x)}{m\psi_l(mx)\zeta_l^{'}(x) - \psi_l^{'}(mx)\zeta_l(x)}\right], \tag{3.98}$$

$$b_{lm} = -E_0\frac{(2l+1)i^{l-1}}{\omega}\left[\frac{\psi_l(mx)\psi_l^{'}(x) - m\psi_l^{'}(mx)\psi_l(x)}{\psi_l(mx)\zeta_l^{'}(x) - m\psi_l^{'}(mx)\zeta_l(x)}\right], \tag{3.99}$$

$$c_{lm} = E_0\frac{(2l+1)i^{l-1}}{\omega}\left[\frac{m\psi_l(x)\zeta_l^{'}(x) - m\psi_l^{'}(x)\zeta_l(x)}{\psi_l(mx)\zeta_l^{'}(x) - m\psi_l^{'}(mx)\zeta_l(x)}\right], \tag{3.100}$$

where $x = ka$.

The coefficients of the same mode have the same denominator, but these denominators are different between two modes. The resonance of the electromagnetic field occurs when the denominator becomes zero, thus the resonance conditions for each

value of l are different between TM mode and TE mode. For TM mode, the resonance corresponds to the resonance of the electric multipole oscillation while the resonance of TE mode corresponds to the magnetic multipole oscillation.

The scattered electric and magnetic fields which are denoted by the right superscript "s" in TM mode are then obtained by substituting the scattering coefficients a_{lm} written in Eq. (3.97) into Eq. (3.39) , and Eqs. (3.49)-(3.52). These solutions are expressed as follows

$$
\begin{aligned}
{}^{\mathrm{tm}}E_r^{\mathrm{s}} &= -E_0\sum_{l=1}^{\infty}(2l+1)i^{l-1}\left[\frac{m\psi_l(mx)\psi_l^{'}(x)-\psi_l^{'}(mx)\psi_l(x)}{m\psi_l(mx)\zeta_l^{'}(x)-\psi_l^{'}(mx)\zeta_l(x)}\right]\frac{h_l^{(1)}(kr)}{kr}P_l^m(\cos\theta)\cos\phi, && (3.101)\\
{}^{\mathrm{tm}}E_\theta^{\mathrm{s}} &= -E_0\sum_{l=1}^{\infty}\frac{(2l+1)i^{l-1}}{l(l+1)}\left[\frac{m\psi_l(mx)\psi_l^{'}(x)-\psi_l^{'}(mx)\psi_l(x)}{m\psi_l(mx)\zeta_l^{'}(x)-\psi_l^{'}(mx)\zeta_l(x)}\right]\frac{\zeta_l^{'}(kr)}{kr}\frac{\mathrm{d}P_l^m(\cos\theta)}{\mathrm{d}\theta}\cos\phi, && (3.102)\\
{}^{\mathrm{tm}}E_\phi^{\mathrm{s}} &= E_0\sum_{l=1}^{\infty}\frac{(2l+1)i^{l-1}}{l(l+1)}\left[\frac{m\psi_l(mx)\psi_l^{'}(x)-\psi_l^{'}(mx)\psi_l(x)}{m\psi_l(mx)\zeta_l^{'}(x)-\psi_l^{'}(mx)\zeta_l(x)}\right]\frac{\zeta_l^{'}(kr)}{kr}\frac{P_l^m(\cos\theta)}{\sin\theta}\sin\phi, && (3.103)\\
{}^{\mathrm{tm}}B_\theta^{\mathrm{s}} &= -E_0\frac{k}{\omega}\sum_{l=1}^{\infty}\frac{(2l+1)i^{l}}{l(l+1)}\left[\frac{m\psi_l(mx)\psi_l^{'}(x)-\psi_l^{'}(mx)\psi_l(x)}{m\psi_l(mx)\zeta_l^{'}(x)-\psi_l^{'}(mx)\zeta_l(x)}\right]h_l^{(1)}(kr)\frac{P_l^m(\cos\theta)}{\sin\theta}\sin\phi, && (3.104)\\
{}^{\mathrm{tm}}B_\phi^{\mathrm{s}} &= -E_0\frac{k}{\omega}\sum_{l=1}^{\infty}\frac{(2l+1)i^{l}}{l(l+1)}\left[\frac{m\psi_l(mx)\psi_l^{'}(x)-\psi_l^{'}(mx)\psi_l(x)}{m\psi_l(mx)\zeta_l^{'}(x)-\psi_l^{'}(mx)\zeta_l(x)}\right]h_l^{(1)}(kr)\frac{\mathrm{d}P_l^m(\cos\theta)}{\mathrm{d}\theta}\cos\phi. && (3.105)
\end{aligned}
$$

The scattered electric and magnetic fields in TE mode are obtained by substituting the scattering coefficient b_{lm} written in Eq. (3.99) into Eq. (3.53), and Eqs. (3.54)-(3.57).

$$
\begin{aligned}
{}^{\mathrm{te}}B_r^{\mathrm{s}} &= -E_0\frac{k}{\omega}\sum_{l=1}^{\infty}(2l+1)i^{l-1}\left[\frac{\psi_l(mx)\psi_l^{'}(x)-m\psi_l^{'}(mx)\psi_l(x)}{\psi_l(mx)\zeta_l^{'}(x)-m\psi_l^{'}(mx)\zeta_l(x)}\right]\frac{h_l^{(1)}(kr)}{kr}P_l^m(\cos\theta)\sin\phi, && (3.106)\\
{}^{\mathrm{te}}B_\theta^{\mathrm{s}} &= -E_0\frac{k}{\omega}\sum_{l=1}^{\infty}\frac{(2l+1)i^{l-1}}{l(l+1)}\left[\frac{\psi_l(mx)\psi_l^{'}(x)-m\psi_l^{'}(mx)\psi_l(x)}{\psi_l(mx)\zeta_l^{'}(x)-m\psi_l^{'}(mx)\zeta_l(x)}\right]\frac{\zeta_l^{'}(kr)}{kr}\frac{\mathrm{d}P_l^1(\cos\theta)}{\mathrm{d}\theta}\sin\phi, && (3.107)\\
{}^{\mathrm{te}}B_\phi^{\mathrm{s}} &= -E_0\frac{k}{\omega}\sum_{l=1}^{\infty}\frac{(2l+1)i^{l-1}}{l(l+1)}\left[\frac{\psi_l(mx)\psi_l^{'}(x)-m\psi_l^{'}(mx)\psi_l(x)}{\psi_l(mx)\zeta_l^{'}(x)-m\psi_l^{'}(mx)\zeta_l(x)}\right]\frac{\zeta_l^{'}(kr)}{kr}\frac{P_l^m(\cos\theta)}{\sin\theta}\cos\phi, && (3.108)\\
{}^{\mathrm{te}}E_\theta^{\mathrm{s}} &= -E_0\sum_{l=1}^{\infty}\frac{(2l+1)i^{l}}{l(l+1)}\left[\frac{\psi_l(mx)\psi_l^{'}(x)-m\psi_l^{'}(mx)\psi_l(x)}{\psi_l(mx)\zeta_l^{'}(x)-m\psi_l^{'}(mx)\zeta_l(x)}\right]h_l^{(1)}(kr)\frac{P_l^m(\cos\theta)}{\sin\theta}\cos\phi, && (3.109)\\
{}^{\mathrm{te}}E_\phi^{\mathrm{s}} &= E_0\sum_{l=1}^{\infty}\frac{(2l+1)i^{l}}{l(l+1)}\left[\frac{\psi_l(mx)\psi_l^{'}(x)-m\psi_l^{'}(mx)\psi_l(x)}{\psi_l(mx)\zeta_l^{'}(x)-m\psi_l^{'}(mx)\zeta_l(x)}\right]h_l^{(1)}(kr)\frac{\mathrm{d}P_l^m(\cos\theta)}{\mathrm{d}\theta}\sin\phi. && (3.110)
\end{aligned}
$$

The internal electric and magnetic fields which are denoted by the right superscript "t" in TM are complete with the internal coefficient d_{lm} from Eq. (3.98) into

Eq. (3.63), and Eqs. (3.64)-(3.67).

$$
\begin{aligned}
{}^{\mathrm{tm}}E_r^{\mathrm{t}} &= E_0 \sum_{l=1}^{\infty} (2l+1) i^{l-1} \left[\frac{m\psi_l(x)\zeta_l^{'}(x) - m\psi_l^{'}(x)\zeta_l(x)}{m\psi_l(mx)\zeta_l^{'}(x) - \psi_l^{'}(mx)\zeta_l(x)} \right] \frac{j_l(\tilde{k}r)}{\tilde{k}r} P_l^m(\cos\theta)\cos\phi, && (3.111)\\
{}^{\mathrm{tm}}E_\theta^{\mathrm{t}} &= E_0 \sum_{l=1}^{\infty} \frac{(2l+1) i^{l-1}}{l(l+1)} \left[\frac{m\psi_l(x)\zeta_l^{'}(x) - m\psi_l^{'}(x)\zeta_l(x)}{m\psi_l(mx)\zeta_l^{'}(x) - \psi_l^{'}(mx)\zeta_l(x)} \right] \frac{\psi_l^{'}(\tilde{k}r)}{\tilde{k}r} \frac{\partial P_l^m(\cos\theta)}{\partial\theta} \cos\phi, && (3.112)\\
{}^{\mathrm{tm}}E_\phi^{\mathrm{t}} &= -E_0 \sum_{l=1}^{\infty} \frac{(2l+1) i^{l-1}}{l(l+1)} \left[\frac{m\psi_l(x)\zeta_l^{'}(x) - m\psi_l^{'}(x)\zeta_l(x)}{m\psi_l(mx)\zeta_l^{'}(x) - \psi_l^{'}(mx)\zeta_l(x)} \right] \frac{\psi_l^{'}(\tilde{k}r)}{\tilde{k}r} \frac{P_l^m(\cos\theta)}{\sin\theta} \sin\phi, && (3.113)\\
{}^{\mathrm{tm}}B_\theta^{\mathrm{t}} &= E_0 \frac{\tilde{k}}{\omega} \sum_{l=1}^{\infty} \frac{(2l+1) i^{l}}{l(l+1)} \left[\frac{m\psi_l(x)\zeta_l^{'}(x) - m\psi_l^{'}(x)\zeta_l(x)}{m\psi_l(mx)\zeta_l^{'}(x) - \psi_l^{'}(mx)\zeta_l(x)} \right] j_l(\tilde{k}r) \frac{P_l^m(\cos\theta)}{\sin\theta} \sin\phi, && (3.114)\\
{}^{\mathrm{tm}}B_\phi^{\mathrm{t}} &= E_0 \frac{\tilde{k}}{\omega} \sum_{l=1}^{\infty} \frac{(2l+1) i^{l}}{l(l+1)} \left[\frac{m\psi_l(x)\zeta_l^{'}(x) - m\psi_l^{'}(x)\zeta_l(x)}{m\psi_l(mx)\zeta_l^{'}(x) - \psi_l^{'}(mx)\zeta_l(x)} \right] j_l(\tilde{k}r) \frac{\mathrm{d}P_l^m(\cos\theta)}{\mathrm{d}\theta} \cos\phi. && (3.115)
\end{aligned}
$$

Finally, the internal electric and magnetic fields in TE mode are obtained by substituting the internal coefficient c_{lm} into Eq. (3.68), and Eqs. (3.69)-(3.72).

$$
\begin{aligned}
{}^{\mathrm{te}}B_r^{\mathrm{t}} &= E_0 \frac{\tilde{k}}{\omega} \sum_{l=1}^{\infty} (2l+1) i^{l-1} \left[\frac{m\psi_l(x)\zeta_l^{'}(x) - m\psi_l^{'}(x)\zeta_l(x)}{\psi_l(mx)\zeta_l^{'}(x) - m\psi_l^{'}(mx)\zeta_l(x)} \right] \frac{j_l(\tilde{k}r)}{\tilde{k}r} P_l^m(\cos\theta)\sin\phi, && (3.116)\\
{}^{\mathrm{te}}B_\theta^{\mathrm{t}} &= E_0 \frac{\tilde{k}}{\omega} \sum_{l=1}^{\infty} \frac{(2l+1) i^{l-1}}{l(l+1)} \left[\frac{m\psi_l(x)\zeta_l^{'}(x) - m\psi_l^{'}(x)\zeta_l(x)}{\psi_l(mx)\zeta_l^{'}(x) - m\psi_l^{'}(mx)\zeta_l(x)} \right] \frac{\psi_l^{'}(\tilde{k}r)}{\tilde{k}r} \frac{\mathrm{d}P_l^m(\cos\theta)}{\mathrm{d}\theta} \sin\phi, && (3.117)\\
{}^{\mathrm{te}}B_\phi^{\mathrm{t}} &= E_0 \frac{\tilde{k}}{\omega} \sum_{l=1}^{\infty} \frac{(2l+1) i^{l-1}}{l(l+1)} \left[\frac{m\psi_l(x)\zeta_l^{'}(x) - m\psi_l^{'}(x)\zeta_l(x)}{\psi_l(mx)\zeta_l^{'}(x) - m\psi_l^{'}(mx)\zeta_l(x)} \right] \frac{\psi_l^{'}(\tilde{k}r)}{\tilde{k}r} \frac{P_l^m(\cos\theta)}{\sin\theta} \cos\phi, && (3.118)\\
{}^{\mathrm{te}}E_\theta^{\mathrm{t}} &= E_0 \sum_{l=1}^{\infty} \frac{(2l+1) i^{l}}{l(l+1)} \left[\frac{m\psi_l(x)\zeta_l^{'}(x) - m\psi_l^{'}(x)\zeta_l(x)}{\psi_l(mx)\zeta_l^{'}(x) - m\psi_l^{'}(mx)\zeta_l(x)} \right] j_l(\tilde{k}r) \frac{P_l^m(\cos\theta)}{\sin\theta} \cos\phi, && (3.119)\\
{}^{\mathrm{te}}E_\phi^{\mathrm{t}} &= -E_0 \sum_{l=1}^{\infty} \frac{(2l+1) i^{l}}{l(l+1)} \left[\frac{m\psi_l(x)\zeta_l^{'}(x) - m\psi_l^{'}(x)\zeta_l(x)}{\psi_l(mx)\zeta_l^{'}(x) - m\psi_l^{'}(mx)\zeta_l(x)} \right] j_l(\tilde{k}r) \frac{\mathrm{d}P_l^m(\cos\theta)}{\mathrm{d}\theta} \sin\phi. && (3.120)
\end{aligned}
$$

3.4 Exciton Theory in carbon nanotubes

An exciton is a bounded electron-hole pair pseudoparticle generated when an electron from the valence band is excited into the conduction band, but remains linked to the hole in the valence band due to Coulombian interaction between photo-excited electron and hole [10]. Since carbon nanotube is a structure that only has one degree

of freedom, an exciton can actually be excited at room temperature, however, it is impossible this phenomena to happen in a bulk three dimensional semiconductor due to the low binding energy of the exciton, about 10 meV. The exciton wavefunction is localized in the real and k spaces. In the latter, the exciton wavefunction is a linear combination of Bloch wavefunctions so that the exciton has two kinds of wave vectors defined as : (i) the wave vector of the center of mass, $\boldsymbol{K} = (\boldsymbol{k}_c - \boldsymbol{k}_v)/2$ and (ii) the wave vector of the relative coordinate, $\boldsymbol{k} = \boldsymbol{k}_c + \boldsymbol{k}_v$, where $\boldsymbol{k}_c$ and $\boldsymbol{k}_v$ are, respectively, the wave vectors of the electron in the conduction band and the hole in the valence band, this is a single particle picture. It should be noted that the hole has an opposite sign for its wave vector and effective mass compared to the electron. $\boldsymbol{K}$ is a good quantum number and then the dispersion energy of the exciton is written as a function of $\boldsymbol{K}$ [2]. If the optical transition along the tube axis is considered the vertical transition, that is, $\boldsymbol{k}_c = \boldsymbol{k}_v$, must be satisfied [13]. Thus, only a $\boldsymbol{K} = 0$ exciton can have its components recombined into emitting a photon, a "bright exciton", but in the case of a $\boldsymbol{K} \neq 0$ exciton, the non-vertical transition, its components will not be recombined directly into the emission of a photon, a "dark exciton" [2]. The spin of the exciton is defined as a total spin S which can be 0 and 1. The exciton spin $S = 0$ is called the "singlet exciton", and the exciton spin $S = 1$ is called the "triplet exciton". The triplet exciton is a dark one in terms of the dipole selection rule.

3.4.1 Exciton Symmetries and the Dipole selection rules for carbon nanotubes

Carbon nanotubes excitons can be distinguished not only by their symmetry [35], but also by their center of mass wave vector [2], following these properties, 4 types of excitons are defined, A_1 , A_2 , E and E^* . The first two excitons that have $\boldsymbol{K} = 0$, that is why they are grouped under the same label, as for the latter two, they have

Fig. 3-6(a): fig:/exciton-regions.eps
Fig. 3-6(b): fig:/swnt-symmetry.eps

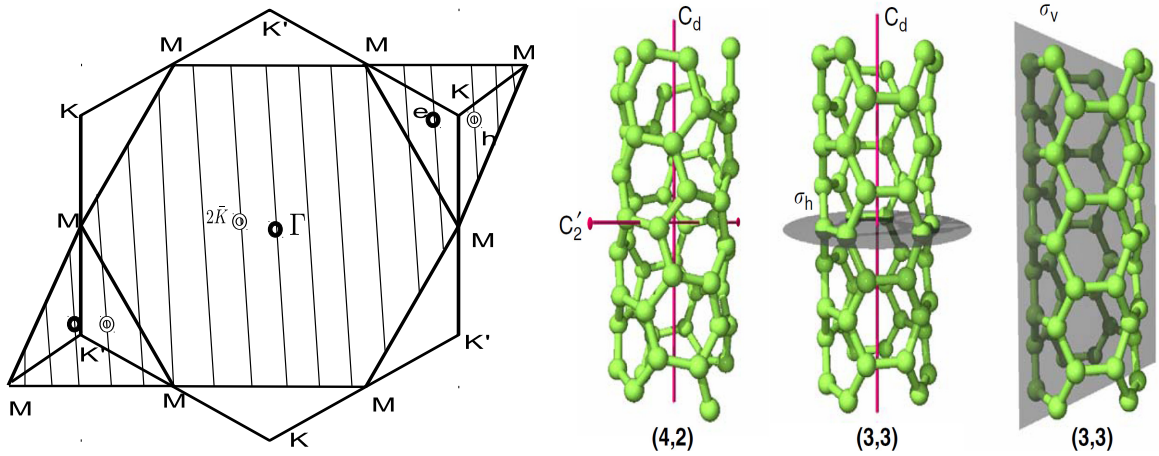

(a) (b)

Figure 3-6: (a)Electron-hole pairs in three inequivalent regions of the Brillouin zone of graphene for (6,5) SWNT, where A excitons correspond to an electron and hole pair in K or $K^{'}$ regions, in which $2\boldsymbol{K} = \boldsymbol{k}_c - \boldsymbol{k}_v$ lies in the Γ point central region. E and E^* excitons correspond to an electron from K region and an hole from $K^{'}$ region, in which $2\boldsymbol{K}$ lies in K and $K^{'}$ regions [2]. (b) Symmetries of a chiral (4,2) SWNT and an armchair (3,3) [35].The tube axis of symmetry is C_d where the d stands for $\frac{2\pi}{d}$ rotations, in this case $d = 2$, and the axis perpendicular to the tube axis is $C_2^{'}$ another π rotation symmetry axis. The horizontal and vertical symmetry planes for (3,3) SWNT, σ_h and σ_v, are the horizontal and vertical mirror planes, correspondingly.

$K \neq 0$, as a result they are "dark", and will be neglected from this point forward since the focus is to investigate the contribution given to the Raman intensity in TERS experiment, dependent on the emission of a photon by recombination. Each of these types are shown in Fig. 3-6, the A excitons that lie in the Γ region have $2\boldsymbol{K} = \boldsymbol{k}_c - \boldsymbol{k}_v$ since they are together either in the same K region or in the $K^{'}$, as for the E and E^* excitons $2\boldsymbol{K}$ in K and $K^{'}$ as electron and hole are in different regions.

The dipole vector selection rules for the A excitons is now further discussed in terms of their symmetry preserving operations. A_1 and A_2 are the irreducible representation defined by the character table of point group D_N for chiral nanotubes, where N is the number of hexagons in the nanotube unit cell. The A_1 exciton is

symmetric with respect to a C_2 rotation, by π, about the axis perpendicular to the tube axis, while the A_2 exciton is anti-symmetric. There are $N/2$ axes, $C_2^{'}$, goes through the center of the bonds between two nonequivalent carbon atoms as shown in the Fig. 3-6(b), and the other $N/2$ axes, $C_2^{''}$, that can go through the center of each hexagons. For achiral nanotubes, armchair and zigzag, there are additional symmetry operations: inversion, horizontal reflection and vertical reflection. The mirror planes of the horizontal vertical reflections for armchair carbon nanotube are shown in Fig. 3-6(b). Then, additional symbols, g gerade, which is German for even, and u ungerade, which is German for uneven, odd, are included in A_1 and A_2 to be A_{1g}, A_{1u}, A_{2g}, and A_{2u}. These symmetries are in the point group D_{Nh} [10].

According to the dipole selection rules without the near field factor, the transition probability is proportional to $|\hat{\boldsymbol{P}} \cdot E_0 \cdot \langle \Psi_f | \nabla | \Psi_i \rangle|^2$ with $|\Psi_f\rangle$ and $|\Psi_i\rangle$ the excited and ground states, and $\hat{\boldsymbol{P}}$, the polarization of the incident laser light. The ground state $|\Psi_i\rangle$ is totally symmetric, and the ∇ operator over $|\Psi_i\rangle$, which is initially completely symmetric, yet, an odd function, becomes antisymmetric under C_2 rotation. The excited state $|\Psi_f\rangle$ must be antisymmetric under C_2 rotation a restriction to have a non-zero, $\langle \Psi_f | \nabla | \Psi_i \rangle$transition probability. Therefore, A_2 excitons are bright ones and A_1 excitons are dark for chiral nanotubes. Nevertheless, it is worth emphasizing that in two photon photo luminescence experiment, the A_1 excitons become optically active and A_2 excitons become dark [18]. For zigzag and armchair carbon nanotubes, the A_{2u} exciton are dipole optically active or bright and the remaining ones are all dark excitons [35]. However, in the two photon experiment, the A_{1g} excitons are bright and the remaining excitons become dark [18].

3.4.2 Carbon nanotubes Exciton's Wavefunctions

As stated before the exciton is a pseudoparticle that has a very short life time and it is composed of two particles, the electron that was excited from the valence band to the conduction band which still is linked to the hole that remained in the valence

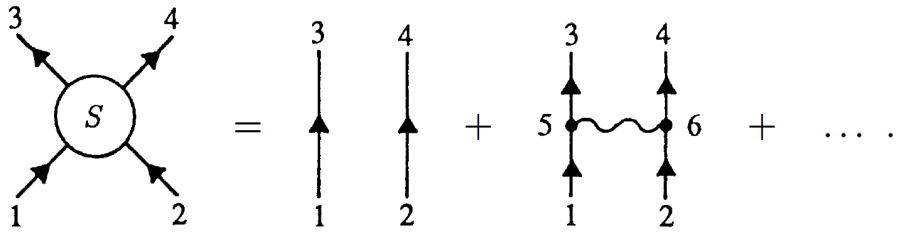

Figure 3-7: The possible interactions between the electron in the conduction band and the hole in the valence band depicted by Feynman's diagrams. S is the kernel where the interactions between the incident particles 1 and 2 occur resulting in the exiting particles 3 and 4. The first event on the right side is a no interaction possibility whereas the second event on the right side is an electromagnetic interaction between 1 and 2 resulting in 3 and 4.[36]

band, their bounding force is a Coulombiam one since they are of opposite charges. In order to obtain the exciton's more than relevant information, such as its wavefunction, eigen-energies and others, a set of possible interactions between the electron and the hole have to be taken into account. An infinite set of interactions may occur, yet only the most probable ones are going to be considered since the exciton lifetime is finite [36].

The exciton energy Ω^n and its wavefunction Ψ^n are obtained by solving the Bethe-Salpeter (BS-equation), depending on the possible interactions between the hole and the electron, which are represented by their wavevectors $\boldsymbol{k}_v$ and $\boldsymbol{k}_c$.

$$\sum_{\boldsymbol{k}_c\boldsymbol{k}_v}\Big\{[E(\boldsymbol{k}_c)-E(\boldsymbol{k}_v)]\delta_{\boldsymbol{k}'_c\boldsymbol{k}_c}\delta_{\boldsymbol{k}'_v\boldsymbol{k}_v}+S(\boldsymbol{k}'_c\boldsymbol{k}'_v,\boldsymbol{k}_c\boldsymbol{k}_v)\Big\}\Psi^n(\boldsymbol{k}_c\boldsymbol{k}_v)=\Omega^n\Psi^n(\boldsymbol{k}'_c\boldsymbol{k}'_v) \quad (3.121)$$

where $E(\boldsymbol{k}_c)-E(\boldsymbol{k}_v)$ is the gap energy between the valence and conduction bands for the hole and the electron energy levelling the $\delta_{\boldsymbol{k}'_c\boldsymbol{k}_c}\delta_{\boldsymbol{k}'_v\boldsymbol{k}_v}$ is the condition for the vertical transitions, which are the focus since only they are bright, $S(\boldsymbol{k}'_c\boldsymbol{k}'_v,\boldsymbol{k}_c\boldsymbol{k}_v)$ is the kernel of possible interactions

$$S(\boldsymbol{k}'_c\boldsymbol{k}'_v,\boldsymbol{k}_c\boldsymbol{k}_v)=-S^{\mathrm{d}}(\boldsymbol{k}'_c\boldsymbol{k}'_v,\boldsymbol{k}_c\boldsymbol{k}_v)+2\delta_S S^{\mathrm{x}}(\boldsymbol{k}'_c\boldsymbol{k}'_v,\boldsymbol{k}_c\boldsymbol{k}_v), \quad (3.122)$$

Fig. 3-7: fig:/fig:exciton-events.eps

where S^{d} is the direct interaction obtained from screened Coulomb potential, S^{x} is the exchange interaction obtained from bare Coulomb potential, δ_S is 1 or 0 for singlet or triplet excitons, [10].

Wave vectors from only the corresponding cutting line, μ index, to the E_{ii} transition for small-diameter nanotubes (0.5< d_t <2.0 nm) because the Coulomb interaction is present in a larger region than the diameter d_t of SWNT [2]. By solving the BS-equation, Eq.3.121, the exciton energy dispersion is obtained with discrete energy levels. Each energy level is labeled by the integer $\nu = 0, 1, 2, 3, \ldots$. Then, the exciton wavefunction $|\boldsymbol{k}, \boldsymbol{K}\rangle$ of the vertical transition near K point

$$|\boldsymbol{k}, \boldsymbol{K}\rangle = \sum_k Z_k^\nu \Psi_k^c(\boldsymbol{r}_e)\Psi_k^{v*}(\boldsymbol{r}_h). \tag{3.123}$$

where Z_k^ν are the exciton wavefunction amplitude obtained by solving the BS-equation. Z_k^ν is the envelope function [37] that arises from the connecting the extremes of the wave function, and ν can be either even and odd depending on the reflection symmetry about the plane perpendicular to the tube axis, the horizontal mirror plane σ_h. Ψ^c and Ψ^v are the one particle wavefunctions of the valence band, hole, and the conduction band, electron. The one particle wavefunction are written as a linear combination of the Bloch wavefunctions $\Phi_{\mathrm{A}}(\boldsymbol{k}, \boldsymbol{r})$ and $\Phi_{\mathrm{B}}(\boldsymbol{k}, \boldsymbol{r})$ of A and B carbon atoms, in the graphene lattice

$$\Psi_k^{v(c)}(\boldsymbol{r}) = c_{\mathrm{A}}^{v(c)}\Phi_{\mathrm{A}}(\boldsymbol{k}, \boldsymbol{r}) + c_{\mathrm{B}}^{v(c)}\Phi_{\mathrm{B}}(\boldsymbol{k}, \boldsymbol{r}), \tag{3.124}$$

where the Bloch wavefunction $\Phi_{\mathrm{A(B)}}(\boldsymbol{k}, \boldsymbol{r})$

$$\Phi_{\mathrm{A(B)}}(\boldsymbol{k}, \boldsymbol{r}) = \frac{1}{\sqrt{N}} \sum_{j=1}^{N} e^{i\boldsymbol{k}\cdot\boldsymbol{R}^j_{\mathrm{A(B)}}} \varphi\Big(\boldsymbol{r} - \boldsymbol{R}^j_{\mathrm{A(B)}}\Big), \tag{3.125}$$

where $\varphi\Big(\boldsymbol{r} - \boldsymbol{R}^j_{\mathrm{A(B)}}\Big)$ is the $2pz$ atomic orbital centered in A(B) atom in the unit cell

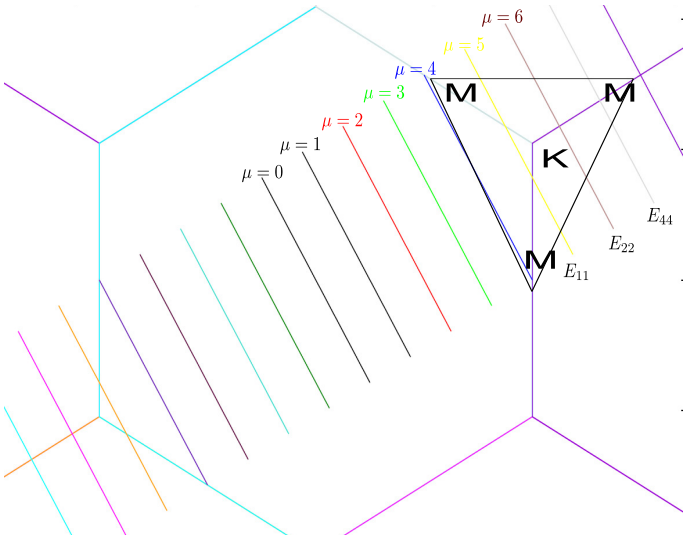

Figure 3-8: Reciprocal lattice of a (8,0) SWNT with the cutting lines displayed, as explained before only the excitons with the $\boldsymbol{k}$ in K region are bright, and here are the exciton transition energies observed experimentally with the matching cutting lines, μ index.[14]

of the graphene lattice.

The A excitons are obtained from the k wave vectors of electron and hole from K and K' as in Fig.3-8 points so that the wave vector of the center of mass $\boldsymbol{K}$ of the excitons become zero as in a vertical transition. The $\boldsymbol{k}$ wave vector around the K' point has an opposite sign in regard of the $\boldsymbol{k}$ from K point, yet $\boldsymbol{K}$ is the same for both K and K' points. The A_1 exciton is symmetric , and the A_2 exciton is antisymmetric under C_2 rotation with respect to the perpendicular axis to the tube. Therefore, the linear combination between the wave vectors from K and K' points excitons for the types A_1 and A_2 satisfying the symmetry [2] may be written

$$A_{2,1} = \frac{1}{\sqrt{2}}(|\boldsymbol{k}, \boldsymbol{K}\rangle \pm |-\boldsymbol{k}, \boldsymbol{K}\rangle). \tag{3.126}$$

where $|\boldsymbol{k}, \boldsymbol{K}\rangle$ is the exciton wavefunction from K point, and $|-\boldsymbol{k}, \boldsymbol{K}\rangle$ is the exciton wave function for the K' point, written in Eq. (3.123). The plus sign is correspondent

Fig. 3-8: fig:/fig:exciton-transcut.eps

to the A_2 exciton, and the minus sign is for the A_1 exciton. The excitons symmetry is confirmed if the C_2 rotation is taken over the above equation, Eq. (3.126) and then checking the relation $\hat{C}_2\Psi_v = \Psi_v^*$ and $\hat{C}_2\Psi_c = -\Psi_c^*$. By substituting Eq. (3.123) into Eq. (3.126), the A_2 exciton wavefunction Ψ_2^ν with an electron on a s' atom in a graphene lattice j', and hole on another s atom in a graphene lattice j, following [2]

$$\Psi_2^\nu(j's', js) = \sum_k Z_k^\nu \mathrm{Re}\big[C_{s'}^c(\boldsymbol{k})C_s^{v*}(\boldsymbol{k})e^{i\boldsymbol{k}\cdot(\boldsymbol{R}_{j's'}-\boldsymbol{R}_{ju})}\big]. \tag{3.127}$$

Ψ_2^ν for $\nu = 0, 1, 2$ of the E_{22} transition for (8,0) SWNT obtained from STB method is shown in Fig. 3-9. In Fig. 3-9(a) and 3-9(c), the exciton wavefunction is shown for the electron and hole on an A atom that is (A,A), since the exciton wavefunction for (B,B) , (A,B), or (B,A) are all identical. Yet, the for $\nu = 1$, (A,A) or (B,B) is not allowed. Then, the exciton wavefunction in Fig. 3-9(b) is for (A,B) case [2]. It is noted here that the x-axis in the original paper should be divided by the lattice constant, 2.46 nm, to be consistent with this plot. According to Fig. 3-9, three excitonic states are orthogonal. Then, the nodes appear on the tube axis according to the value of ν. The A_2^0 is well localized with the full width at half maximum about 2 nm. The exciton becomes delocalized if energy and tube diameter are increased. Ψ_2^0 and Ψ_2^2 are symmetric, and Ψ_2^1 is anti-symmetric with respect to the reflection about the plane perpendicular to the tube axis. Therefore, Ψ_2^0 and Ψ_2^2 are represented by A_{2g}, whereas Ψ_2^1 is by A_{2u}, for excitons in armchair and zigzag SWNTs.

The exciton wavefunctions of A excitons also arise from the second quantization where the electron creation operator, $\hat{c}^\dagger$ and the electron annihilation operator $\hat{c}$ are introduced. The wavefunction of the conduction band is obtained from the application of the creation operator over the ground state $|0\rangle$, and the wavefunction of the valence band from the annihilation operator over the ground state. Then, the A excitons

becomes

$$\Psi(A_2^\nu) = \frac{1}{\sqrt{2}}\sum_k Z_k^\nu\Big(\hat{c}_k^\dagger\hat{c}_k + \hat{c}_{-k}^\dagger\hat{c}_{-k}\Big)\Big|0\Big\rangle, \tag{3.128}$$

$$\Psi(A_1^\nu) = \frac{1}{\sqrt{2}}\sum_k Z_k^\nu\Big(\hat{c}_k^\dagger\hat{c}_k - \hat{c}_{-k}^\dagger\hat{c}_{-k}\Big)\Big|0\Big\rangle. \tag{3.129}$$

where subscript k and $-k$ of the creation and annihilation operators are to identify wave vectors from K and K' point. The Eq. (3.129) and Eq. (3.129) are needed in order to construct the exciton-photon matrix element of the dipole approximation. And finally the exciton-near field matrix element.

It is worth mentioning that in the Simple Tight Binding Method, STB, taken into account in this case the curvature effect of the SWNT is neglected therefore the s and p orbital coupling is also disconsidered, in the other method, Extend Tight Binding, ETB, the curvature effect is included. The latter approach although more complex is closer to the reality than the first.

3.4.3 Exciton-photon matrix element

In this section, the formulation of the exciton-photon matrix element in the Dipole approximation is given. This work has been done by J. Jiang et al. [38] based on the second quantization. However, in this thesis, the electromagnetic field will not be quantized which means that the classical vector potential is used in the formulation. This approach has been used by A. Grünei et al. [13] to calculate the optical absorption of graphene and SWNT regarding the electron photon interaction.

Considering the Hamiltonian of an electron in an electromagnetic field

$$\mathcal{H} = \frac{[\boldsymbol{p} - e\boldsymbol{A}(\boldsymbol{r},t)]^2}{2m} + V(\boldsymbol{r}), \tag{3.130}$$

where $\boldsymbol{p}$ is linear momentum of the electron, $\boldsymbol{A}$ is vector potential of the electromag-

Fig. 3-9: fig:/exwf-swnt0800-e22go.eps

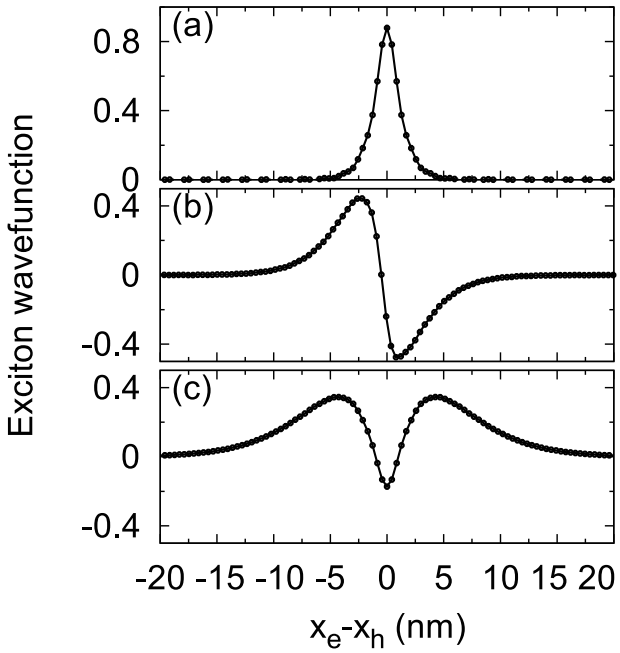

Figure 3-9: **Amplitude of A_2 exciton wavefunction for E_{22} transition as a function of relative distance along tube axis of $(8,0)$ SWNT. [24]** (a) Amplitude of the A_2 exciton wavefunction for $(\nu = 0)$. (b) Amplitude of the A_2 exciton wavefunction, $(\nu = 1)$. (c) Amplitude of the A_2 exciton wavefunction, $(\nu = 2)$.

netic field, e is the electron charge, m is its mass and $V(\boldsymbol{r})$ is the electronic potential of the electron. The linear dependence of $\boldsymbol{A}$ is retained and the squared term $\propto \boldsymbol{A}^2$, neglected, as the latter is much smaller than the former regarding the light power. The nonlinear effect can not be neglected for high energy electromagnetic field. Invoking Coulomb's gauge, $\nabla \cdot \boldsymbol{A} = 0$, the linear momentum commutes with the vector potential, then rewriting the Hamiltonian

$$\mathcal{H} = \left[\frac{\boldsymbol{p}^2}{2m} + V(\boldsymbol{r})\right] - \frac{e}{m}\boldsymbol{A}(\boldsymbol{r},t)\cdot\boldsymbol{p} = \mathcal{H}_0 + \mathcal{H}^{'}(t), \tag{3.131}$$

where $\mathcal{H}_0$ is defined as the unperturbed Hamiltonian, and $\mathcal{H}^{'}(t)$ is defined as the time-dependent perturbed Hamiltonian. Coulomb's gauge has the vector potential related to the electric field, $\boldsymbol{E} = -\frac{\partial \boldsymbol{A}}{\partial t}$, with a time-harmonic dependence $e^{-i\omega t}$ the vector potential is $\boldsymbol{A} = -\frac{i}{\omega}\boldsymbol{E}$. Therefore, the time-dependent perturbed Hamiltonian

is dependent on the electric field

$$\mathcal{H}^{'}(t) = \frac{e\hbar}{m\omega}\boldsymbol{E}(t)\cdot\nabla \tag{3.132}$$

An indispensable consideration regarding the optical perturbation, $\mathcal{H}^{'}$, over the graphene or SWNT free carriers, in the case of the far field radiation perturbation it doesn't match the free cariers wave function, of about 2nm, however in the near field perturbation scenario that is present in the 2nm distance between the tip and the sample, they are of the same order, therefore the $\boldsymbol{E}(t)$ cannot be considered constant from the dipole vector integration $\boldsymbol{D}^{fi}(\boldsymbol{k}_f,\boldsymbol{k}_i) = \left\langle \Psi^f(\boldsymbol{k}_f)\middle|\nabla|\Psi^i(\boldsymbol{k}_i)\right\rangle$, as it was done in the far field explained below.

3.4.4 Dipole vector for Graphene and for SWNT

Before going to the second quantization picture it is very constructive to calculate the Dipole Vector for two levels transition Bloch expanded wavefunctions in graphene, since a analogous fashion is to be employed for the near field Dipole Vector of SWNTs.

At first considering Bloch expanded wavefunctions, $\Psi = c_A\Phi_A + c_B\Phi_B$ and the Dipole Vector $\boldsymbol{D}^{fi}(\boldsymbol{k}_f,\boldsymbol{k}_i) = \left\langle \Psi^f(\boldsymbol{k}_f)\middle|\nabla|\Psi^i(\boldsymbol{k}_i)\right\rangle$. As the STB method is considered, only the three nearest neighbors contributions will be taken, their position is defined as, $\boldsymbol{R}_A^j = \boldsymbol{R}_B^i + \boldsymbol{r}_B^l$ for the A carbon atom position and the inverse for B, with $l = 1, 2$ and 3.

From that, the Dipole vector is obtained with the oscillator strength

$$\boldsymbol{D}^{cv}(\boldsymbol{k}) = -\frac{2\sqrt{3}m_{\text{opt}}}{a}\text{Re}\left[c_B^{c*}(\boldsymbol{k})c_A^v(\boldsymbol{k})\sum_l e^{(-i\boldsymbol{r}_A^l\cdot\boldsymbol{k})\boldsymbol{r}_A^l}\right] \tag{3.133}$$

$$m_{\text{opt}} = \left\langle \phi(\boldsymbol{r}-\boldsymbol{r}_B^1)\middle|\frac{\partial}{\partial x}\middle|\phi(\boldsymbol{r})\right\rangle \tag{3.134}$$

$$O(\boldsymbol{k}) = \sqrt{\boldsymbol{D}^{cv*}(\boldsymbol{k})\cdot\boldsymbol{D}^{cv}(\boldsymbol{k})} \tag{3.135}$$

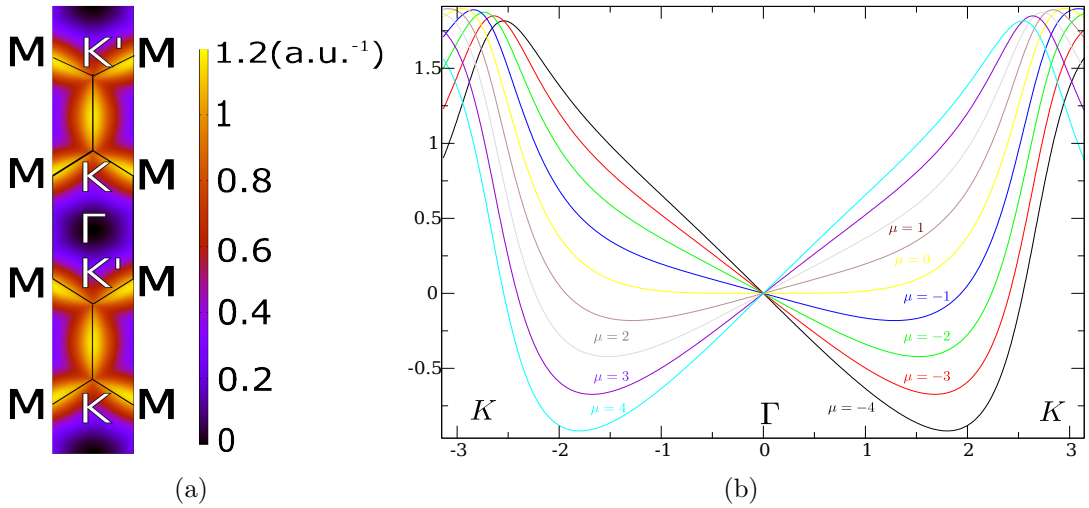

(a) (b)

Figure 3-10: (a)Oscillator strength for the dipole vector of transitions in graphene, which is a 2 dimensional material, the reason for the two components for the wave vectors, distributed on the reciprocal lattice high symmetry points [13]. A two dimensional plot, $\boldsymbol{k}_y$ by $\boldsymbol{k}_x$ and with a color range from $O(\boldsymbol{k})$. (b) Dipole vector for the SWNT armchair (5,5), one dimensional material, the reason why there is only one component for the wave vector, in each of the cutting lines index, μ. A simple two dimensional plot representation,$\boldsymbol{D}^{cv}(\boldsymbol{k})$ by $\boldsymbol{k}$.

Where $c_B^{c^*}$ and c_A^v are two coefficients for the conduction and valence bands, that arise from the STB calculation and will be discussed in detail later, as for m_{opt} this is the radiation interaction coefficient, exactly the term that is different when near field is taken into account and $O(\boldsymbol{k})$ the dipole vector absolute value, or the oscillator strength.

Under the second quantization operators are employed so that a many-particles system can be described as the linear combination of the one-particle wavefunctions which form a complete set

$$\Psi(\boldsymbol{r},t) = \sum_k \hat{c}_k(t)\psi_k(\boldsymbol{r}), \tag{3.136}$$

Fig. 3-10(a): fig:/osc-strengh.eps
Fig. 3-10(b): fig:/dipvec-55.eps

where $\hat{c}_k(t) = e^{-i\varepsilon_k t/\hbar}\hat{c}_k$, ε_k is one-particle energy. $\hat{c}_k$ and $\hat{c}_k^\dagger$ satisfy the anticommutation relations

$$\{\hat{c}_k, \hat{c}_{k'}^\dagger\} = \delta_{kk'}, \qquad \{\hat{c}_k, \hat{c}_{k'}\} = 0, \qquad \{\hat{c}_k^\dagger, \hat{c}_{k'}^\dagger\} = 0, \tag{3.137}$$

where $\delta_{kk'}$ is a Delta function. $\hat{c}_k$ and $\hat{c}_k^\dagger$ are the annihilation and the creation operators. $\hat{c}_k$ annihilates an electron in the state k, the operation will be zero if it either operates on the ground state or there is no electron in the state k. $\hat{c}_k^\dagger$ creates an electron in state k, the operation will be zero if and only if the state k has been already occupied by the electron. The Hamiltonian of the transition from the initial state to the final state is redefined

$$\mathcal{H}_{el-op} = \int \Psi_f \mathcal{H}' \Psi_i \mathrm{d}\boldsymbol{r}. \tag{3.138}$$

With the Eq. (3.136) and the perturbed one-particle Hamiltonian from Eq. (3.132) into Eq. (3.138), the Hamiltonian of the vertical transition $k_c = k_v$ is

$$\mathcal{H}_{el-op} = \frac{e\hbar}{m\omega} E_x \sum_k D_k \hat{c}_{k_c}^\dagger \hat{c}_{k_v}, \tag{3.139}$$

where E_x is the electric field parallel to the tube axis, in the x direction in which is constant, this is due to the wavelength of the laser light being much larger than the atomic distance in graphene based materials, the Dipole approximation, with this considered D_k is

$$D_k = \left\langle \Psi_k^c \middle| \frac{\partial}{\partial x} \middle| \Psi_k^v \right\rangle, \tag{3.140}$$

where the subscript c and v are the conduction band and the valence band, and $k_c = k_v$ for the vertical transition requirement.

The exciton-photon matrix elements M_{ex-op} for A_2^ν and A_1^ν excitons from the

dipole approximation are

$$M_{ex-op}(A^{\nu}_{2(1)}) = \langle \Psi(A^{\nu}_{2(1)}) | \mathcal{H}_{el-op} | 0 \rangle. \tag{3.141}$$

Using A^{ν}_2 and A^{ν}_1 from Eq. (3.129) and Eq. (3.129), into Eq. (3.141), the matrix elements of A excitons

$$M_{ex-op}(A^{\nu}_2) = \frac{1}{\sqrt{2}} \frac{e\hbar}{m\omega} E_x \sum_k Z^{\nu *}_k (D_k + D_{-k}), \tag{3.142}$$

$$M_{ex-op}(A^{\nu}_1) = \frac{1}{\sqrt{2}} \frac{e\hbar}{m\omega} E_x \sum_k Z^{\nu *}_k (D_k - D_{-k}). \tag{3.143}$$

Since the dipole vector dependence is the wave vector, k, which is repeated across the reciprocal space, a $-k$ is completely equivalent, just in a different region of the wave space, as a result $D_k = D_{-k}$. Therefore, the matrix element of A_1 excitons are always zero for all cutting lines, ν, and only the matrix element of A^n_2 remains

$$M_{ex-op}(A^{\nu}_2) = \sqrt{2} \frac{e\hbar}{m\omega} E_x \sum_k Z^{\nu *}_k D_k \qquad , \qquad M_{ex-op}(A^n_1) = 0. \tag{3.144}$$

It can be seen that the amplitude of the matrix element is proportional to E_x. If laser light is polarized along the tube axis, $E_x = E_0$ where E_0 is the amplitude of the laser light. Considering the laser light as a plane wave, the amplitude is $E_0 = \sqrt{\frac{I}{\varepsilon_0 c}}$ where ε_0 is the permittivity of vacuum and c is the speed of light in free space. The intensity I is the power and the focused area of the laser light.

The dipole vector D_k by one-particle wavefunctions of the valence band and the conduction band from Eq. (3.124) into Eq. (3.140). Making $M_{ex-op}(A^{\nu}_2)$

$$M_{ex-op}(A^{\nu}_2) = \sqrt{2} \frac{e\hbar}{m\omega} E_x \sum_k Z^{\nu *}_k D_k \tag{3.145}$$

All this considered, Eq. (3.144), $M_{ex-op}(A^{\nu}_2)$ can be written in terms of the A_2

exciton wavefunction Ψ_2^ν written in Eq. (3.127) by substituting the one-particle wavefunctions of the valence band and the conduction band expressed in Eq. (3.124) into the dipole vector around K and K' points. Then, the $M_{ex-op}(A_2^\nu)$ can be written in terms of Ψ_2^ν

$$M_{ex-op}(A_2^\nu) = \sqrt{2}\frac{e\hbar}{m\omega}E_x\left\{\sum_k Z_k^{\nu *}\frac{-2\sqrt{3}m_{\text{opt}}}{a}\text{Re}\left[c_B^{c^*}(k)c_A^v(k)\sum_l e^{(-i\boldsymbol{r}_A^l\cdot\boldsymbol{k})\boldsymbol{r}_A^l}\right]\right\} \tag{3.146}$$

3.5 Exciton photon near field matrix element

After the development of the usual radiation exciton photon matrix element $M_{ex-op}(A_2^\nu)$, based on the exciton dipole vector, derived analogously to the electron-photon one, the exciton-near field matrix element grounded on the exciton theory of carbon nanotube developed by J. Jiang et al. [2] and the classical near field spherical scattering from Mie's theory [1] developed earlier in this chapter. It is possible to investigate the near field exciton photon matrix element, by means of the scattered wave irradiated from the small metallic spherical approximation to the tip employed in TERS, which has only contributions from different dipole modes ($l = 1, 2, 3...$), the near field along the tube axis of a SWNT depends of its own geometry. The exciton-near field matrix element of the vertical transition is then constructed by replacing the incident electric field in the exciton-photon matrix element by the near field along the tube axis.

3.6 Near field factors

The tip spherical approximation with radius a placed at distance d above a SWNT is shown in Fig. 3-11. It is very important to distinguish initially the wavevector of the incident light defined as $\boldsymbol{q}$ to avoid the confusion with the wavevectors from

the SWNTs Brillouin zone, which are denoted by k. The incident electric field is polarized along the tube axis allowing vertical transitions along the tube axis. The scattered electric field $\boldsymbol{E}^{\mathrm{s}}$ of the dipole term ($l = 1, m = 1$) is taken only from the TM (Transverse Magnetic), where $B_r = 0$ and $E_r \neq 0$, mode which corresponds to the electronic vibration in the metallic sphere. Other index coefficients have to be summed to find the total contribution, remembering that the shape of the scattered field might be similar but it will change, since in the case of $m = 1$, $a_{11} = 0$. Therefore, the dipole $\boldsymbol{E}^{\mathrm{s}}$ has two components, in the radial direction (E_r^{s}) and in the polar angle (E_θ^{s}) written spherical coordinates

$$\boldsymbol{E}^{\mathrm{s}} = E_r^{\mathrm{s}}\hat{\boldsymbol{e}}_r + E_\theta^{\mathrm{s}}\hat{\boldsymbol{e}}_\theta, \tag{3.147}$$

where

$$E_r^{\mathrm{s}} = a_{11}\left[-\frac{i}{(qr)^3} - \frac{1}{(qr)^2}\right]e^{iqr}\sin\theta \tag{3.148}$$

$$E_\theta^{\mathrm{s}} = \frac{a_{11}}{2}\left[\frac{i}{(qr)^3} + \frac{1}{(qr)^2} - \frac{i}{qr}\right]e^{iqr}\cos\theta \tag{3.149}$$

a_{11} is the dipole scattering coefficient of TM mode by assigning $l = 1, m = 1$ in Eq. 3.97. The dimension of a_{11} is the same as the electric field, V/m. The terms proportional to $1/r^3$ of E_r^{s} and E_θ^{s} in Eq. (3.149) and converting from the spherical coordinates to the Cartesian system, $\hat{\boldsymbol{e}}_r = \sin\theta\hat{\boldsymbol{e}}_x - \cos\theta\hat{\boldsymbol{e}}_z$ and $\hat{\boldsymbol{e}}_\theta = \cos\theta\hat{\boldsymbol{e}}_x + \sin\theta\hat{\boldsymbol{e}}_z$, the near field $\boldsymbol{E}^{\mathrm{nf}}$ is dismembered in x and z directions

$$\begin{aligned}\boldsymbol{E}^{\mathrm{nf}} = &\left[-\frac{ia_{12}}{(qr)^3}\sin^2\theta + \frac{ia_{12}}{2(qr)^3}\cos^2\theta\right]\hat{\boldsymbol{e}}_x + \\ &\left[\frac{ia_{12}}{(qr)^3} + \frac{ia_{12}}{2(qr)^3}\right]\sin\theta\cos\theta\hat{\boldsymbol{e}}_z.\end{aligned} \tag{3.150}$$

Fig. 3-11: fig:/exciton-nf-system.eps

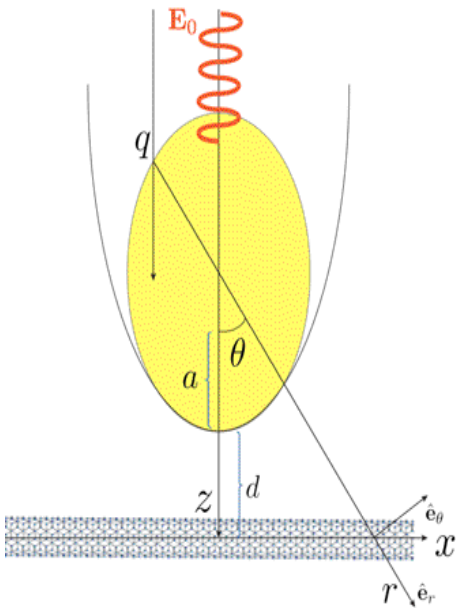

Figure 3-11: **System of a metallic sphere on SWNT.** x axis is the tube axis, and z one is perpendicular to the tube. Wave vector of an incident light is $\boldsymbol{q}$ pointing in the z direction meaning that the incident light is traveling to a SWNT from the top. The incident electric field $\boldsymbol{E}_0$ is polarized parallel to the tube axis. Radius a and separation distance d are constant parameters. The unit vectors of the spherical coordinates in the radial and polar directions are $\hat{\boldsymbol{e}}_r$ and $\hat{\boldsymbol{e}}_\theta$. r is the radial distance from the center of the metallic sphere.

With $\sin\theta = \frac{x}{r}$ and $\cos\theta = \frac{a+d}{r}$ into the near field in the x direction in Eq. (3.150), the near field along tube axis E_x^{nf}

$$E_x^{\mathrm{nf}} = \frac{ia_{11}}{2}\frac{1}{[q(a+d)]^3}\left\{\left[\frac{(a+d)^2-2x^2}{r^2}\right]\left(\frac{a+d}{r}\right)^3\right\} = \frac{ia_{11}}{2}\frac{1}{[q(a+d)]^3}f_x^{\mathrm{nf3}}(x), \tag{3.151}$$

where $f_x^{\mathrm{nf3}}(x)$ is defined as

$$f_x^{\mathrm{nf3}}(x) = \left\{\left[\frac{(a+d)^2-2x^2}{r^2}\right]\left(\frac{a+d}{r}\right)^3\right\} \tag{3.152}$$

$f_x^{\mathrm{nf3}}(x)$ is a real dimensionless function of position along the tube axis x which is maximum of 1 at $x = 0$. $f_x^{\mathrm{nf3}}(x)$ is near field function originated from $1/r^3$ terms.

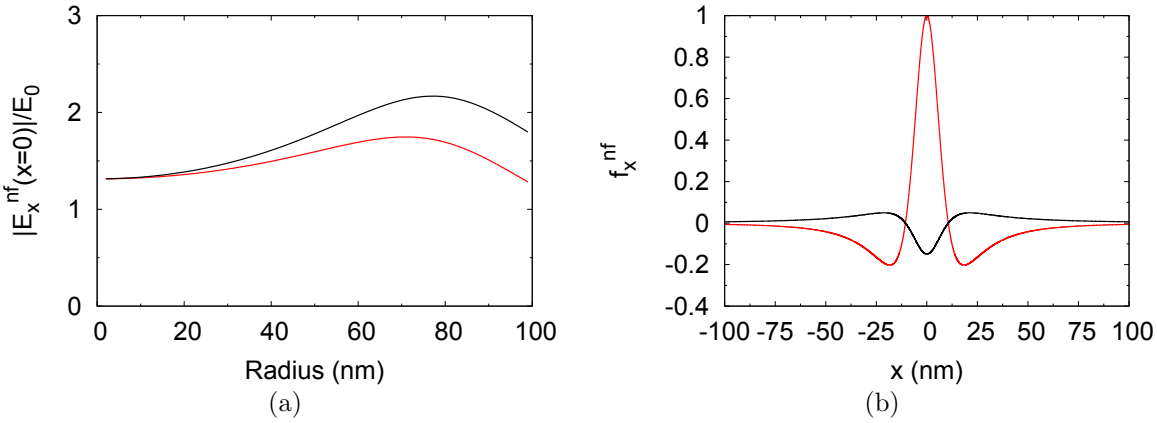

Figure 3-12: **Near field enhancement and near field functions. [24]** (a) Near field enhancement, $|E_x^{\rm nf}(x=0)|/E_0$, with only $f_x^{\rm nf3}$, the red line, or with both $f_x^{\rm nf3}$ and $f_x^{\rm nf2}$, the black line, as a function of the radius of a gold sphere excited by the He-Ne laser light with the wavelength of 633 nm. The separation distance d is zero. (b) Near field functions $f_x^{\rm nf3}$, red line, and $f_x^{\rm nf2}$, black line, dependence of the tube axis distance of a 200 nm length SWNT. The separation distance d is zero and radius of a gold sphere a is 15 nm ($a+d=15$nm).

Since $f_x^{\rm nf3}(x)$ is symmetric along the tube axis, it can be fitted with Gaussian based functions, such as $I_\alpha \exp(-\beta_\alpha x^2)$, where I_α and β_α are Gaussian fitting parameters. The Gaussian fitting function of $f_x^{\rm nf3}(x)$ will be employed in the near field matrix element.

In the right figure above it is possible to relate the range of the near field factor $1/r^3$ dependence as comparable to the exciton wave function spatial density, both are in the order of 1nm.

Considering the terms proportional to $1/r^2$ in Eq. (3.149), the total near field along the tube axis $E_x^{\rm nf}$

$$E_x^{\rm nf} = \left\{ \frac{ia_{11}}{2} \frac{1}{[q(a+d)]^3} \right\} \{ f_x^{\rm nf3}(x) + i f_x^{\rm nf2}(x) \} = \left\{ \frac{ia_{11}}{2} \frac{1}{[q(a+d)]^3} \right\} f_x^{\rm nf}(x), \quad (3.153)$$

Fig. 3-12(a): fig:/efenf-a-lam633nm.eps
Fig. 3-12(b): fig:/fxnf-15nm-xnm.eps

where $f_x^{\mathrm{nf2}}(x)$ is

$$f_x^{\mathrm{nf2}}(x) = -\frac{q(a+d)[(a+d)^2 - 2x^2]}{r^2}\left(\frac{a+d}{r}\right)^2, \tag{3.154}$$

and $f_x^{\mathrm{nf}}(x) = f_x^{\mathrm{nf3}}(x) + if_x^{\mathrm{nf2}}(x)$. $f_x^{\mathrm{nf2}}(x)$ is the near field function from the terms proportional to $1/r^2$. Adding the terms proportional to $1/r^2$ is equivalent to adding the imaginary part to $f_x^{\mathrm{nf3}}(x)$. $f_x^{\mathrm{nf2}}(x)$ is also symmetric as shown by the black line in Fig. 3-12(b). At $x = 0$, the magnitude of $f_x^{\mathrm{nf2}}(x)$ is equal to $-q(a+d)$. The near field functions $f_x^{\mathrm{nf3}}(x)$ and $f_x^{\mathrm{nf2}}(x)$ then, may be fitted with the Gaussian based functions

$$f_x^{\mathrm{nf3}}(x) = \sum_{\alpha} I_\alpha \exp\bigl(-\beta_\alpha x^2\bigr), \tag{3.155}$$

$$f_x^{\mathrm{nf2}}(x) = -q(a+d)\sum_{\alpha'} I_{\alpha'} \exp\bigl(-\beta_{\alpha'} x^2\bigr),, \tag{3.156}$$

where I_α and β_α are Gaussian fitting parameters.

3.7 The exciton photon near-field matrix element

The time-dependent perturbed Hamiltonian of one-particle as written in Eq. (3.132) is changed by including the scattered electric field $\boldsymbol{E}^{\mathrm{s}}$ to the incident electric field $\boldsymbol{E}^{\mathrm{i}}$ which is the total electric field outside a metallic sphere according to G. Mie [1]. Then, the one particle perturbed Hamiltonian of the scattered light is written in the same form as Eq. (3.132) by $\mathcal{H}^{'}(t) = \frac{e\hbar}{m\omega}\boldsymbol{E}^{\mathrm{s}}(t)\cdot\nabla$. Unlike the dipole approximation that the incident electric field is treated as constant along the tube axis [13], the scattered electric field $\boldsymbol{E}^{\mathrm{s}}$ is localized near the metallic sphere in a 2nm region, also, since the the near field component is much larger than the far field one in this region the long wavelength approximation is not valid [39], and then it can not be taken outside the integration. By following the same steps as section 2.4.3, the exciton-near

field matrix elements of A_2 and A_1 excitons for the vertical transition

$$M_{ex-nf}(A_2^\nu) = \sqrt{2}\frac{e\hbar}{m\omega}\frac{1}{2}\Sigma_k Z_k^{\nu *}\{S_k + S_{-k}\}, \tag{3.157}$$

$$M_{ex-nf}(A_1^\nu) = \sqrt{2}\frac{e\hbar}{m\omega}\frac{1}{2}\Sigma_k Z_k^{\nu *}\{S_k - S_{-k}\}, \tag{3.158}$$

where S_k is defined as the transition matrix element

$$S_k = \left\langle \Psi_k^c \middle| E_x^{\rm nf}\frac{\partial}{\partial x}\middle| \Psi_k^v \right\rangle, \tag{3.159}$$

where Ψ_k^v and Ψ_k^c are one-particle wavefunctions of valence and conduction bands, written in Eq. (3.124). By substituting the near field along the tube axis $E_x^{\rm nf}$ from Eq. (3.151) into Eq. (3.159), the transition matrix element S_k is now

$$S_k = \frac{ia_{11}}{2}\frac{1}{[q(a+d)]^3}\left\langle \Psi_k^c \middle| f_x^{\rm nf}\frac{\partial}{\partial x}\middle| \Psi_k^v \right\rangle = \frac{ia_{11}}{2}\frac{1}{[q(a+d)]^3}D_k^{\rm N}, \tag{3.160}$$

where $D_k^{\rm N}$ is defined as the near field matrix element

$$D_k^{\rm N} = \left\langle \Psi_k^c \middle| f_x^{\rm nf}(x)\frac{\partial}{\partial x}\middle| \Psi_k^v \right\rangle = \left\langle \Psi_k^c | \big(f_x^{\rm nf3}(x) + i f_x^{\rm nf2}(x)\big)\frac{\partial}{\partial x} | \Psi_k^v \right\rangle \tag{3.161}$$

The near field matrix element $D_k^{\rm N}$ has the same unit as the Dipole vector D_k. It becomes the same as D_k if and only if $f_x^{\rm nf} = 1$. Next, we show the formulation of the near field matrix element $D_k^{\rm N}$. By substituting the one-particle wavefunctions of valence and conduction bands in Eq. (3.124) into the expression of $D_k^{\rm N}$, four integrals

$$\begin{aligned} D_k^{\rm N} \;=\; & c_{\rm A}^{c*}c_{\rm A}^v\left\langle \Phi_{\rm A}^c(\boldsymbol{k},\boldsymbol{r})\middle| f_x^{\rm nf}\frac{\partial}{\partial x}\middle|\Phi_{\rm A}^v(\boldsymbol{k},\boldsymbol{r})\right\rangle + c_{\rm B}^{c*}c_{\rm B}^v\left\langle \Phi_{\rm B}^c(\boldsymbol{k},\boldsymbol{r})\middle| f_x^{\rm nf}\frac{\partial}{\partial x}\middle|\Phi_{\rm B}^v(\boldsymbol{k},\boldsymbol{r})\right\rangle + \\ & c_{\rm A}^{c*}c_{\rm B}^v\left\langle \Phi_{\rm A}^c(\boldsymbol{k},\boldsymbol{r})\middle| f_x^{\rm nf}\frac{\partial}{\partial x}\middle|\Phi_{\rm B}^v(\boldsymbol{k},\boldsymbol{r})\right\rangle + c_{\rm B}^{c*}c_{\rm A}^v\left\langle \Phi_{\rm B}^c(\boldsymbol{k},\boldsymbol{r})\middle| f_x^{\rm nf}\frac{\partial}{\partial x}\middle|\Phi_{\rm A}^v(\boldsymbol{k},\boldsymbol{r})\right\rangle \end{aligned} \tag{3.162}$$

By substituting the Bloch wave functions from Eq. (3.125) into Eq. (3.162) and taking into account only the first nearest neighbors interaction for the $_{AB}$ or $_{BA}$ terms and the interaction on the same atomic site for the $_{AA}$ or $_{BB}$ ones of Eq. (3.162). The near field matrix elements Eq. (3.162) are the summation of (A,A) and (B,B), on-site matrix elements, as well as (A,B) and (B,A), off-site matrix elements

$$\begin{aligned} D_k^{\mathrm{N}} &= \frac{1}{N} c_{\mathrm{A}}^{c*} c_{\mathrm{A}}^{v} \sum_{j=1}^{N} n_{\mathrm{AA}} + \frac{1}{N} c_{\mathrm{B}}^{c*} c_{\mathrm{B}}^{v} \sum_{j=1}^{N} n_{\mathrm{BB}} + \\ & \frac{1}{N} c_{\mathrm{A}}^{c*} c_{\mathrm{B}}^{v} \sum_{j=1}^{N} \sum_{p=1}^{3} e^{i\boldsymbol{k}\cdot\boldsymbol{r}_{\mathrm{A}}^{p}} n_{\mathrm{AB}} + \frac{1}{N} c_{\mathrm{B}}^{c*} c_{\mathrm{A}}^{v} \sum_{j=1}^{N} \sum_{p=1}^{3} e^{-i\boldsymbol{k}\cdot\boldsymbol{r}_{\mathrm{A}}^{p}} n_{\mathrm{BA}}, \end{aligned} \tag{3.163}$$

where n_{AA} and n_{BB} are called the (A,A) and (B,B) on-site matrix elements, n_{AB} and n_{BA} are called (A,B) and (B,A) off-site matrix elements, $\boldsymbol{r}_{\mathrm{A}}^{p}$ $(p = 1, 2, 3)$ are first nearest neighbours vectors pointing from A atom to B atom.

The (A,A) and (B,B) on-site matrix elements

$$n_{\mathrm{AA}} = \left\langle \varphi(\boldsymbol{r} - \boldsymbol{R}_{\mathrm{A}}^{j}) \middle| f_x^{\mathrm{nf3}} + i f_x^{\mathrm{nf2}} \frac{\partial}{\partial x} \middle| \varphi(\boldsymbol{r} - \boldsymbol{R}_{\mathrm{A}}^{j}) \right\rangle = n_{\mathrm{AA}}^{(3)} + i n_{\mathrm{AA}}^{(2)} \tag{3.164}$$

$$n_{\mathrm{BB}} = \left\langle \varphi(\boldsymbol{r} - \boldsymbol{R}_{\mathrm{B}}^{j}) \middle| f_x^{\mathrm{nf3}} + i f_x^{\mathrm{nf2}} \frac{\partial}{\partial x} \middle| \varphi(\boldsymbol{r} - \boldsymbol{R}_{\mathrm{B}}^{j}) \right\rangle = n_{\mathrm{BB}}^{(3)} + i n_{\mathrm{BB}}^{(2)} \tag{3.165}$$

and the (A,B) and (B,A) off-site matrix elements

$$n_{\mathrm{AB}} = \left\langle \varphi(\boldsymbol{r} - \boldsymbol{R}_{\mathrm{A}}^{j}) \middle| f_x^{\mathrm{nf3}} + i f_x^{\mathrm{nf2}} \frac{\partial}{\partial x} \middle| \varphi(\boldsymbol{r} - (\boldsymbol{R}_{\mathrm{A}}^{j} + \boldsymbol{r}_{\mathrm{A}}^{p})) \right\rangle = n_{\mathrm{AB}}^{(3)} + i n_{\mathrm{AB}}^{(2)} \tag{3.166}$$

$$n_{\mathrm{BA}} = \left\langle \varphi(\boldsymbol{r} - \boldsymbol{R}_{\mathrm{B}}^{j}) \middle| f_x^{\mathrm{nf3}} + i f_x^{\mathrm{nf2}} \frac{\partial}{\partial x} \middle| \varphi(\boldsymbol{r} - (\boldsymbol{R}_{\mathrm{B}}^{j} + \boldsymbol{r}_{\mathrm{B}}^{p})) \right\rangle = n_{\mathrm{BA}}^{(3)} + i n_{\mathrm{BA}}^{(2)} \tag{3.167}$$

where $\boldsymbol{R}_{\mathrm{A}}^{j}$ and $\boldsymbol{R}_{\mathrm{B}}^{j}$ are A and B atomic positions in the unit cell j of a graphene lattice. The superscript (3) and (2) denotes the matrix element of the near field function powers f_x^{nf3} or f_x^{nf2}. The $\boldsymbol{r}_{\mathrm{A}}^{p}$ and $\boldsymbol{r}_{\mathrm{B}}^{p}$, $(p = 1, 2, 3)$, are the position vectors for the first nearest neighbouring A and B atoms, from A to B, with the relation $\boldsymbol{r}_{\mathrm{B}}^{p} = -\boldsymbol{r}_{\mathrm{A}}^{p}$.

On site near field matrix element

In the dipole approximation, the on-site matrix elements do not contribute due to their symmetry. However, because of the presence of the tip generated near field function f_x^{nf}, the on-site matrix elements will actually contribute. The (A,A) on-site near field matrix element $n_{\mathrm{AA}}^{(3)}$ defined in Eq. (3.164)

$$n_{\mathrm{AA}}^{(3)} = \left\langle \varphi(\boldsymbol{r} - \boldsymbol{R}_{\mathrm{A}}^{j}) \middle| f_x^{\mathrm{nf3}}(x) \frac{\partial}{\partial x} \middle| \varphi(\boldsymbol{r} - \boldsymbol{R}_{\mathrm{A}}^{j}) \right\rangle \tag{3.168}$$

Employing Gaussian functions from the $2pz$ atomic orbital, f_x^{nf3} into Eq. (3.168)

$$n_{\mathrm{AA}}^{(3)} = \frac{1}{n} \sum_{k,l,\alpha} 2\beta_l I_l I_k I_\alpha \{L_x\}\{L_y\}\{L_z\}, \tag{3.169}$$

where the indexes k and l are for the $2pz$ atomic orbital, and the index α is for the near field function. The integrals L_x, L_y and L_z

$$L_x = -\int_{-\infty}^{\infty} (x - x_{\mathrm{A}}^{j}) e^{\left[-\gamma_{kl}(x - x_{\mathrm{A}}^{j})^2 - \beta_\alpha x^2\right]} \mathrm{d}x, \tag{3.170}$$

$$L_y = \int_{-\infty}^{\infty} e^{\left[-\gamma_{kl}\left(y - y_{\mathrm{A}}^{j}\right)^2\right]} \mathrm{d}y, \tag{3.171}$$

$$L_z = \int_{-\infty}^{\infty} z^2 e^{\left(-\gamma_{kl} z^2\right)} \mathrm{d}z, \tag{3.172}$$

where $\gamma_{kl} = \beta_k + \beta_l$, x_{A}^{j} and y_{A}^{j} are the components for the A atom position in the graphene lattice j. L_y and L_z can be integrated straightforwardly as any Gaussian integral. Then, $L_y = \sqrt{\frac{\pi}{\gamma_{kl}}}$, and $L_z = \sqrt{\frac{\pi}{\gamma_{kl}}}\left(\frac{1}{2\gamma_{kl}}\right)$. As for L_x, the exponential term of Eq. (3.170) is expanded

$$e^{\left[-\gamma_{kl}(x - x_{\mathrm{A}}^{j})^2 - \beta_\alpha x^2\right]} = e^{\left[-\frac{\gamma_{kl}\beta_\alpha}{\gamma_{kl}+\beta_\alpha}\left(x_{\mathrm{A}}^{j}\right)^2\right]} e^{\left[-(\gamma_{kl}+\beta_\alpha)(x - x_0)^2\right]} \tag{3.173}$$

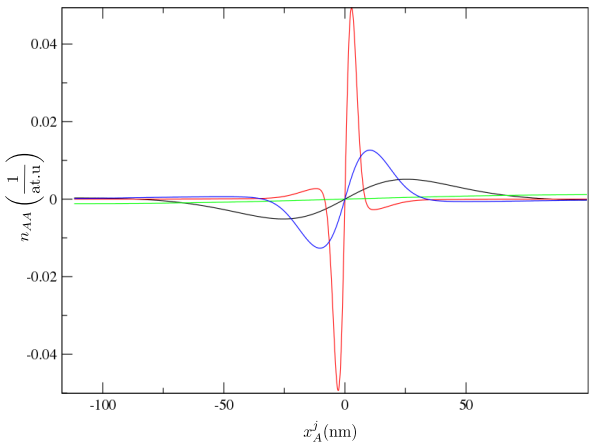

Figure 3-13: **(A,A) on-site matrix element n_{AA} as a function of x_{A}^j.** Red line is n_{AA} for $a+d=1$ nm, blue line for $a+d=4$ nm, black for $a+d=10$ and green for $a+d=44$ nm.

where $x_0=\frac{\gamma_{kl}}{\gamma_{kl}+\beta_\alpha}x_{\mathrm{A}}^j$. Then L_x can be integrated analytically as the previous Gaussians, L_y and L_z

$$L_x = x_{\mathrm{A}}^j \frac{\beta_\alpha}{\gamma_{kl}+\beta_\alpha}\sqrt{\frac{\pi}{\gamma_{kl}+\beta_\alpha}}e^{\left[-\frac{\gamma_{kl}\beta_\alpha}{\gamma_{kl}+\beta_\alpha}(x_{\mathrm{A}}^j)^2\right]} \tag{3.174}$$

By substituting L_x, L_y and L_z into Eq. (3.169), the $n_{\mathrm{AA}}^{(3)}$ can be expressed as

$$n_{\mathrm{AA}}^{(3)}(x_{\mathrm{A}}^j) = x_{\mathrm{A}}^j \frac{1}{n}\sum_{k,l,\alpha}\beta_\alpha\beta_l I_l I_k I_\alpha \frac{1}{\gamma^2}\left(\frac{\pi}{\gamma_{kl}+\beta_\alpha}\right)^{3/2} e^{\left[-\frac{\gamma_{kl}\beta_\alpha}{\gamma_{kl}+\beta_\alpha}(x_{\mathrm{A}}^j)^2\right]} \tag{3.175}$$

The (B,B) on-site matrix element $n_{\mathrm{BB}}^{(3)}$ is analogous to the previous result on 3.175. The same goes for $n_{\mathrm{AA}}^{(2)}$ and $n_{\mathrm{BB}}^{(2)}$, the only difference between $n_{\mathrm{BB}}^{(3)}$ and $n_{\mathrm{AA}}^{(2)}$ is their magnitude. The on-site matrix elements have an exponential dependence of the component of the atom component x_{A}^j is originated from the localization of the near field. $n_{\mathrm{AA}}^{(3)}(n_{\mathrm{BB}}^{(3)})$ is proportional to $x_{\mathrm{A}}^j(x_{\mathrm{B}}^j)$ due to the symmetry. If $x_{\mathrm{A}}^j(x_{\mathrm{B}}^j)$ is equal to zero, the near field on-site matrix element is maximum. In Fig. 3-13, $n_{\mathrm{AA}}^{(3)}$ as a function of x_{A}^j has been shown for $a+d=1,4,10,44$ nm with $d=0$nm. The red curve from $a+d=1$ peaks at 0.05 1/(at.u) with $x_{\mathrm{A}}^j=0.38$ nm. $n_{\mathrm{AA}}^{(3)}$ sharply decreases

Fig. 3-13: fig:/nAA.eps

by increasing the $x_{\rm A}^j$. By increasing $a+d$, $n_{\rm AA}^{(3)}$ is broadened and the its amplitude decreases resulting in an anti-symmetric on-site matrix element.

Off site near field matrix element

Only $n_{\rm AB}$ will be calculated in detail since $n_{\rm BA}$ is completely analogous to it. According to Eq. (3.166), $n_{\rm AB}^{(3)}$ is

$$n_{\rm AB}^{(3)} = \left\langle \varphi(\boldsymbol{r}-\boldsymbol{R}_{\rm A}^j)\middle| f_x^{\rm nf3}(x)\frac{\partial}{\partial x}\middle|\varphi(\boldsymbol{r}-(\boldsymbol{R}_{\rm A}^j+\boldsymbol{r}_{\rm A}^{\,p}))\right\rangle. \tag{3.176}$$

The A carbon atom from the unrolled graphene sheet position vector is $\boldsymbol{R}_{\rm A}^j = x_{\rm A}^j\hat{\boldsymbol{e}}_x + y_{\rm A}^j\hat{\boldsymbol{e}}_y$ where $x_{\rm A}^j$ and $y_{\rm A}^j$ are its components on the tube axis and on its circumference. Three first nearest neighbor position vectors are pointing out from $\boldsymbol{R}_{\rm A}^j$, $\boldsymbol{r}_{\rm A}^{\,p} = x_{\rm rA}^p\hat{\boldsymbol{e}}_x + y_{\rm rA}^p\hat{\boldsymbol{e}}_y$. Employing the Gaussian based functions from the $2pz$ atomic orbital as well as the near field function $f_x^{\rm nf3}$ into Eq. (3.176), $n_{\rm AB}^{(3)}$ is now

$$n_{\rm AB}^{(3)} = \frac{1}{n}\sum_{k,l,\alpha} 2\beta_l I_l I_k I_\alpha \{L_x\}\{L_y\}\{L_z\}, \tag{3.177}$$

where the indexes k and l are for the $2pz$ atomic orbital, and the index α is for the near field function. The integrals L_x, L_y and L_z are

$$L_x = -\int_{-\infty}^{\infty}\left[x-(x_{\rm A}^j+x_{\rm rA}^p)\right]e^{\left[-\beta_k(x-x_{\rm A}^j)^2-\beta_l\left(x-(x_{\rm A}^j+x_{\rm rA}^p)\right)^2-\beta_\alpha x^2\right]}{\rm d}x \tag{3.178}$$

$$L_y = \int_{-\infty}^{\infty} e^{\left[-\beta_k\left(y-y_{\rm A}^j\right)^2-\beta_l\left(y-(y_{\rm A}^j+y_{\rm rA}^p)\right)^2\right]}{\rm d}y \tag{3.179}$$

$$L_z = \int_{-\infty}^{\infty} z^2 e^{\left(-\gamma_{kl}z^2\right)}{\rm d}z \tag{3.180}$$

where $\gamma_{kl} = \beta_k + \beta_l$. The $z-$integral (L_z) is the same as in the near field on-site matrix element, $L_z = \sqrt{\frac{\pi}{\gamma_{kl}}}\left(\frac{1}{2\gamma_{kl}}\right)$. Not the case for L_y and L_y. In order to perform

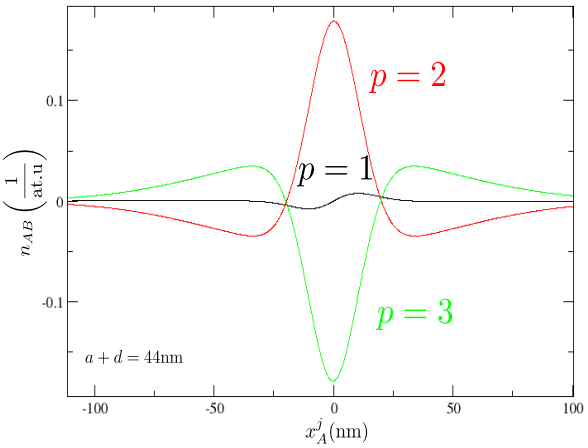

Figure 3-14: **The near field (A,B) off-site matrix element as a function of $x_{\rm A}^j$.** Here each nearest neighbor gives one of the curves, which are in turn summed over so the off site element is obtained. The wavelength of the laser light is 633 nm. The component of the first nearest neighbor vector on the tube axis is $x_{\rm rA}^3 = -a_{\rm c-c}$, where $a_{\rm c-c} = 0.142$ nm, C-C atomic distance.

the integration, each exponential term will be expanded by

$$e^{\left[-\beta_k(x-x_a)^2-\beta_l(x-x_b)^2-\beta_\alpha(x-x_c)^2\right]} = C_{kl\alpha}e^{\left[-(\gamma_{kl}+\beta_\alpha)(x-x_0)^2\right]} \tag{3.181}$$

where $C_{kl\alpha}(x_a, x_b, x_c)$ and x_0 are

$$C_{kl\alpha} = e^{\left[-\frac{\beta_k\beta_l}{\gamma_{kl}+\beta_\alpha}(x_a-x_b)^2-\frac{\beta_k\beta_\alpha}{\gamma_{kl}+\beta_\alpha}(x_a-x_c)^2-\frac{\beta_l\beta_\alpha}{\gamma_{kl}+\beta_\alpha}(x_b-x_c)^2\right]} \tag{3.182}$$

$$x_0 = \frac{\beta_k x_a + \beta_l x_b + \beta_\alpha x_c}{\gamma_{kl}+\beta_\alpha}. \tag{3.183}$$

Then, L_x and L_y can be expanded and integrated as previous Gaussians functions

$$L_x(x_{\rm A}^j, x_{\rm rA}^p) = C_{kl\alpha}\left(\frac{1}{\gamma_{kl}+\beta_\alpha}\right)\sqrt{\frac{\pi}{\gamma_{kl}+\beta_\alpha}}\left[\beta_\alpha x_{\rm A}^j + (\beta_k+\beta_\alpha)x_{\rm rA}^p\right], \tag{3.184}$$

$$L_y(y_{\rm rA}^p) = \sqrt{\frac{\pi}{\gamma_{kl}}}\exp\left[-\frac{\beta_k\beta_l}{\gamma_{kl}}(y_{\rm rA}^p)^2\right] \tag{3.185}$$

By replacing the integrals with the results from earlier, $n_{\rm AB}^{(3)}$ is

$$n^{(3)}_{\rm AB}(x^j_{\rm A}, x^p_{\rm rA}) = \frac{1}{n}\sum_{k,l,\alpha}\beta_l I_l I_k I_\alpha \frac{1}{\gamma^2_{kl}}\left(\frac{\pi}{\gamma_{kl}+\beta_\alpha}\right)^{3/2}\left[\beta_\alpha x^j_{\rm A} + (\beta_k+\beta_\alpha)x^p_{\rm rA}\right] e^{\left[-\frac{\beta_k\beta_l}{\gamma_{kl}+\beta_\alpha}(a_{\rm c-c})^2 - \frac{\beta_k\beta_\alpha}{\gamma_{kl}+\beta_\alpha}(x^j_{\rm A})^2 - \frac{\beta_l\beta_\alpha}{\gamma_{kl}+\beta_\alpha}(x^j_{\rm A}+x^p_{\rm rA})^2\right]} \tag{3.186}$$

Similarly, $n^{(2)}_{\rm AB}$ defined in Eq. (3.166)

$$n^{(2)}_{\rm AB}(x^j_{\rm A}, x^p_{\rm rA}) = -q(a+d)\frac{1}{n}\sum_{k,l,\alpha'}\beta_l I_l I_k I_{\alpha'} \frac{1}{\gamma^2_{kl}}\left(\frac{\pi}{\gamma_{kl}+\beta_{\alpha'}}\right)^{3/2}\left[\beta_{\alpha'} x^j_{\rm A} + (\beta_k+\beta_{\alpha'})x^p_{\rm rA}\right] e^{\left[-\frac{\beta_k\beta_l}{\gamma_{kl}+\beta_{\alpha'}}(a_{\rm c-c})^2 - \frac{\beta_k\beta_{\alpha'}}{\gamma_{kl}+\beta_{\alpha'}}(x^j_{\rm A})^2 - \frac{\beta_l\beta_{\alpha'}}{\gamma_{kl}+\beta_{\alpha'}}(x^j_{\rm A}+x^p_{\rm rA})^2\right]} \tag{3.187}$$

In Eq. (3.186) there is a correspondence relation to the far field dipole approximation, when $\beta_\alpha = 0$, $I_\alpha = 1$, and without summation on α, which means that $f^{\rm nf}_x = 1$. The exponential decay of $n_{\rm AB}$ is due to the localization of the near field. In Fig. 3-14, the magnitude of the $n^{(3)}_{\rm AB}$ (solid red line) as a function of $x^j_{\rm A}$ for the first nearest neighbor $\boldsymbol{r}^3_{\rm A}$ of a zigzag SWNT from which the component on the tube axis, $x^3_{\rm rA}$, is $-a_{\rm c-c}$, where $a_{\rm c-c} = 0.142$ nm, C-C atomic distance. The radius of a gold sphere is $a = 15$ nm, and the separation distance $d = 0$ nm. Then, the FWHM of the near field function $f^{\rm nf3}_x$ is about 11.5 nm. The wavelength of the laser light is 633 nm. It can be seen that the FWHM of the $n^{(3)}_{\rm AB}$ is the same as that of the near field function $f^{\rm nf3}_x$. Therefore, the enhancement of near field matrix element is only inside the region enclosed by the full width at half maximum, FWHM of near field function. The magnitude of near field matrix element becomes much smaller than that of the far field matrix element outside this region. The magnitude of the $n^{(3)}_{\rm AB}$ doesn't have much difference as the $n_{\rm AB}$ by including the $n^{(2)}_{\rm AB}$.Note that the relation $n_{\rm AB}(x^j_{\rm A}, -x^p_{\rm rA}) = -n_{\rm AB}(x^j_{\rm A}, x^p_{\rm rA})$ is always satisfied.

Fig. 3-14: fig:/nAB.eps

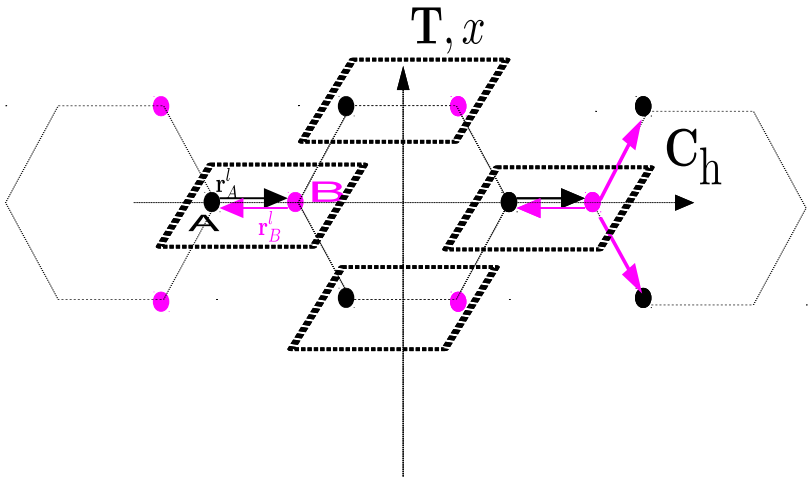

Figure 3-15: **Coordinate and first nearest neighbor vectors in an unrolled graphene lattice of an armchair SWNT.** Coordinate system for an armchair SWNT, the origin is at the center of the central hexagon, and the tube axis as well as the circumference one are in the $\boldsymbol{T}$ and $\boldsymbol{C}_h$ directions.The unit cells of this graphene lattice are marked by the dotted parallelograms. Distinct carbon atoms A and B in graphene unit cell are the black and magenta filled circles.

3.8 Exciton-photon near field element for achiral SWNT

The development of the exciton photon interactions matrix elements for achiral SWNT is made, since there is no angle dependence as in the chiral case, this is the simplest development.

3.8.1 Armchair SWNT near field exciton-photon matrix element

Fig. 3-15: fig:/armchair-swnt.eps

Three nearest neighbor vectors in the above figure

$$\boldsymbol{r}_{\rm A}^{1} = \left(\frac{a_0}{C_h}\right)\boldsymbol{C}_h \tag{3.188}$$

$$\boldsymbol{r}_{\rm A}^{2} = -\left(\frac{a_0/2}{C_h}\right)\boldsymbol{C}_h + \left(\frac{\sqrt{3}a_0/2}{T}\boldsymbol{T}\right) \tag{3.189}$$

$$\boldsymbol{r}_{\rm A}^{3} = -\left(\frac{a_0/2}{C_h}\right)\boldsymbol{C}_h - \left(\frac{\sqrt{3}a_0/2}{T}\boldsymbol{T}\right) \tag{3.190}$$

where $a_0 = 0.142$ nm is C-C distance.

The origin is strategically defined in the unrolled graphene sheet of an armchair SWNT at the intersection between the z'-axis or $\theta = 0$ axis of the metallic spherical approximation in Fig. 3-11 as shown in Fig. 3-15. Since D_k^N in Eq. (3.160) is in the reciprocal space of armchair SWNTs, the wavevector k is translatable over the reciprocal space, $D_k^N = D_{-k}^N$. Then, the exciton-photon near field matrix element of A_1 excitons are null for all ν, as for the A_2 excitons this is not the case, S_k from Eq. (3.160) into $M_{\rm ex-nf}(A_2^\nu)$ in Eq. (3.157) results in

$$M_{\rm ex-nf}(A_2^\nu) = \sqrt{2}\frac{e\hbar}{m\omega}\left\{\frac{ia_{12}}{2}\frac{1}{[q(a+d)]^3}\right\}\sum_k Z_k^{\nu *} D_k^N. \tag{3.191}$$

The remaining part of this matrix element to be evaluated is the summation $\sum_k Z_k^{\nu *} D_k^N$ in Eq. (3.191) for armchair SWNTs. The D_k^N in Eq. (3.162) will be considered for an armchair SWNT. The coefficients of the one-particle wavefunctions from the valence and the conduction bands for A and B atoms are taken from the STB method from [13]

$$c_{\rm A}^v(\boldsymbol{k}) = \frac{1}{\sqrt{2(1+sw(\boldsymbol{k}))}}\sqrt{\frac{f(\boldsymbol{k})}{w(\boldsymbol{k})}}, \quad c_{\rm B}^v(\boldsymbol{k}) = \frac{1}{\sqrt{2(1+sw(\boldsymbol{k}))}}\sqrt{\frac{f^*(\boldsymbol{k})}{w(\boldsymbol{k})}}, \tag{3.192}$$

$$c_{\rm A}^c(\boldsymbol{k}) = \frac{1}{\sqrt{2(1-sw(\boldsymbol{k}))}}\sqrt{\frac{f(\boldsymbol{k})}{w(\boldsymbol{k})}}, \quad c_{\rm B}^c(\boldsymbol{k}) = -\frac{1}{\sqrt{2(1-sw(\boldsymbol{k}))}}\sqrt{\frac{f^*(\boldsymbol{k})}{w(\boldsymbol{k})}}, \tag{3.193}$$

where s is the overlap integral, $f(\boldsymbol{k}) = \sum_{p=1}^{3}\exp(i\boldsymbol{k}\cdot\boldsymbol{r}_{\rm A}^p)$, and $w(\boldsymbol{k}) = |f(\boldsymbol{k})|$. Con-

sidering the valence band, the coefficients must be taken complex conjugate if atomic sites are changed from A atom to B atom and vice versa. As for the conduction band its coefficients go negative complex conjugate if the same exchange is made. The product of the coefficients for the near field (A,A) and (B,B) on-site matrix elements satisfy the relation $c_{\mathrm{A}}^{c*}(\boldsymbol{k})c_{\mathrm{A}}^{v}(\boldsymbol{k}) = -c_{\mathrm{B}}^{c*}(\boldsymbol{k})c_{\mathrm{B}}^{v}(\boldsymbol{k})$. Furthermore, $n_{\mathrm{AA}} = n_{\mathrm{BB}}$, since $x_{\mathrm{A}}^{j} = x_{\mathrm{B}}^{j}$, this is due to the armchair geometry at place. Therefore, there is no contribution to the near field on-site matrix elements of armchair SWNTs . Then, D_k^N for armchair is

$$\begin{aligned} D_k^{\mathrm{N}} &= \frac{1}{N}c_{\mathrm{A}}^{c*}(\boldsymbol{k})c_{\mathrm{B}}^{v}(\boldsymbol{k})\sum_{j=1}^{N}\sum_{p=1}^{3} e^{i\boldsymbol{k}\cdot\boldsymbol{r}_{\mathrm{A}}^{p}} n_{\mathrm{AB}}\big(x_{\mathrm{A}}^{j}, x_{\mathrm{rA}}^{p}\big) + \\ &\quad \frac{1}{N}c_{\mathrm{B}}^{c*}(\boldsymbol{k})c_{\mathrm{A}}^{v}(\boldsymbol{k})\sum_{j=1}^{N}\sum_{p=1}^{3} e^{-i\boldsymbol{k}\cdot\boldsymbol{r}_{\mathrm{A}}^{p}} n_{\mathrm{BA}}\big(x_{\mathrm{A}}^{j}, -x_{\mathrm{rA}}^{p}\big). \end{aligned} \tag{3.194}$$

D_k^N can be expanded by summing on p. Then, D_k^N can be written in term of the summation of $n_{\mathrm{AB}}\big(x_{\mathrm{A}}^{j}, x_{\mathrm{rA}}^{2}\big)$ on j multiplied by k dependent function as

$$D_k^{\mathrm{N}} = \frac{1}{N}\left\{\sum_{j=1}^{N} n_{\mathrm{AB}}(x_{\mathrm{A}}^{j}, x_{\mathrm{rA}}^{2})\right\}\{c_{\mathrm{A}}^{c*}(\boldsymbol{k})c_{\mathrm{B}}^{v}(\boldsymbol{k})\phi(\boldsymbol{k}) - c_{\mathrm{B}}^{c*}(\boldsymbol{k})c_{\mathrm{A}}^{v}(\boldsymbol{k})\phi^{*}(\boldsymbol{k})\}, \tag{3.195}$$

where $\phi(\boldsymbol{k}) = e^{(i\boldsymbol{k}\cdot\boldsymbol{r}_{\mathrm{rA}}^{2})} - e^{(i\boldsymbol{k}\cdot\boldsymbol{r}_{\mathrm{rA}}^{3})}$. Using the nearest neighbours position vectors$\boldsymbol{r}_{\mathrm{rA}}^{2}$ and $\boldsymbol{r}_{\mathrm{rA}}^{3}$ as shown in Fig. 3-15 to $\phi(\boldsymbol{k})$, the phase factor

$$\phi(\boldsymbol{k}) = 2i\sin\left(\frac{ka}{2}\right)\exp\left(-i\frac{\mu\pi a}{C_h\sqrt{3}}\right), \tag{3.196}$$

where k is the wavenumber along the tube axis, μ is the cutting line index, $a = \sqrt{3}a_{c-c} = 0.246$ nm is graphene lattice constant, and C_h is the circumference direction

vector of the SWNT. Then, the summation $\sum_k Z_k^{\nu *} D_k^N$

$$\sum_k Z_k^{\nu *} D_k^N = \frac{1}{N}\left\{\sum_{j=1}^{N} n_{\rm AB}(x_{\rm A}^j, x_{\rm rA}^2)\right\} \left\{\sum_k Z_k^{\nu *}[c_{\rm A}^{c*}(\boldsymbol{k}) c_{\rm B}^v(\boldsymbol{k})\phi(\boldsymbol{k}) - c_{\rm B}^{c*}(\boldsymbol{k}) c_{\rm A}^v(\boldsymbol{k})\phi^*(\boldsymbol{k})]\right\}. \quad (3.197)$$

The normalization constant $1/N$, where N is the total number of graphene lattices in a SWNT, present in Eq. (3.197) since $n_{\rm AB}$ is not a constant of $x_{\rm A}^j$, instead it exponentially decays by increasing $x_{\rm A}^j$ as shown in Fig. 3-14. Therefore increasing the number of graphene unit cells N in a SWNT, the number of wavenumbers k along the tube axis also increases. The increasing of the number of k raises the term summation on k in Eq. (3.197). However, the factor $1/N$ strongly reduces $\sum_{j=1}^{N} n_{\rm AB}(x_{\rm A}^j, x_{\rm rA}^2)$. Then, $\sum_k Z_k^{\nu *} D_k^N$ decreases by increasing N. Therefore, the exciton-near field matrix element would vanish by increasing the length of a SWNT, if all $x_{\rm A}^j$ were taken into account.

3.8.2 Zigzag SWNT near field exciton-photon matrix element

Zigzag SWNT geometry depicted in Fig. 3-16 as well as the nearest neighboring position vectors . The origin is again strategically defined at the center of the hexagon where a line perpendicular to the tube axis passes through the origin of the metallic tip spherical approximation.

Fig. 3-16: fig:/zigzag-swnt.eps

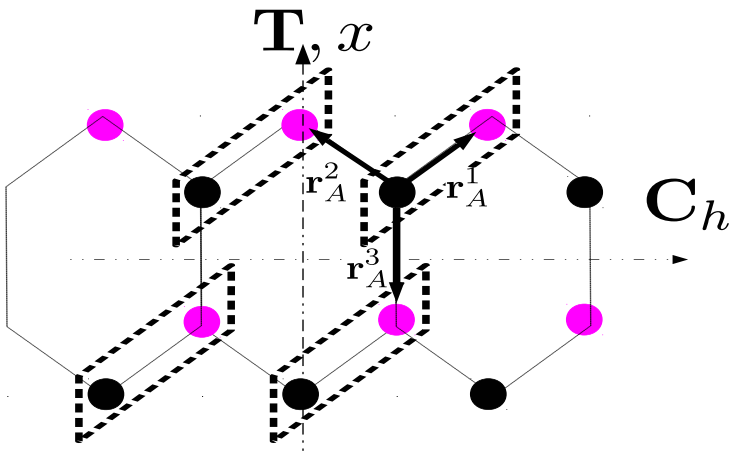

Figure 3-16: **Coordinate and first nearest neighbor vectors in an unrolled graphene lattice of zigzag SWNT.** Coordinate system of a zigzag SWNT, the origin is at the center of the central hexagon, and tube axis and circumference are in the $\mathbf{T}$ and in the $\mathbf{C}_h$ directions. Graphene unit cells are the dashed parallelograms. Two distinct carbon atoms A and B in the graphene unit cell are the black and magenta full circles.

Three first nearest neighbor position vectors for the zigzag SWNT

$$\boldsymbol{r}_{\mathrm{A}}^1 = \sqrt{3}a_0/2\left(\frac{\boldsymbol{C}_h}{C_h}\right) + a_0/2\left(\frac{\boldsymbol{T}}{T}\right) \tag{3.198}$$

$$\boldsymbol{r}_{\mathrm{A}}^2 = -\sqrt{3}a_0/2\left(\frac{\boldsymbol{C}_h}{C_h}\right) + a_0/2\left(\frac{\boldsymbol{T}}{T}\right) \tag{3.199}$$

$$\boldsymbol{r}_{\mathrm{A}}^3 = -a_0\left(\frac{\boldsymbol{T}}{T}\right) \tag{3.200}$$

where $a_0 = 0.142$ nm is C-C distance.

According to the coordinate system of the zigzag SWNT, A and B atoms in graphene unit cell j have distinct positions on the tube axis, $x_{\mathrm{A}}^j \neq x_{\mathrm{B}}^j$. Differently from the armchair SWNT, the summation $\sum_k Z_k^{\nu *} D_k^N$ cannot be simplified.

$$\sum_k Z_k^{\nu *} D_k^N = \frac{1}{N}\sum_{j=1}^{N}\sum_k\sum_{p=1}^{3} Z_k^{\nu *}\Big[c_{\mathrm{A}}^{c*}(\boldsymbol{k})c_{\mathrm{B}}^{v}(\boldsymbol{k})e^{i\boldsymbol{k}\cdot\boldsymbol{r}_{\mathrm{A}}^p} n_{\mathrm{AB}}(x_{\mathrm{A}}^j, x_{\mathrm{A}}^p) + c_{\mathrm{B}}^{c*}(\boldsymbol{k})c_{\mathrm{A}}^{v}(\boldsymbol{k})e^{-i\boldsymbol{k}\cdot\boldsymbol{r}_{\mathrm{A}}^p} n_{\mathrm{BA}}(x_{\mathrm{B}}^j, -x_{\mathrm{A}}^p)\Big], \tag{3.201}$$

where the exponential phase factor of the three nearest neighbours are

$$e^{(i\boldsymbol{k}\cdot\boldsymbol{r}_{\mathrm{A}}^{1})} = e^{\left[i\frac{a}{2}\frac{\mu}{d_t/2}+\frac{ika}{2\sqrt{3}}\right]} \tag{3.202}$$

$$e^{(i\boldsymbol{k}\cdot\boldsymbol{r}_{\mathrm{A}}^{2})} = e^{\left[-i\frac{a}{2}\frac{\mu}{d_t/2}+\frac{ika}{2\sqrt{3}}\right]} \tag{3.203}$$

$$e^{(i\boldsymbol{k}\cdot\boldsymbol{r}_{\mathrm{A}}^{3})} = e^{\left[-\frac{ika}{\sqrt{3}}\right]} \tag{3.204}$$

The exciton-photon near field matrix element has smaller value than the exciton-photon far field matrix element if all graphene lattices of the unrolled carbon nanotube are taken into account.

Chapter 4

Results and Discussions

After the introduction and listing of all the components related to the tip enhancement Raman spectroscopy, that have been explained in ever increasing level of detailed in chapters 2 and 3, it is now possible to present and discuss the main results that were obtained for some armchair SWNTs taking into account the near field generated by the metallic tip spherical approximation interaction with bright excitons generated in these SWTNs.

4.1 Tip enhanced Raman intensity formulation

The usual Raman intensity discussed in chapter 2 last section contained non near field components exciton radiation interactions matrix elements, considering the final results of chapter 3, the near field matrix elements, it can be rewritten

$$I(\omega_q, E_{\text{laser}}) = \sum_f \left| \sum_{m,m'} \frac{M_{\text{ex-nf}}(\mathbf{k}-\mathbf{q}, im') M^{\text{ep}}(\mathbf{q}, m'm) M_{\text{ex-nf}}(\mathbf{k}, im)}{(E_{\text{laser}} - \Delta E_{mi})(E_{\text{laser}} - \hbar\omega_q - \Delta E_{m'i})} \right|^2 \tag{4.1}$$

A program was developed to calculate this intensity by the Raman shift, the difference between the incident and the scattered light wavelength, by Hasdeo *et al.*

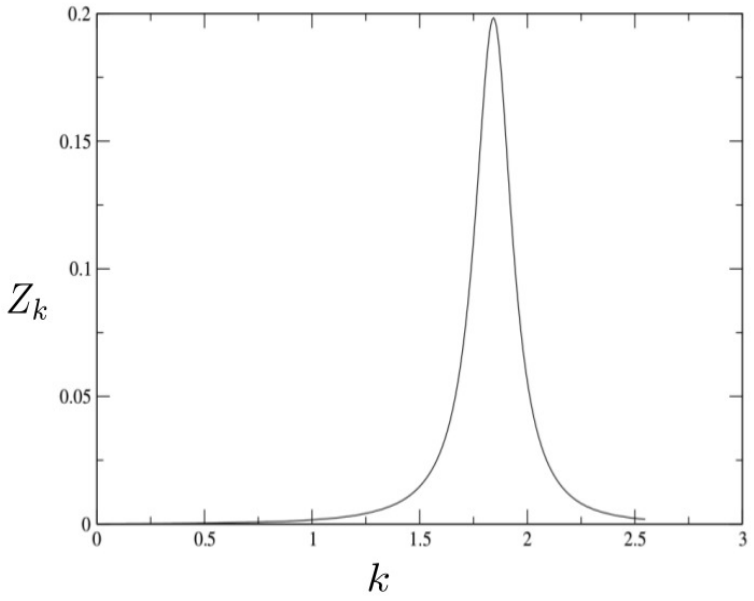

Figure 4-1: Wavefunction for a E_{22} transition exciton in a armchair (5,5) SWNT, the amplitude Z_k by the wavevector k

[40]. Yet this program did not include the final result from the previous chapter, the near field exciton matrix element, $M_{\text{ex-nf}}$.

$$M_{\text{ex}-\text{nf}}(A_2^{\nu}) = \sqrt{2}\frac{e\hbar}{m\omega}\left\{\frac{ia_{12}}{2}\frac{1}{[q(a+d)]^3}\right\}\sum_k Z_k^{\nu *} D_k^N. \tag{4.2}$$

The same was done to calculate this matrix element, but in order to do so, the numerical solution of the Bethe Salpeter equation

$$\sum_{\boldsymbol{k}_c\boldsymbol{k}_v}\left\{[E(\boldsymbol{k}_c) - E(\boldsymbol{k}_v)]\delta_{\boldsymbol{k}'_c\boldsymbol{k}_c}\delta_{\boldsymbol{k}'_v\boldsymbol{k}_v} + K(\boldsymbol{k}'_c\boldsymbol{k}'_v, \boldsymbol{k}_c\boldsymbol{k}_v)\right\}\Psi^n(\boldsymbol{k}_c\boldsymbol{k}_v) = \Omega^n\Psi^n(\boldsymbol{k}'_c\boldsymbol{k}'_v) \tag{4.3}$$

was obtained by using a program developed by Nugraha *et al.* [14], the results from this program consist of the exciton wavefunction of each carbon nanotube chirality for each corresponding dielectric constant and cutting line

Fig. 4-1: fig:/0505e22wf.eps

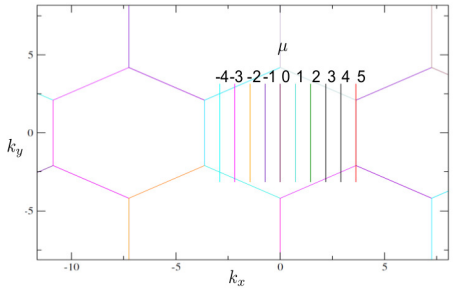

Figure 4-2: (5,5) SWNT Brillouin zone with the cutting line index μ, remembering that the E_{22} transition corresponds to $\mu = 3$, since it is the second line crossing the line connecting two M points, from different hexagons.

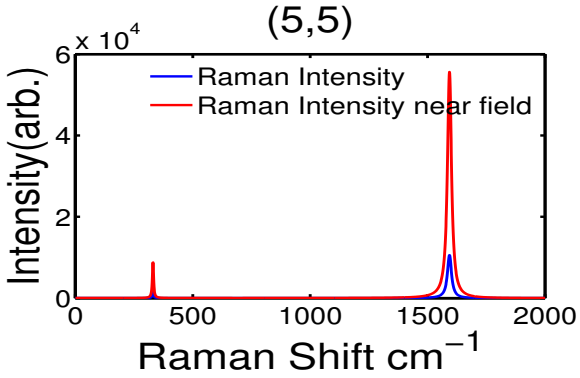

Figure 4-3: (5,5) Raman intensity with and without the near field matrix element, where for this case $|M_{\text{ex-nf}}| = 0.2612$eV, the gold tip apex spherical approximation radius of 40nm, from which the sample is 4nm distant and the incident laser energy $E_{\text{laser}} = 3.39$eV.

Since the E_{22} transition exciton was the one considered for the whole thesis calculation, as explained in chapter 3 exciton theory section 3.4, this transition is proportional to k vectors that correspond to a specific portion of the SWNT Brillouin zone.

From this it is finally possible to calculate the exciton near field matrix element that is going to be used in Hasdeo's program [40] . Finally obtaining a (5,5) SWNT Raman spectra.

The first peak from the above figure Fig.4-3 corresponds to the Radial Breathing

Fig. 4-2: fig:/swnt0505bzcut.eps
Fig. 4-3: fig:/0505ramanintensity.eps

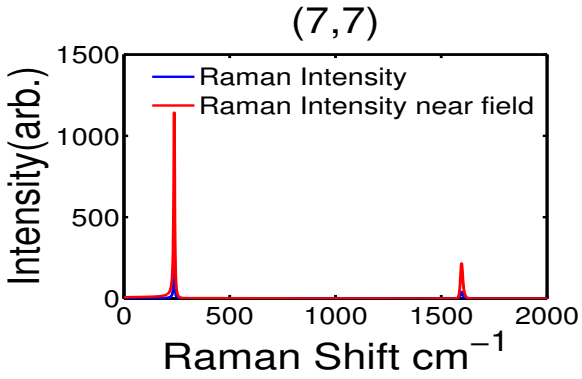

Figure 4-4: (7,7) Raman intensity with and without the near field matrix element, where for this case $|M_{\text{ex-nf}}| = 0.1347$eV, the incident laser energy $E_{\text{laser}} = 2.64eV$.

Mode, RBM, peak, which in this case is much smaller than that of the G mode, the second peak, corresponding to in plane longitudinal and transverse optical phonon modes.

In this case it is possible to see that the intensity of the second peak, G, is bigger than that of the first, RBM, that follows [41] which discuss the SWNT diameter dependence with the RBM intensity, which is lower for small diameter armchair.

Yet for a barely bigger diameter the case is different

Comparing the (5,5) and (7,7) SWNTs spectra it is clearly possible to distinguish the RBM intensity, which is bigger for the latter case, both SWNT are of the armchair family, however, the phonon dispersion relation for each of the chiralities differ, this is beyond the scope of this thesis and will not be discussed here.

The three spectra figures considered, show that the main result is an enhancement is of 10^4 times.

Fig. 4-4: fig:/0707ramanintensity.eps
Fig. 4-5: fig:/1010ramanintensity.eps

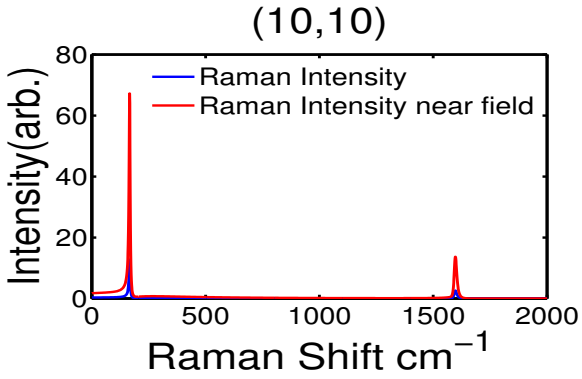

Figure 4-5: (10,10) Raman intensity with and without the near field matrix element, where for this case $|M_{\text{ex-nf}}| = 0.0978\text{eV}$, the incident laser energy $E_{\text{laser}} = 1.94eV$.

4.2 Chirality dependence of $Z_k D_k$ summation

Apparently there is a chirality dependence for the near field matrix element as well as for the far field one where

$$M_{\text{ex-ff}} = \sqrt{2}\sum_k Z_k D_k \tag{4.4}$$

the far field exciton matrix element has the usual dipole vector, $D_k = \mathbf{E}_{\text{ff}} \cdot \left\langle \Psi^f(\mathbf{r}, \mathbf{k}_f) \middle| \nabla \middle| \Psi^i(\mathbf{r}, \mathbf{k}_i) \right\rangle$ and

$$M_{\text{ex-nf}} = \sqrt{2}\frac{e\hbar}{m\omega}\left[\frac{ia_{22}}{2}\frac{1}{[q(a+d)]^3}\right]\sum_k Z_k^{\nu *} D_k \tag{4.5}$$

where Z_k is the exciton wavefunction from Fig. 4-1 and in this case the dipole vector has the near field factor direct influence $D_{\text{nf}k} = \langle \Psi_k^c | f_x^{\text{nf3}}(x) \frac{\partial}{\partial x} | \Psi_k^v \rangle$.

Fig. 4-6: fig:/dkzkchirality.eps

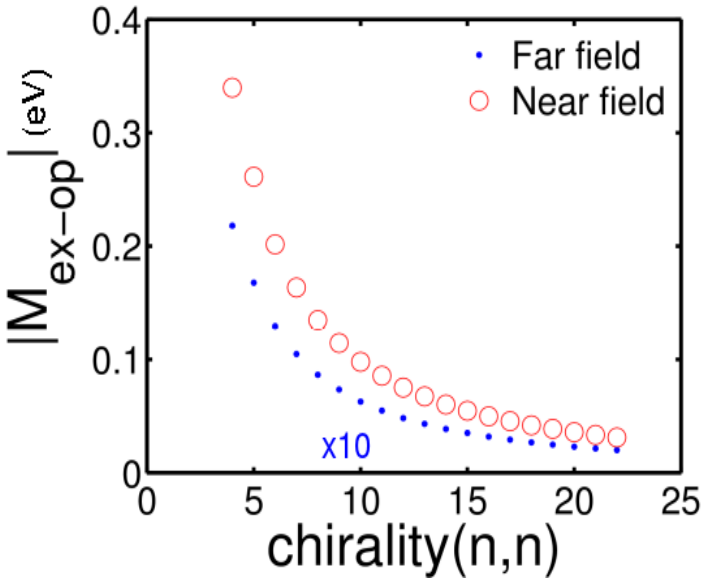

Figure 4-6: The red circle is the near field exciton photon matrix element absolute value, and the blue dot is the far field one. They have basically the same behavior.

Chapter 5

Conclusion

All this considered, the intensity found as main objective of this thesis, is usually 10^4 times bigger than the non enhanced one, this is surprising, since the experimental results do not show such an enhancement, however the basis from which it was possible to arrive is sound and justified,yet the program used in the calculations should be reconsidered. Apart from this the geometric dependence for the near field matrix element that was reached did not yet allow for a general chirality near field matrix element, yet it does not seen to be very far from employing the chiral angle dependence on the carbon atoms position vectors.

Apart from this immediate points, a third more troublesome arises, the dipole vector dependence with chirality was never discussed in detail before, and it wasn't the main objective of this thesis, but at least some speculation was tried. To improve the results here, a deeper analysis of the dependence between the metallic tip and the sample should be tried, as well as, the exciton transition energy, and the size of the spherical approximation to the tip.

Finally verification of the near field and far field influences over the exciton photon matrix element.

Appendix A

In chapter 3, the solutions from Maxwell's equations in spherical coordinates can be solved by the employment of the identities listed in appendix A-1. The differential equations for the electric and magnetic fields components E_θ, E_ϕ, B_θ and B_ϕ written in terms of the known E_r in TM mode are derived in appendix A-2. The associated associated Legendre polynomial and its properties that are used in the boundary conditions to obtain the coefficients of the scattering wave and the internal field in Mie's theory are given in the appendix A-3. The spherical Bessel and the spherical Hankel functions are given in the appendix A-4 to be used in the Mie's theory program.

A.1 Vector calculus in spherical coordinates

A.1.1 Differential identities in spherical coordinates

1. Gradient of any scalar ψ

$$\nabla\psi = \hat{e}_r\frac{\partial\psi}{\partial r} + \hat{e}_\theta\frac{1}{r}\frac{\partial\psi}{\partial\theta} + \hat{e}_\phi\frac{1}{r\sin\theta}\frac{\partial\psi}{\partial\phi}. \tag{A.1}$$

2. The Laplacian of ψ

$$\nabla^2\psi = \frac{1}{r^2}\frac{\partial}{\partial r}\left(r^2\frac{\partial\psi}{\partial r}\right) + \frac{1}{r^2\sin\theta}\frac{\partial}{\partial\theta}\left(\sin\theta\frac{\partial\psi}{\partial\theta}\right) + \frac{1}{r^2\sin^2\theta}\frac{\partial^2\psi}{\partial\phi^2} \tag{A.2}$$

3. The divergence of any vector $\mathbf{E} = E_r\hat{e}_r + E_\theta\hat{e}_\theta + E_\phi\hat{e}_\phi$

$$\nabla \cdot \mathbf{E} = \frac{1}{r^2}\frac{\partial}{\partial r}(r^2 E_r) + \frac{1}{r\sin\theta}\frac{\partial}{\partial\theta}(\sin\theta E_\theta) + \frac{1}{r\sin\theta}\frac{\partial E_\phi}{\partial\phi}. \tag{A.3}$$

4. The rotation of a vector $\mathbf{E} = E_r\hat{e}_r + E_\theta\hat{e}_\theta + E_\phi\hat{e}_\phi$

$$\nabla \times \mathbf{E} = \hat{e}_r(\nabla \times \mathbf{E})_r + \hat{e}_\theta(\nabla \times \mathbf{E})_\theta + \hat{e}_\phi(\nabla \times \mathbf{E})_\phi, \tag{A.4}$$

where

$$(\nabla \times \mathbf{E})_r = \frac{1}{r\sin\theta}\left[\frac{\partial}{\partial\theta}(\sin\theta E_\phi) - \frac{\partial E_\theta}{\partial\phi}\right], \tag{A.5}$$

$$(\nabla \times \mathbf{E})_\theta = \frac{1}{r\sin\theta}\left[\frac{\partial E_r}{\partial\phi} - \sin\theta\frac{\partial}{\partial r}(rE_\phi)\right], \tag{A.6}$$

$$(\nabla \times \mathbf{E})_\phi = \frac{1}{r}\left[\frac{\partial}{\partial r}(rE_\theta) - \frac{\partial E_r}{\partial\theta}\right]. \tag{A.7}$$

A.1.2 Vector Laplacian

The vector Laplacian $\nabla^2\mathbf{E}$ appearing in the vector Helmholtz equation is obtained from the following identities $\nabla \times (\nabla \times \mathbf{E}) = \nabla(\nabla \cdot \mathbf{E}) - \nabla^2\mathbf{E}$. If $\nabla \cdot \mathbf{E} = 0$, the vector Laplacian is then calculated from the double curl as $\nabla^2\mathbf{E} = -\nabla \times (\nabla \times \mathbf{E})$.

$$\nabla \times (\nabla \times \mathbf{E}) = \hat{e}_r(\nabla \times (\nabla \times \mathbf{E}))_r + \hat{e}_\theta(\nabla \times (\nabla \times \mathbf{E}))_\theta + \hat{e}_\phi(\nabla \times (\nabla \times \mathbf{E}))_\phi, \tag{A.8}$$

where

$$
\begin{aligned}
(\nabla\times(\nabla\times\mathbf{E}))_r &= -\frac{1}{r^2}\frac{\partial^2}{\partial r^2}(r^2E_r)-\frac{1}{r^2\sin\theta}\frac{\partial}{\partial\theta}\left(\sin\theta\frac{\partial E_r}{\partial\theta}\right)\\
&\quad -\frac{1}{r^2\sin^2\theta}\frac{\partial^2E_r}{\partial\phi^2}, \qquad (A.9)\\
(\nabla\times(\nabla\times\mathbf{E}))_\theta &= -\frac{1}{r}\frac{\partial^2}{\partial r^2}(rE_\theta)-\frac{1}{r^2\sin^2\theta}\frac{\partial}{\partial\theta}\left[\sin\theta\frac{\partial}{\partial\theta}(\sin\theta E_\theta)\right]\\
&\quad -\frac{1}{r^2\sin^2\theta}\frac{\partial^2E_\theta}{\partial\phi^2}-\frac{2}{r^2}\frac{\partial E_r}{\partial\theta}-\frac{2}{r^3}\frac{\cos\theta}{\sin\theta}\frac{\partial}{\partial r}(r^2E_r), \qquad (A.10)\\
(\nabla\times(\nabla\times\mathbf{E}))_\phi &= -\frac{1}{r}\frac{\partial^2}{\partial r^2}(rE_\phi)-\frac{1}{r^2}\frac{\partial}{\partial\theta}\left[\frac{1}{\sin\theta}\frac{\partial}{\partial\theta}(\sin\theta E_\phi)\right]\\
&\quad -\frac{1}{r^2\sin^2\theta}\frac{\partial^2E_\phi}{\partial\phi^2}-\frac{2\cos\theta}{r^2\sin^2\theta}\frac{\partial E_\theta}{\partial\phi}-\frac{2}{r^2\sin\theta}\frac{\partial E_r}{\partial\phi}. \qquad (A.11)
\end{aligned}
$$

It can be seen that only the radial component of $\nabla\times(\nabla\times\mathbf{E})$ is separable, the other two, are coupled

A.2 Differential equations for the Transverse Magnetic mode

In the TM mode, $E_r\neq 0, B_r=0$. Once E_r has been solved from the vector Helmholtz equation, the differential equations for E_θ, E_ϕ, B_θ and B_ϕ can be found from E_r based on Faraday and Maxwell and Ampere's laws

A.2.1 Faraday's law

Faraday's law describes the coupling of the electric and the magnetic field

$$
\begin{aligned}
\nabla\times\mathbf{E} &= i\omega\mathbf{B},\\
\hat{e}_r(\nabla\times\mathbf{E})_r+\hat{e}_\theta(\nabla\times\mathbf{E})_\theta+\hat{e}_\phi(\nabla\times\mathbf{E})_\phi &= i\omega(B_\theta\hat{e}_\theta+B_\phi\hat{e}_\phi). \qquad (A.12)
\end{aligned}
$$

Since the unit vectors are linearly independent, three differential equations come from equating the two sides from Eq. (A.12) :

$$\frac{\partial}{\partial\theta}(\sin\theta E_\phi) - \frac{\partial E_\theta}{\partial\phi} = 0, \tag{A.13}$$

$$\frac{1}{\sin\theta}\frac{\partial E_r}{\partial\phi} - \frac{\partial}{\partial r}(rE_\phi) = i\omega r B_\theta, \tag{A.14}$$

$$\frac{\partial}{\partial r}(rE_\theta) - \frac{\partial E_r}{\partial\theta} = i\omega r B_\phi. \tag{A.15}$$

A.2.2 Ampere and Maxwell law

The Ampere and Maxwell law is

$$\begin{aligned} \nabla\times\mathbf{B} &= -i\varepsilon\frac{k_0}{c}\mathbf{E}, \\ \hat{e}_r(\nabla\times\mathbf{B})_r + \hat{e}_\theta(\nabla\times\mathbf{B})_\theta + \hat{e}_\phi(\nabla\times\mathbf{B})_\phi &= -i\varepsilon\frac{k_0}{c}(B_r\hat{e}_r + B_\theta\hat{e}_\theta + B_\phi\hat{e}_\phi) \end{aligned} \tag{A.16}$$

Which can be separated into 3

$$\frac{1}{\sin\theta}\frac{\partial}{\partial\theta}(\sin\theta B_\phi) - \frac{1}{\sin\theta}\frac{\partial B_\theta}{\partial\phi} = -\frac{ik_0\varepsilon}{c}rE_r, \tag{A.17}$$

$$\frac{\partial}{\partial r}(rB_\phi) = \frac{ik_0\varepsilon}{c}rE_\theta, \tag{A.18}$$

$$\frac{\partial}{\partial r}(rB_\theta) = -\frac{ik_0\varepsilon}{c}rE_\phi. \tag{A.19}$$

A.2.3 Differential equation of E_θ in TM mode

Removing B_ϕ from Eq. (A.15) and Eq. (A.18), E_θ in TM mode is

$$\frac{\partial^2}{\partial r^2}(rE_\theta) + k^2(rE_\theta) = \frac{\partial^2 E_r}{\partial r\partial\theta}. \tag{A.20}$$

A.2.4 Differential equation of E_ϕ in TM mode

The same being done for B_θ from Eq. (A.14) and Eq. (A.19), E_ϕ is

$$\frac{\partial^2}{\partial r^2}(rE_\phi) + k^2(rE_\phi) = \frac{1}{\sin\theta}\frac{\partial^2 E_r}{\partial r \partial \phi}. \tag{A.21}$$

A.2.5 Differential equation of B_θ in TM mode

Repeating again for E_ϕ from Eq. (A.14) and Eq. (A.19), B_θ is:

$$\frac{\partial^2}{\partial r^2}(rB_\theta) + k^2(rB_\theta) = -\frac{i\varepsilon k_0}{c}\frac{1}{\sin\theta}\frac{\partial E_r}{\partial \phi}. \tag{A.22}$$

A.2.6 Differential equation of B_ϕ in TM mode

Finally for E_θ from Eq. (A.15) and Eq. (A.18), B_ϕ is

$$\frac{\partial^2}{\partial r^2}(rB_\phi) + k^2(rB_\phi) = \frac{i\varepsilon k_0}{c}\frac{\partial E_r}{\partial \theta} \tag{A.23}$$

A.3 The associated Legendre polynomials

Associated Legendre polynomials $P_l^m(x)$ have some indispensable properties used in Mie's theory. $P_l^m(x)$ which are solutions of the polar section from E_r in TM mode and B_r in TE mode in which m in Eq. (3.35) becomes zero. $P_l(x)$ of each order l can be taken from Rodrigues's formula written as

$$P_l(x) = \frac{1}{2^l 2!}\frac{\mathrm{d}^l}{\mathrm{d}x^l}(x^2-1)^l. \tag{A.24}$$

$P_l(x)$ of small order l obtained from Eq. (A.24) are listed below

$$P_0(x) = 1, \tag{A.25}$$

$$P_1(x) = x, \tag{A.26}$$

$$P_2(x) = \frac{1}{2}(3x^2 - 1), \tag{A.27}$$

$$P_3(x) = \frac{1}{2}(5x^3 - 3x), \tag{A.28}$$

$$P_4(x) = \frac{1}{8}(35x^4 - 30x^2 + 3), \tag{A.29}$$

$$P_5(x) = \frac{1}{8}(63x^5 - 70x^3 + 15x), \tag{A.30}$$

where $x = \cos\theta$. Higher order $P_l(x)$ may by obtained using the recursion relation

$$(l+1)P_{l+1}(x) = (2l+1)xP_l(x) - lP_{l-1}(x). \tag{A.31}$$

Then, $P_l^m(x)$ can be obtained from $P_l(x)$ using the following relation

$$P_l^m(x) = (-1)^m(1-x^2)^{m/2}\frac{\mathrm{d}^m}{\mathrm{d}x^m}P_l(x). \tag{A.32}$$

In Mie's theory, $m = 1$ would be a solution for the scattered wave and the internal filed because the incident light is a plane wave traveling in the $z-$direction, and the incident electric field is polarized along $x-$direction, however, this results in a null TM coefficient, therefore a second trial would be $m = 2$ and $l = 1$, yet this results in a null associated Legendre polynomial, the real solution to be used is then, $m = 2$ and $l = 2$. $P_2^2(\cos\theta)$ or higher $l = 1, 2, 3, 4, 5$ which comes from Eq. (A.26)-(A.30) into Eq. (A.32)

$$P_2^2(\cos\theta) = 3\sin^2\theta, \tag{A.33}$$

$$\tag{A.34}$$

The important properties of the associated Legendre polynomials are

1. The relation between the associated Legendre Polynomial and the Legendre Polynomial ($m = 0$) is

$$\frac{\mathrm{d}P_l(\cos\theta)}{\mathrm{d}\theta} = -P_l^1(\cos\theta). \tag{A.35}$$

2. The orthogonality of the associated Legendre polynomial

$$\int_{-1}^{1} P_l^m(x)P_k^m(x)\mathrm{d}x = \frac{2}{2l+1}\frac{(l+m)!}{(l-m)!}\delta_{kl}, \tag{A.36}$$

$$\int_{-1}^{1} \frac{P_l^m(x)P_l^n(x)}{1-x^2}\mathrm{d}x = \frac{(l+m)!}{m(l-m)!}\delta_{mn}. \tag{A.37}$$

3. The integral indentities of the associated Legendre polynomials used in Mie's theory :

$$\int_0^\pi \left(\frac{\mathrm{d}P_l^m}{\mathrm{d}\theta}\frac{\mathrm{d}P_k^m}{\mathrm{d}\theta} + m^2\frac{P_l^m}{\sin\theta}\frac{P_k^m}{\sin\theta}\right)\sin\theta\mathrm{d}\theta = \frac{2l(l+1)(l+m)!}{(2l+1)(l-m)!}\delta_{lk}, \tag{A.38}$$

$$\int_0^\pi \left(\frac{P_l^1}{\sin\theta}\frac{\mathrm{d}P_k^1}{\mathrm{d}\theta} + \frac{P_k^1}{\sin\theta}\frac{\mathrm{d}P_l^1}{\mathrm{d}\theta}\right)\sin\theta\mathrm{d}\theta = 0. \tag{A.39}$$

A.4 The spherical Bessel and the spherical Hankel functions

The spherical Bessel function $j_l(z)$ and the spherical Hankel function of the first kind $h_l^{(1)}(z)$

$$j_l(z) = (-1)^l z^l\left(\frac{1}{z}\frac{\mathrm{d}}{\mathrm{d}z}\right)^l\left(\frac{\sin z}{z}\right), \tag{A.40}$$

$$h_l^{(1)}(z) = -i(-1)^l z^l\left(\frac{1}{z}\frac{\mathrm{d}}{\mathrm{d}z}\right)^l\left(\frac{e^{iz}}{z}\right), \tag{A.41}$$

where $i = \sqrt{-1}$.

By using the Rayleigh formulas in Eq. (A.40), the spherical Bessel functions of

order $l = 0$ and $l = 1$

$$j_0(z) = \frac{\sin z}{z}, \tag{A.42}$$

$$j_1(z) = \frac{\sin z}{z^2} - \frac{\cos z}{z}. \tag{A.43}$$

Spherical Hankel functions of the first kind of order $l = 0$ and $l = 1$ by using the Rayleigh formulas in Eq. (A.41).

$$h_0^{(1)}(z) = -\frac{ie^{iz}}{z}, \tag{A.44}$$

$$h_1^{(1)}(z) = \left(-\frac{1}{z} - \frac{i}{z^2}\right)e^{iz}. \tag{A.45}$$

The higher order spherical Bessel/Hankel functions come from the recurrence relations

$$f_{l-1}(z) + f_{l+1}(z) = \frac{2l+1}{z} f_l(z), \tag{A.46}$$

$$l f_{l-1}(z) - (l+1) f_{l+1}(z) = (2l+1) f_l^{'}(z), \tag{A.47}$$

where f_l may represent j_l and $h_l^{(1)}$.

The Riccati Bessel functions $\psi_l(z)$ and $\zeta_l(z)$ defined as $\psi_l(z) = z j_l(z)$ and $\zeta_l(z) = z h_l^{(1)}(z)$, respectively, of the higher order ($l > 2$) come from those of the order $l = 0$ and $l = 1$ by using the recurrence relations, derived from Eq. (A.46)-(A.47), as follows

$$g_{l-1}(z) + g_{l+1}(z) = \frac{2l+1}{z} g_l(z), \tag{A.48}$$

$$(l+1) g_{l-1}(z) - l g_{l+1}(z) = (2l+1) g_l^{'}(z), \tag{A.49}$$

where g_l may represent ψ_l and ζ_l.

Appendix B

From chapter 4, a program was cited to calculate the near field exciton matrix element to be used into calculation for the tip enhanced Raman intensity calculation

B.1 Exciton near field matrix element calculation program

This program uses the exciton wavefunction from Nugraha *et al* [14] called zk-e22-0505-022.dat. Also the 3 nearest neighbors contributions for the near field exciton photon matrix element are nab1, nab2 and nab3.

After the end of the main code, the functions used to define the coefficient from the Helmholtz vector equation are defined, the Hankel and Bessel spherical functions.

The initial part mentioned, as well as the incident laser energy, was the input needed to obtain the exciton photon matrix element which is the output.

Apart from that the gaussian functions for the on site and off site matrix element contributions were read at the beginning of this program

/thesis/nfdipolevector.f90

The input data required is the chirality of the nanotube in question, the integers (n, m) value, the incident laser energy, E_{laser}, as well as the exciton wavefunction data with the near field dipole vector nearest neighbors components, this program only works for airmchair SWNTs.

References

[1] G.Mie, Ann. Phys. **25**, 377 (1908).

[2] J. Jiang et al., Phys. Rev. B **75**, 035407 (2007).

[3] L. G. Cançado et al., Phy. Rev. Lett. **103**, 186101 (2009).

[4] C. Chen, N. Hayazawa, and S. Kawata, Nature Communications **5**, 3312 (2014).

[5] A. Hartschuh, E. J. Sanchez, X. S. Xie, and L. Novotny, Phy. Rev. Lett. **90**, 095503 (2003).

[6] N. Peica, C. Thomsen, and J. Maultzsch, Nanoscale Research Letters **6** (2011).

[7] Z. Yang, J. Aizpurua, and H. Xu, Journal of Raman Spectroscopy **40**, 1343 (2009).

[8] M. B. Raschke and C. Lienau, Applied Physics Letters **83**, 5089 (2003).

[9] M. S. D. R. Saito, G. Dresselhaus, *Physical Properties of Carbon Nanotubes*, Imperial College Press, 1998.

[10] R. S. Ado Jorio, Mildred Dresselhaus and G. F. Dresselhaus, *Raman Spectroscopy in Graphene Related Systems*, WILEY-VCH, 2011.

[11] A. J. M. A. P. A. G. S. F. A. G. G. D. Ge. G. Samsonidze, R. Saito and M. S. Dresselhaus, Journal of Nanoscience and Nanotechnology (2003).

[12] R. R. M. Rasmita Sahoo, Graphene **3**, 6 (2014).

[13] A. Grüneis, *Resonance Raman spectroscopy of single wall carbon nanotubes*, PhD thesis, Tohoku University, 2004.

[14] A. R. T. Nugraha, Exciton environmental effect of single wall carbon nanotubes, Master's thesis, Tohoku University, 2010.

[15] F. Sangghaleh, B. Bruhn, T. Schmidt, and J. Linnros, Nanotechnology **24**, 225204 (2013).

[16] R. Saito, G. Dresselhaus, and M. S. Dresselhaus, Phys. Rev. B **61**, 2981 (2000).

[17] G. G. Samsonidze et al., Applied Physics Letters **85**, 5703 (2004).

[18] E. Artacho, T. L. Beck, and E. Hernández, physica status solidi (b) **243**, 971 (2006).

[19] A. Hartschuh, Angewandte Chemie International Edition **47**, 8178 (2008).

[20] L. G. Cançado, A. Hartschuh, and L. Novotny, Journal of Raman Spectroscopy **40**, 1420 (2009).

[21] L. G. Cançado et al., Phys. Rev. Lett. **103**, 186101 (2009).

[22] M. I. Mishchenko and L. D. Travis, Bull. Amer. Meteorol. Soc. **89**, 1853 (2008).

[23] N. W. Ashcroft and N. D. Mermin, *Solid States Physics*, Thomson Learning, 1976.

[24] P.Tapsanit, Near field enhancement of optical transition in carbon nanotubes, Master's thesis, Tohoku University, 2012.

[25] N. E. Christensen and B. O. Seraphin, Phys. Rev. B **4**, 3321 (1971).

[26] P. G. Etchegoin, E. C. Le Ru, and M. Meyer, The Journal of Chemical Physics **125**, (2006).

[27] P. B. Johnson and R. W. Christy, Phys. Rev. B **6**, 4370 (1972).

[28] S. Foteinopoulou, J. P. Vigneron, and C. Vandenbem, Opt. Express **15**, 4253 (2007).

[29] J. E. Nestell and R. W. Christy, Appl. Opt. **11**, 643 (1972).

[30] S. Kawata, *Near-Field Optics and Surface Plasmon Polaritons*, Springer Heidelberg, 2001.

[31] M. R. Spiegel, *Schaum's Outline of Theory and Problems of Fourier Analysis with Applications to Boundary Value Problems*, McgrawHill, 1974.

[32] T. Klar et al., Phys. Rev. Lett. **80**, 4249 (1998).

[33] J. D. Jackson, *Classical Electrodynamics*, John Wiley & Sons, Ltd., 1999.

[34] J. Vanderlinde, *Classical Electromagnetic Theory*, Kluwer Academic Publishers, 2005.

[35] E. B. Barros et al., Physics Reports **431**, 261 (2006).

[36] J. R. Walter Greiner, *Quantum Electrodynamics*, Springer, 2009.

[37] E. B. Barros et al., Phys. Rev. B **73**, 241406 (2006).

[38] J. Jiang et al., Phys. Rev. B **75**, 035405 (2007).

[39] Y. M. K. K. M. N. H. N. S. Y. H. I. Mai Takase, Hiroshi Ajiki and K. Murakoshi, Nature Photonics **7**, 550 (2013).

[40] E. H. Hasdeo, Electronic raman spectroscopy of metallic carbon nanotubes, Master's thesis, Tohoku University, 2013.

[41] K. Sato, R. Saito, A. R. Nugraha, and S. Maruyama, Chemical Physics Letters **497**, 94 (2010).